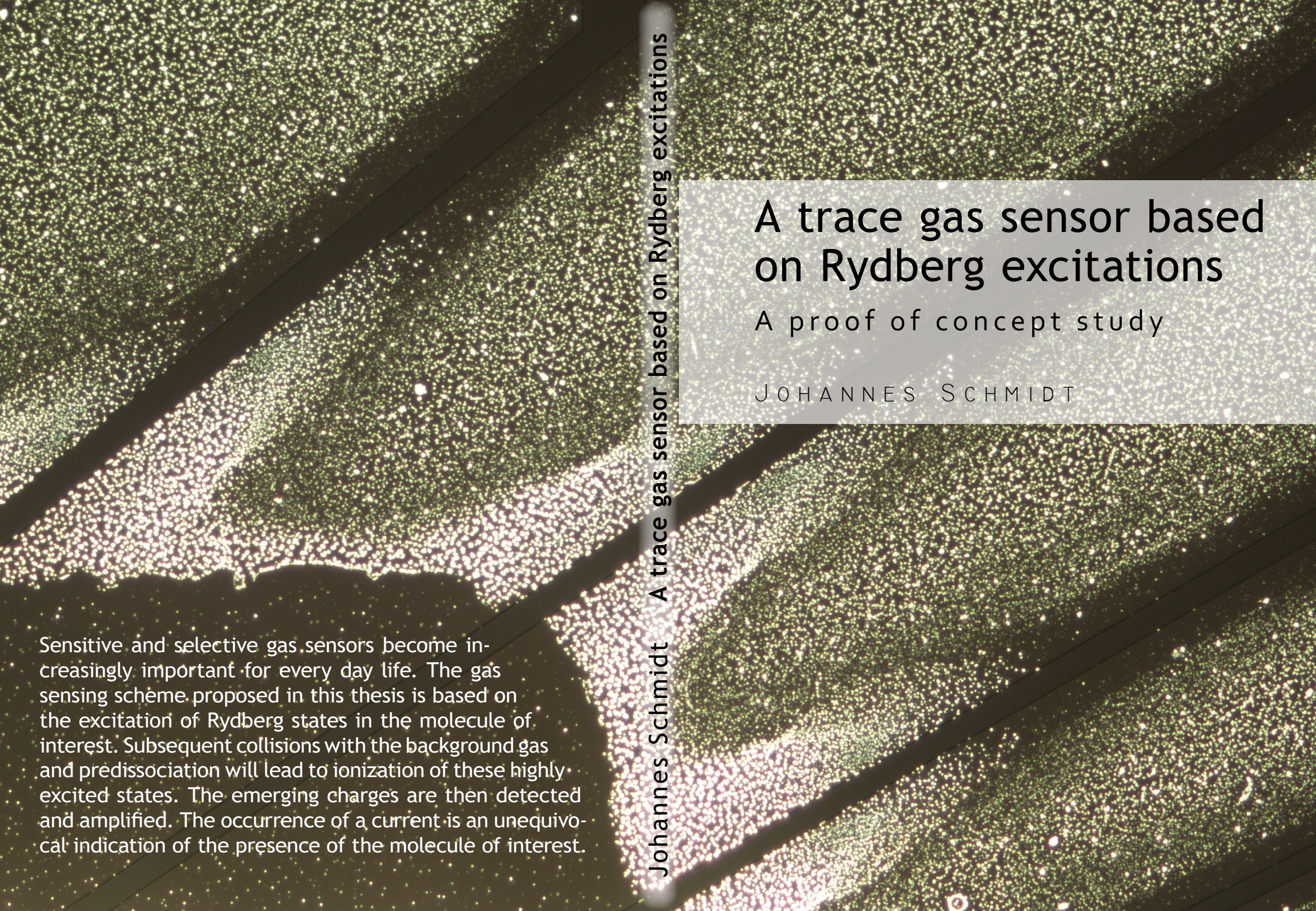

# A trace gas sensor based on Rydberg excitations

## A proof of concept study

Johannes Schmidt

Sensitive and selective gas sensors become increasingly important for every day life. The gas sensing scheme proposed in this thesis is based on the excitation of Rydberg states in the molecule of interest. Subsequent collisions with the background gas and predissociation will lead to ionization of these highly excited states. The emerging charges are then detected and amplified. The occurrence of a current is an unequivocal indication of the presence of the molecule of interest.

Johannes Schmidt A trace gas sensor based on Rydberg excitations

# A trace gas sensor based on Rydberg excitations

## A proof of concept study

Von der Fakultät Mathematik und Physik der Universität Stuttgart
zur Erlangung der Würde eines Doktors der Naturwissenschaften
(Dr. rer. nat.) genehmigte Abhandlung

vorgelegt von

**Johannes Schmidt**

aus Berlin

| | |
|---|---|
| Hauptberichter: | Prof. Dr. Tilman Pfau |
| Mitberichter: | Prof. Dr. Peter Michler |
| Prüfungsvorsitzender: | Prof. Dr. Hans Peter Büchler |
| Tag der mündlichen Prüfung: | 1. März 2019 |

5. Physikalisches Institut
Universität Stuttgart
2019

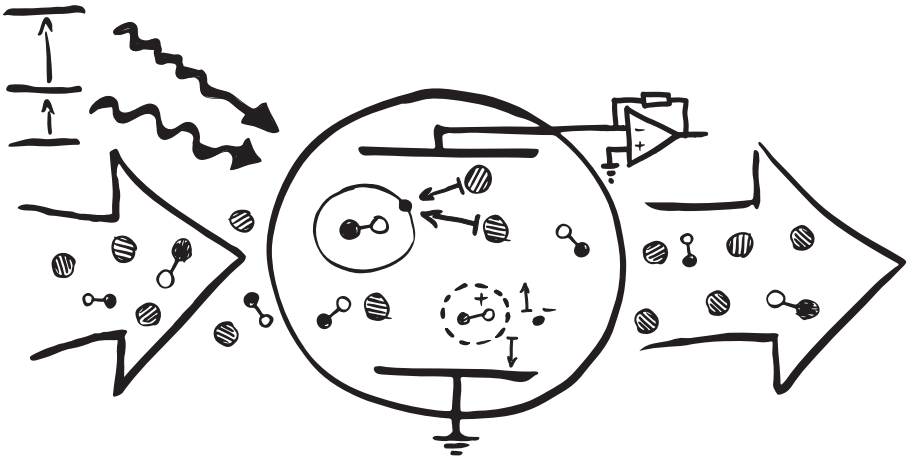

Artistic sketch of the Rydberg based gas sensor. A gas mixture is flowing into a glass cell. The atoms or molecules of interest are excited to a Rydberg state. These are then ionized via collisions with other particles in the gas mixture. The emerging charges are separated and measured using a transimpedance amplifier.

# Abstract

Sensitive and selective gas sensors become increasingly important for every day life. The gas sensing scheme proposed in this thesis is based on the excitation of Rydberg states in the molecule of interest. Subsequent collisions with the background gas and predissociation will lead to ionization of these highly excited states. The emerging charges are then detected and amplified. The occurrence of a current is an unequivocal indication of the presence of the molecule under consideration.
During the course of this thesis the applicability of the method was demonstrated by the example of nitric oxide in a gas mixture at ambient temperature and pressure. Further investigations were performed on a model system consisting of the analyte rubidium in a background gas of nitrogen. There, a sensitivity of 10 ppb in a gas with a concentration of 1 ppm was demonstrated. Special focus was put on the examination of the lineshape of the Rydberg signal depending on the background gas density. The last part of the thesis is dedicated to the fabrication methods used to realize the glass cells containing the gas. Several approaches to efficiently amplify the Rydberg created current signal are presented as well.

# Contents

# Zusammenfassung

**"Der richtige Riecher für exakte Diagnostik - Präzisionsspektroskopie misst winzige Stickoxid-Gasmengen dank Rydberg Anregung:** *Die Nase eines Hundes ist hunderttausendmal empfindlicher als die eines Menschen. Durch entsprechendes Training kann der "beste Freund des Menschen" sogar bestimmte Krankheiten beim Menschen riechen. Physiker der Universität Stuttgart treten nun in Konkurrenz zu den begabten Vierbeinern: sie bauen eine künstliche Nase, die noch deutlich sensibler ist als ihr natürliches Vorbild [1]."*

So wie es in dem obenstehenden Zitat schon angedeutet ist, handelt die vorliegende Arbeit von der Entwicklung eines neuartigen Gassensors basierend auf sogenannten Rydberg Atomen. Rydberg Atome nennt man Atome oder Moleküle, die in einen energetisch sehr hoch liegenden Zustand angeregt wurden. Solch eine Rydberg Anregung erreicht man heutzutage durch mehrere, das heißt zwei bis drei Laser Übergänge. Energetisch hoch liegend bedeutet hier, dass sich das äußerste Valenzelektron schon sehr nahe an der Ionisationsschwelle befindet, aber gerade noch so an den verbleibenden Atomrumpf gebunden ist. Dies erlaubt es, ein Atom, das sich in einem solchen Rydberg Zustand befindet, sehr leicht zu ionisieren. Das kann beispielsweise durch einen Stoß mit einem anderen Atom geschehen. Die aus diesem Prozess entstehenden Ladungen, das Elektron und der verbleibende ionische Atomrumpf können daraufhin als ein Strom über zwei Elektroden gemessen werden.
Im Vergleich zu einer optischen Detektion der Rydberg Anregung, ist die Messung dieses Ionisationsstroms mit wesentlich weniger Rauschen möglich. Eine solch hochauf-lösende Spektroskopie, die durch die verschiedenen Laser-Anregungen spektral sehr präzise ist und zusammen mit der Strommessung ein hohes Signal-zu-Rausch-Verhältnis aufweist, ermöglicht nun eine neue Art Gasdetektor zu realisieren.
Solch ein Gassensor könnte zum Beispiel für die Analyse eines Abgasstroms eines Autos verwendet werden oder auch für die Bestimmung bestimmter Krankheiten beim Menschen durch Untersuchung seines Atems. In einer innovativen

Vision könnte man sich vorstellen, dass ein Gasgemisch durch eine Glaszelle fließt. Dabei werden die zu detektierenden Atome und Moleküle, zum Beispiel Stickoxid, mit Lasern in den Rydberg Zustand angeregt. Durch Stöße beispielsweise ionisieren diese hoch angeregten Moleküle. Der kontinuierlich dabei entstehende Strom kann dann über eine Verstärkerschaltung gemessen werden. Aufgrund der verschiedenen Laser, die wie ein Fingerabdruck zu dem Molekül passen, ist das Erscheinen eines Stroms ein klares Anzeichen für das Vorhandensein ebendieses Moleküls in dem Gasgemisch.
Die Anwendbarkeit, die Untersuchung der Vorteile aber auch der Nachteile dieses Detektionsprinzips ist Thema dieser Arbeit. Zu diesem Zweck wurden zwei Experimente durchgeführt, die die prinzipielle Funktionsprüfung des Messprinzips zur Aufgabe hatten. Beide Experimente beschränken sich auf sehr unterschiedliche Parameterbereiche, tragen aber gerade dadurch zusammen zu einem umfassenden Bild der Anwendbarkeit des Sensorprinzips bei.
Das erste Kapitel dieser Arbeit beschäftigt sich mit der Frage nach der prinzipiellen Anwendbarkeit des Rydberg Gassensors. Als Leitfaden dienen dabei die "Technologie Reifegrade" [2] anhand derer zuerst die absolut grundlegenden Eigenschaften von Rydberg Zuständen eingeführt werden. Dies wird gefolgt von der Identifikation möglicher Nutzungsszenarien und wird abgeschlossen von ersten theoretischen Abschätzung der Sensitivität des Gassensors. Diese Abschätzungen werden hier schon im Vorgriff von den experimentellen Daten untermauert. Der restliche Teil dieses Manuskripts, die verbleibenden fünf Kapitel beinhalten die genauen Details, die zum Verständnis der Daten notwendig sind, die im ersten Kapitel schon verwendet wurden.
Die prinzipielle Anwendbarkeit des Sensorprinzips auf den identifizierten Fall, hier Stickoxid, wird in Kapitel 2 beleuchtet. Die notwendigen Experimente wurden während eines zweimonatigen Austauschs an das Institut von Prof. Dr. Ed Grant am Lehrstuhl für Chemie an der University of British Columbia in Vancouver durchgeführt. In einem zweiten Schritt wird die Messmethode in einem sehr klar definierten und charakterisierten Experiment am Beispiel des Alkalimetalls Rubidium getestet. Besonderes Augenmerk wird hier auf die Analyse des Rauschens gelegt.
Das Verhalten der Rydberg Zustände in Anwesenheit anderer Gasatome ist äußerst wichtig für den Gassensor. Die Wechselwirkung der Rydbergatome zusammen mit anderen Gasen wird schlussendlich die physikalische Grenze der Sensitivität des Sensors darstellen. Das nötige Hintergrundwissen und die zugehörigen Messungen werden in Kapitel 4 untersucht. Alle Experimente mit Rubidium wurden an der Unversität Stuttgart am 5. Physikalischen Institut

unter Leitung von Prof. Dr. Tilman Pfau durchgeführt. Die letzten zwei Kapitel, Kapitel 5 und 6 behandeln die technologischen Aspekte der Experimente. Es werden ein neuer Prozess zur Fertigung der verwendeten Glaszellen vorgestellt. Außerdem werden die verschiedenen getesteten Herangehensweise zur rauscharmen Verstärkung des Rydbergstroms untersucht. Diese technologischen Entwicklungen wurden am Institut für Großflächige Mikroelektronik unter Leitung von Prof. Dr. Norbert Frühauf an der Universität Stuttgart durchgeführt. Einen wesentlichen Beitrag hat dazu auch Prof. Dr. Jens Anders am Institut für Intelligente Sensorik und Theoretische Elektrotechnik geleistet, welches sich ebenfalls an der Universität Stuttgart befindet. Die Arbeit endet mit einem Wiederaufgreifen der Technologie Reifegrade des ersten Kapitels. Hier wird wird ein möglicher Pfad zur Weiterentwicklung des Sensorprinzips hin zu einem höheren Reifegrad aufgezeigt.

# Introduction

**"The right sense for precise diagnostics - Precision spectroscopy measures tiny nitric oxide concentrations thanks to Rydberg excitations:** *Compared to the humans' nose a dogs' nose is onehundredthousand times more sensitive. Through specific training "man's best friend" is even able to smell certain diseases. Physicists at the University of Stuttgart are now trying to compete with the talented tail-waggers: they are building an artificial nose, which is considerably more sensitive than its natural model."* (translated from [1])

Just as the quote suggests, this thesis deals with the development of a new gas sensing method based on Rydberg excitations. Rydberg atoms are atoms excited to high-lying states, where the valence electron is already far apart from the remaining ionic core. This excitation is achieved by using two or more laser transitions. Since the valence electron of such a Rydberg atom is only weakly bound it can be separated from the ionic core very easily, for example via collisions with the surrounding gas atoms. The emerging charges, the electron and the ion, can subsequently be measured as a current.
Thinking of the exhaust of a car engine or the exhaled breath of a human, one can come up with applications of this measurement method, like the detection of nitric oxide. In an innovative vision, the gas mixture under investigation would flow through a glass cell and the analyte of interest would then be laser-excited to a Rydberg state. This highly excited molecule would subsequently decay via collisions into charges. These charges are measured as a current. Due to the several required laser transitions, which fit to the analyte like a fingerprint, the occurrence of a current is an unequivocal signature of the presence of the molecule of interest.
The applicability of this gas sensing method is analyzed in this thesis. For this purpose, two proof of concept experiments were carried out, covering different parameter ranges. In this way, both experiments together provide an overview of the relevance of the newly invented method.

The present manuscript therefore starts of by providing the necessary knowledge to classify the Rydberg based gas sensor among other already existing gas sensing methods. The first chapter is structured according to the so called "technology readiness levels" [2]. By using the technical classifications of the maturity of a sensing method as orientation, the basics of Rydberg excited atoms are explained. This is followed by the identification of possible use-cases and concludes by summarizing the results of the complete thesis into preliminary estimations of the performance of a Rydberg based gas sensor.
The remaining five chapters of this thesis provide detailed understanding and illustrate the single results, which led to the estimations made in the first chapter.
The general applicability of the sensing method to the identified use-case, in this case nitric oxide, is investigated in chapter 2. The necessary experiments were performed during an exchange to the institute of Prof. Dr. Ed Grant in the chemistry department at the University of British Columbia in Vancouver in Canada.
In the next step, the method is analyzed at the example of rubidium in chapter 3 and special attention is put on the analysis of the noise properties of the sensor.
The behavior of the Rydberg states in contact with other surrounding gas atoms is of particular importance for the sensitivity of the proposed sensing method. The interaction between the groundstate atom or the Rydberg excited atom and other gas components imposes the methodical limit to the gas sensing scheme. The background knowledge including measurements are presented in chapter 4 under the alias "A gas sensor in through-flow". All experiments on rubidium were performed at the 5th institute of physics of Prof. Dr. Tilman Pfau at the University of Stuttgart in Germany.
The remaining chapters, chapter 5 and chapter 6, finally deal with the technological aspect of the presented work. There, newly developed techniques for the fabrication of the glass cells are presented. Also, the various attempts to realize low-noise current amplifiers for the measurement of the Rydberg current are introduced. These technological developments were carried out at the Institute for Large Area Microelectronics (IGM) of Prof. Dr. Norbert Frühauf at the University of Stuttgart. An essential part of the technological progress was also contributed by the Institute of Smart Sensors of Prof. Dr. Jens Anders at the University of Stuttgart.

The manuscript concludes by picking up the technical classification measure of technology readiness levels again, hence tying up the end to the beginning. There, a possible path towards the next level of technological maturity is pointed out.

# 1 Development of a new kind of gas sensor

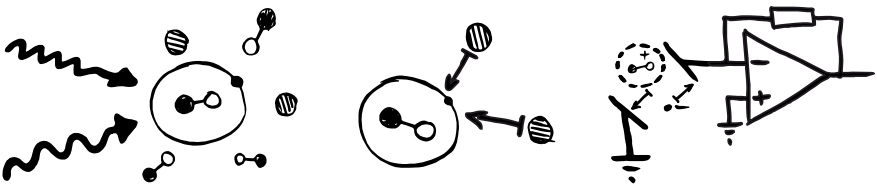

**Figure 1.1:** Schematic of the gas sensing idea. Rydberg states are excited via an optical n-photon excitation. The Rydberg excited molecules decay via collisions with the background gas into separated pairs of ions and electrons. Finally, the emerging charges are measured using a transimpedance amplifier (TIA) converting the incoming current into an output voltage.

When dealing with a new idea, it is often difficult to really grasp the actual applicability and relevance in the technological context. In order to quantify the maturity of a new technology, NASA was among the first to introduce a measure for the sophistication of a particular method or device: the technology readiness level (TRL). This scale has been adapted for the industry as well and is divided into nine stages of readiness [2]. This classification is intended for the use in space systems, but is also very applicable in the research and development sector:

- TRL 1: *"Basic principles observed and reported"*
- TRL 2: *"Technology concept and/or application formulated"*
- TRL 3: *"Analytical and experimental critical function and/or characteristic proof-of-concept"*
- TRL 4: *"Component and/or breadboard functional verification in laboratory environment"*
- TRL 5: *"Component and/or breadboard critical function verification in a relevant environment"*
- TRL 6: *"Model demonstrating the critical functions of the element in a relevant environment"*
- TRL 7: *"Model demonstrating the element performance for the operational environment"*
- TRL 8: *"Actual system completed and accepted for flight ("flight qualified")"*
- TRL 9: *"Actual system "flight proven" through successful mission operations"*

The explanation and classification of the Rydberg based gas sensor will be approached using this concept of assignment, starting from the basics of Rydberg physics and finalizing with the proof of concept realization.

# 1.1 Technology readiness level 1

**"Basic principles observed and reported:** *Scientific research exists related to the technology to be assessed and begins to be translated into applied research and development. Basic principles are observed and reported through academic-like research. Potential applications are identified but performance requirements are not yet specified [2]."*

The most important properties of Rydberg states are introduced first. More detailed concepts and theoretical foundations are discussed in chapter 2, chapter 3 and in chapter 4 as far as required for the understanding of the experiments.

## 1.1.1 Rydberg states

A Rydberg state with a principal quantum number $n$ is a quantum state of an atom, whose energy levels $E_n$ behave a lot like those of an hydrogen atom

$$E_n = -\frac{R_y}{(n-\delta_{nlj})^2}. \tag{1.1}$$

This means that the interaction of the valence electron with the ionic core can be described as the interaction with a point charge, which appears shielded by the inner shell electrons. In order to take this shielding into account, one introduces the effective principal quantum number $n^* = n - \delta_{nlj}$, which is reduced by the quantum defect[1]. The energy scale is given by the Rydberg energy

$$R_y = hc \cdot R_\infty \cdot \frac{1}{1+\frac{m_e}{m_{atom}}} = hc \cdot \frac{m_e \cdot e^4}{8c\epsilon_0^2 h^3} \cdot \frac{1}{1+\frac{m_e}{m_{atom}}} \overset{^{85}\mathrm{Rb}}{=} 13.606 \text{ eV}. \tag{1.2}$$

Since the electron is already far apart from the core, a lot of its properties are exaggerated compared to groundstate atoms. The scaling of some of the most important properties are given in table 1.1. The explicit formulas for calculating these quantities are given when needed.

[1] $\delta_{nlj} = \delta_{0lj} + \frac{\delta_{2lj}}{(n-\delta_{0lj})^2} + \frac{\delta_{4lj}}{(n-\delta_{0lj})^4} + \ldots$. Since the effective shielding by the remaining electrons depends on the penetration of the valence electron's orbit into the remaining shell, the quantum defect consequently depends on the total angular momentum and spin. For $^{85}$Rb and $nS_{1/2}$ states $\delta_0 = 3.1312$ and $\delta_2 = 0.1784$ are given [3].

**Table 1.1:** Scaling of important properties of Rydberg atoms with the principal quantum number.

| | | |
|---|---|---|
| Energy | $n^{-2}$ | [4] |
| Radius | $n^{2}$ | [4] |
| Geometric cross section | $n^{4}$ | [4] |
| Photoionization cross section | $n^{-5}$ | [5–7] |
| Polarizability | $n^{7}$ | [8] |

### 1.1.2 Rydberg excitation and detection

Rydberg atoms can be excited with various methods. An historical way relies on charge-exchange interaction and electron impact in gas discharge lamps. Of course, the excitation bandwidth is very broad in such cases. Later in history Rydberg atoms were excited in one step using x-ray radiation. With the invention of lasers the optical excitation became feasible. The use of several laser transitions allows to excite Rydberg states via an intermediate state without the use of deep UV light.

**Rydberg excited species** Using lasers, a lot of different atomic and molecular species were already demonstrated to be excitable to a Rydberg state. For a successful Rydberg excitation two things are necessary in most cases: First, a rather simple energy level scheme; Second, long-lived intermediate states, such that a significant portion of the groundstate population can be transferred to the excited states. Both requirements are based on the fact that the decaying intermediate states end up in the groundstate, where the atoms can again be excited and are not lost from the optical excitation cycle.
Apart from all alkali atoms, a lot of simple molecules have already been excited to Rydberg states. Examples among others are $CH_4$ [9], $CF_4$ [9], CO [10], $H_2S$ [11] or NO [12, 13]. Mostly insufficient laser power and also unknown transitions prohibit the investigation of Rydberg excitation in other more complex molecules.

**Measurement** The creation of Rydberg states can be measured with different methods. In cold atom experiments and also molecular beam experiments a state selective electric field pulse is often applied. The ionized atoms are then guided onto an avalanche detector, such as a channeltron or a microchannel plate [14, 15]. Also thermionic diodes were already used before [16, 17]. Another way is to collect the fluorescence of the decaying Rydberg states. One very common method when using coherent excitation light is the observation of electromagnetically induced transparency (EIT) [18]. For the principle demonstration of the proposed gas sensing method yet another method is used.
The equation (1.1) shows that an atom in a Rydberg state has already a very low binding energy. For a $^{85}$Rb atom in a $20S_{1/2}$ state, the needed velocity to ionize the atom via a collision with another Rb atom is only roughly 300 m/s. This corresponds to a temperature of 90°C. Consequently, a creation of charges is expected already at room temperature. The created charges can be measured as a current on a pair of electrodes. The exact behavior and dependencies of this current signal on the density of the analyte and the background gas density are examined in section 1.3.1 and in chapter 3.

The qualitative difference between the aforementioned optical detection of the Rydberg states via EIT and this current detection is the outstanding good signal to noise ratio. This has been investigated in the PhD thesis by Renate Daschner [20] and also in one of the first publications covering this topic [19]. An example of an optical EIT transmission signal and a current signal as function of the detuning $\Delta\omega_C$ of one of the two Rydberg excitation lasers on the example of $^{85}$Rb is plotted in figure 1.2. Both traces are taken from [19]. The EIT signal was obtained by employing an Lock-in amplifier and averaging for 15 minutes. The current signal was measured without further signal processing and over a time span of 0.1 s. The optical detection suffers from a huge background signal caused by a flux of photons, which did not interact with the atoms. This flux creates a lot of noise. Additionally, the EIT signal represents the coherence between the addressed levels. The current signal instead is directly proportional to the population in the Rydberg state and hence does not rely on a strictly coherent excitation. Although a coherent excitation can indeed increase the Rydberg population. This allows to detect the Rydberg creation even in the presence of a huge background gas density. In principle, the current signal does not contain a background signal, which decreases the inherent shot noise compared to the optical signal.

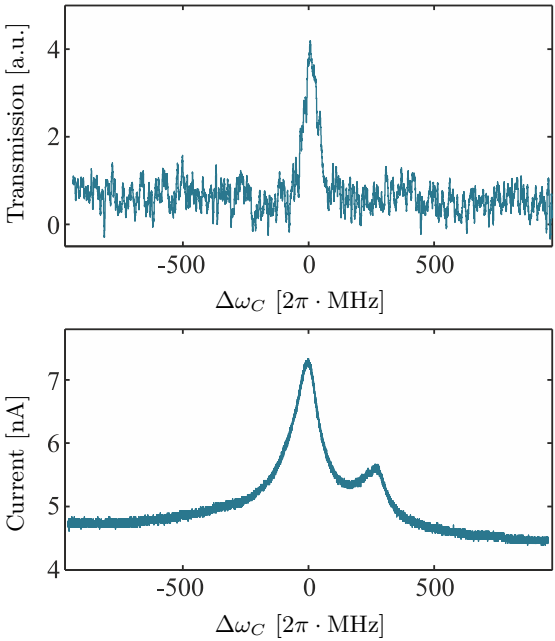


**Figure 1.2:** a) Optical EIT transmission signal of the Rydberg excitation. b) Current signal as function of the detuning $\Delta\omega_C$ of the Rydberg excitation laser. Both plots are taken from [19].

## 1.2 Technology readiness level 2

**"Technology concept and/or application formulated:** *Once basic principles are observed, practical applications can be invented. Applications are speculative and there may be no proof or detailed analysis to support the assumptions [2]."*

The concept of Rydberg atoms enabled a huge variety of discoveries and insights into physical phenomena. Also a broad range of applications were proposed or even demonstrated. Among those were single photon sources [21], single photon transistors [22], quantum gates [23] but also sensing devices, for example a sensor for microwave fields [24]. The excitation and measurement method

introduced in section 1.1 shows exceptionally good noise properties. One idea to make use of this property is to realize a sensor for trace gases.

**A trace gas sensor based on Rydberg excitations** The sensing method can be divided into three steps, which are illustrated in figure 1.1. First, the molecules or atoms of interest are excited to a Rydberg state using two or more laser transitions. Second, the Rydberg excited species decay into a pair of charges via collisions and predissociation. Finally, theses charges are measured as a current. The occurrence of a current is a clear indication of the presence of the analyte.

### 1.2.1 Use-case identification

One can easily imagine lots of applications for a gas sensor. For example the control of a combustion process inside a car engine, where the exact composition of the exhaust has to be monitored [25]; A plasma etching processing, where the gas composition has to be controlled very well [26]; Control and survey of crop growth [27, 28]; Or even the development of new medical drugs, as well as monitoring of diseases such as asthma or cancer in the exhaled human breath [29]. The challenge is to find an application, where already existing sensing methods are unsatisfactory and which is at the same time of technological relevance. One such application could be the detection of NO in exhaled breath. In order to understand the technological need for yet another gas sensing method it is necessary to understand the typical benchmarks of gas sensors, the possible application areas and most important how the proposed sensing method compares to other sensors in a specific field of use. Below, the most important benchmarks of a gas sensor are listed.

- Detection limit, Response, Sensitivity: The detection limit in parts per million, billion or even trillion is the smallest concentration the sensor can distinguish from zero signal. The response $(A - O)/O$ is the relative change of the sensors output value $A$ compared to its output value $O$ without the presence of the analyte. The sensitivity is the response of the sensor per change of the concentration. If the response to a small change of the concentration is large, the sensitivity is large as well.

- Selectivity: The sensor's ability to distinguish between the presence of one molecule and another is called selectivity. A sensor is extremely selective if it is sensitive to only one single type of molecule.

- Linearity: The monotonicity of the sensor's response and its theoretical calculability are very important for the interpretation of the output value of a sensor. Unknown effects and influences on the sensor will otherwise lead to a wrong diagnose.

- Methodology, Traceability: The way to theoretically calculate the output of the sensor, but also the way measurement errors are handled is part of the methodology. Additionally, if there is no need for calibration, then truly traceable, comparable and most important, absolute measurements become possible.

- Accuracy, Drift: The measurement error caused by unknown influences is called the accuracy. The drift is the decrease of accuracy over time.

- Lifetime, Chemical resistance: Gas sensors are often exposed to mixtures with unknown composition in chemically harsh environments. Under such circumstances the sensor might show increased parameter drift, which leads to a loss of accuracy and at some point the sensor might even degrade.

- Dynamic range: The range of concentrations starting from the detection limit up to the saturation of the sensor.

- Parameter range: The applicable parameter range is important not only in terms of concentration but also when it comes to different pressures, temperatures and required volume of the gas sample. The need for vacuum pressures better than $10^{-6}$ mbar for example will certainly prohibit the analysis of gases in a through-flow configuration. Also, the investigation of the breath of a mouse will not be possible with a sensor requiring 1 l of gas volume.

- Response time: A lot of processes are time-dependent. For example, it is interesting to know where exactly the source of a specific gas is situated inside a humans' lung. Observing the concentration of this gas depending on the stage of exhaling can give important insights on the course of a disease.

- Ease of administration, Portability: The best sensor cannot be employed if its technical overhead is so huge, that specially trained personnel is needed. Furthermore, some applications require small-sized sensors. This is important for example for analyzing the NO content in the exhaust of a driving car.

Obviously the choice of gas sensor does not only rely on its sensitivity and selectivity. A huge variety of other characteristic properties have to be weighed up in order to find the most convenient sensor for a specific task. In fact, there is no gas sensor, which is equally suitable for all possible situations.

### 1.2.2 Overview on gas sensors

**Table 1.2:** Advantages and disadvantages of different gas sensing methods

| | Pro | Contra |
|---|---|---|
| Capacitive, resistive, gravimetric, thermo-/biochemical | High $T$, $c$, $p$ | Low accuracy |
| Optical | Contactless | Light fluctuations |
| Photoionization | Contactless | Low selectivity |
| Electrochemical | Small | Drift |
| Chemiluminescence | Very sensitive | Large $V$ |
| Mass spectrometry | Very selective/sensitive | Low $p$ |

There exists a variety of different gas sensing methods, which all differ in terms of sensitivity and selectivity. Some of them are shortly explained now and special attention is put on the sensing methods, which are also employed for the detection of NO. The main advantages and also disadvantages are summarized in table 1.2.
A wide range of not very sensitive detectors are sensors, which are in contact with the investigated medium. These sensors are able to detect high concentrations of an analyte at sometimes extreme temperatures and pressures, but since they are in direct contact with the medium they all show a drift of their

characteristics and hence are not traceable. Those are, among others, capacitive and resistive sensors [30–32]. Also gravimetric sensors [33], which measure the oscillation frequency of a micromechanical cantilever, need to be calibrated regularly. The sensitivity and also selectivity of these sensors can be enhanced by utilizing tailored surface reactions. This is the case for some thermo- and biochemical sensors [34]. Still, none of these detectors reaches sensitivities, which are necessary for instance for a breath gas analysis of nitric oxide.
A gas sensing method, which circumvents the problem of surface deterioration is based on optical measurements. There, the absorption of laser light is observed, mostly by exciting vibrational transitions inside the molecule of interest [35–37]. Most optical sensors for NO use quantum-cascade lasers (QCL) with which the ground vibrational transitions of NO are probed at a wavelength of roughly 5.2 $\mu$m. It is also possible to excite electronic transitions such as the transition from the X $^2\Pi_{1/2}$ to the A $^2\Sigma$ state at roughly 225 nm. Since at this wavelength range, nitric dioxide and also sulfur dioxide have a broad absorption peak, their absorption has to be monitored at some other reference wavelength as well. Hence, the measurement of NO is only possible in a ratiometric way [38].
In order to reach very high sensitivities the signal has to be increased by interrogating a larger amount of gas molecules. This is accomplished by increasing the gas volume and also the effective beam path by employing high-finesse cavities around the probe volume. However, the adjustment of such optics is often only feasible by a specially trained person. Fluctuations of the light level are problematic for such sensors. Fluctuations by the light source itself and also dirt particles in the beam path eventually lead to false detection events. Additionally, the condensation of dirt and vapor onto the mirrors is a problem, which can only be circumvented by actively heating the cavity and using a cold trap before the sensor. This comes at the expense of an even larger gas volume. Additionally, the noise level is inherently increased, since always a small signal has to be measured on top of a huge photon background. Still, detection limits of lower than ppb can only be achieved for long interrogation times and at the expense of a higher maintenance. For example, the detection limit achieved by QCL based sensing methods is mostly above 1 ppb and the response time is also in the range of seconds.
One approach to enhance the selectivity is to photoionize NO in a 2-photon REMPI process (see chapter 2). The created ions are then separated from all other species by mass spectrometry [39]. This is very similar to another type of gas sensor, namely photoionization detectors [40]. Atoms of the mixture con-

stituent under consideration are optically ionized by exciting them directly into the continuum using two or three photon transitions. The overall sensitivity is low and the direct ionization diminishes the selectivity of the scheme.
Another class of sensors, which can be even more sensitive than optical sensors, are electrochemical sensors [41, 42]. A famous representative of this class of amperometric and potentiometric sensors [43] is the Lambda probe. The Lambda probe is maybe also the best example of a sensor, where a reference gas is mandatory and hence leads to the largest uncertainties. In general, any gas that can be electrochemically oxidized can be measured, for example by the following surface-mediated reaction [44]:

$$2\ \mathrm{NO} + 4\ e^- \rightarrow\ \mathrm{N_2} + 2\ \mathrm{O^{2-}}. \tag{1.3}$$

The sensor's selectivity, depends on the material of the electrode and the applied filters [45, 46], which inevitably comes at the cost of larger gas volumes, though. The detection limit is above 5 ppb and has an upper limit of around 500 ppb. The response time is longer than several seconds as well. The main problem arises from the aging of the electrode. For a medical usage, it is recommended to exchange the electrode after at most 300 measurements [47].
The current "gold standard" for sensing NO [47] is based on chemiluminescence. NO is mixed with ozone, where it chemically reacts to form nitrogen dioxide in an excited state. This decays spontaneously under emission of a photon, which is detected and amplified with a photomultiplier tube:

$$\mathrm{NO} + \mathrm{O_3} \rightarrow \mathrm{NO_2^*} + \mathrm{O_2} \tag{1.4}$$

$$\mathrm{NO_2^*} \rightarrow \mathrm{NO_2} + h\nu. \tag{1.5}$$

In principle, this method is limited by the collection and detection efficiency of the fluorescence. A concern are quenching processes, which lead to a collision induced radiation free de-excitation. These quenching processes depend highly on the background gas pressure. Therefore, a vacuum of around 10 mbar is mandatory [48]. The reaction above can also take place for other molecules, such as CO. There, special means to suppress the detection of the wavelength region of the fluorescence emerging from those molecules have to be taken. A source of systematic errors is the composition of the gas provided for the creation of the ozone. Special attention has to be put on selecting a carrier gas, which is free of NO. The required gas volume for the detection of ppb concentrations is about 1 l and the response time of a typical commercial system is about 1 s [49].

Mass spectrometry is traditionally the most sensitive investigation tool for gas compositions [50, 51]. Nevertheless, achieving selectivity for molecules with the same charge to mass ratio is complex and is getting more difficult for heavier particles. One famous example is $N_2$ and CO. Additionally the experimental overhead required for the high vacuum and the magnetic field make such a device bulky and its operation involved.
Obviously, there exist various ways to detect NO. Still, those measurement techniques are not flawless and among the sensing methods used for the detection of NO in medical environment none of these fulfills all requirements. This is discussed in the following.

### 1.2.3 Mammalian breath gas analysis

The big advantages of the Rydberg based gas sensing scheme are its sensitivity in the ppb regime and at the same time nearly perfect selectivity. Furthermore, it can be applied to very small gas volumes in chemically very demanding environments without showing signs of drift, at least from a methodical point of view. These advantages are explained in more detail in section 1.3. As already pointed out, among all the different gas sensing schemes and their applications, there is one use-case which fits the most to the proposed Rydberg gas sensing method: the examination of the nitric oxide content in the exhaled mammalian breath. There are two reasons. First, Rydberg excitation of NO has already been investigated and different excitation schemes are known. This is because NO is a small molecule with a rather simple level structure. Since it has only one single unpaired electron it is considered to be the "hydrogen atom" among the molecules. Second, the NO concentration in exhaled breath is only on the order of parts per billion instead of parts per thousand in the exhaust of a car engine. Additionally, its vital role for the immune system and as neurotransmitter has created more and more attention during the last years. Consequently, people came up with a list containing requirements for an NO gas sensor [52], which is summarized in table 1.3. A sensitivity in the ppb regime is required. In the best case this is possible in a through-flow configuration in real-time at ambient pressure without cross-sensitivities. Among the three most employed sensing methods there is none, which fulfills all requirements sufficiently. Hence, there is the possibility to fill a technological gap for a use-case with high relevance, where the benchmarks are already defined. Before the importance of NO is explained in more detail, it is insightful to learn about breath gas analysis.

This is one of the most enabling steps to classify the proposed Rydberg based detection scheme according to the technology readiness levels.
In fact, the importance of mammalian breath gas analysis has already been pointed out by Hippocrates centuries ago. Distinctive breath odors have been used as indicators of "evil humors", that are nowadays called diabetes, dental, lung, renal or liver disease [53, 54]. As a noninvasive examination method that additionally poses minimum risk to the person collecting the gas, breath gas analysis has enormous potential.
Human breath consists to the most part of nitrogen, oxygen, carbon dioxide, water and about 1% inert gases. Another 100 ppm consists of about 500 different compounds. Those can have exogenous and also endogenous origins. Interestingly, some of them are the same for all humans and a large concentration discrepancies of those particular compounds from one patient to the next can serve as an indicator for a pathological disease. For example a test for acetone is used to diagnose diabetes, increased amounts of ethane and ethylene can indicate oxidative stress, which leads to accelerated aging. Finally, nitric oxide is a clear indicator of an inflammatory disease, such as asthma, but also some sorts of cancer [53, 54].

**Nitric oxide in the human body** In 1998 the Nobel price in medicine was awarded for the discoveries concerning nitric oxide as a signaling molecule in the cardiovascular system [55–57]. It was found that the amino acid L-arginine produces NO, which acts as a neurotransmitter and causes the relaxation of smooth muscle tissue. This is called vasodilation. NO thereby regulates the blood pressure and protects the cardiovascular system from disease [55–57]. The onset of investigations of the role of NO in the human body led to the discovery that the vast variety of possible chemical reactions of this small molecule enables stimulation of RNA and protein synthesis, facilitates neurotransmission and controls gene expression [58]. Even more important is probably its function for the immune system. Because NO is a radical, it is supporting the immune system by destroying for example foreign bacteria. More recent work has shown that it regulates the immune function of macrophages [59]. Yet, in excessive amounts, NO is neurotoxic and can hasten apoptosis [58]. Consequently, increased NO concentrations can be observed where an inflammatory disease begins to spread. Diseases where an increased amount of NO can be found in the exhaled breath are asthma [60] and also certain types of cancer [61–64].

Whether the production of NO acts as an defense mechanism or is indeed harmful during an inflammatory disease is not yet fully understood. However, a healthy human exhales around 4-160 ppb of NO from the mouth and 200-2000 ppb from the nose. It was also found that NO concentrations are always higher in the upper respiratory tract than in the lower part. Again, the reasons still need to be investigated in more detail [65].

**Nitric oxide in the environment** Apart from the human body, other organisms were also found to use NO in a variety of ways. For example regarding plants [66], the correlation between illness and NO concentration is currently under investigation [67] and whether plants may potentially be able to store NO.
The present discussion on the impact of air pollution on our environment has spotlighted the small molecule NO. The main portion of air pollution in the atmosphere has anthropogenic sources, emerging mainly from the combustion of nitrogen-bearing fuels in motor vehicles. During the combustion, the bound nitrogen inside the fuel is released as free radical, which can also form NO. Since NO is very reactive, it reacts chemically to form other harmful substances, such as ground level ozone, nitrogen dioxide and volatile organic compounds. This noxious mixture is called photochemical smog [38]. This air pollution can even be monitored from satellites. From such data it was shown that there exists a robust relationship between an increased level of smog and infant mortality [68, 69]. Although correlation and causation should not be mixed up, such studies and the knowledge of the multiple functions of NO in the human body should raise awareness of a possible problem.
Although modern car engines emit less pollutants than some decades ago, the number of car engines keeps on rising, so that the overall amount of NO on ground level remained nearly unchanged since the upcoming of motorized vehicles [38]. The main emitter of NO are nowadays Diesel engines. This is due to the working principle of the catalytic converter. In a normal gasoline engine, which works with a mass of burned air to a mass of fuel ratio of $\lambda = m_{\mathrm{air}}/m_{\mathrm{fuel}} = 1$, the catalytic converter works in three ways. First, carbon monoxide is converted into carbon dioxide. Then, carbon hydrogen chains are converted into carbon dioxide and water. The remaining carbon monoxide from the first step interacts with the NO to form nitrogen and again carbon dioxide.

$$2\ CO + O_2 \rightarrow 2\ CO_2 \tag{1.6}$$

$$C_mH_n + (m + \frac{n}{4})\ O_2 \rightarrow m\ CO_2 + \frac{n}{2}\ H_2O \tag{1.7}$$

$$2\ NO + 2\ CO \rightarrow N_2 + 2\ CO_2. \tag{1.8}$$

In a Diesel engine, where an excessive amount of oxygen is needed $\lambda > 1$, the first process step works too well, such that no CO remains for the catalytic conversion of NO. Car manufacturers try to circumvent this by inventing new technologies such as the AdBlue technology [70] or even try to run the engine for some time in a less efficient way. Then, CO is available for the conversion of NO still sticking onto the surface of the catalytic converter. Of course, this can only happen on the expense of power.
Although a lot of effort is put into decreasing the amount of NO on the roads, it can still be demonstrated that the NO concentration inside a car even on a highway can easily exceed 2000 ppb [71], which is actually the maximum amount a healthy human should exhale.

**Table 1.3:** Required specifications for NO analyzers according to [52]. The names of some properties have been changed in order to be compliant with the technical terms introduced in this thesis.

| Parameter | Oral NO | Nasal NO |
|---|---|---|
| Pressure | 1 bar | $\sim$ |
| Temperature | 37°C | $\sim$ |
| Flow | 50 ml/s | $\sim$ |
| Detection limit | 1 ppb | 10 ppb |
| $SNR$ | $\geq 3:1$ | $\sim$ |
| Accuracy | $<$ 1 ppb | $<$ 10 ppb |
| Range | 1-500 ppb | 10 ppb - 50 ppm |
| Response time | $<$ 500 ms | $\sim$ |
| Drift | $<$ 1% of full scale/24 h | $\sim$ |

**Shortcomings of breath gas analysis** Breath gas analysis faces some challenges independent of the analyte. One of the major difficulties arises from complicated instrumentation. It is for example often reported that the outcome of a measurement is heavily depending on the way a person is breathing into the apparatus. Hence, it needs training for the operator and also for the examined patient [29, 54].
A lot of clinical studies are essentially not comparable with each other because no background measurements were done. As explained in the previous paragraph, the NO concentration near traffic roads can sometimes even exceed the maximum amount of NO a healthy person exhales. Additionally, other exogenous sources of increased NO concentration in the human breath have already been identified, such as smoking and certain types of food and also certain activities, such as excessive sport [52, 54].
A challenge in the measurement process is the chemical reaction of NO with any transition metal to a so called nitrosyl complex. Hence, special storing and transferring methods and materials need to be developed and standardized [52].
Most medical scientists nowadays agree that the measurement of the NO concentration can give insights on the course of a disease and the impact of medication, rather than being a fully compliant indicator of the presence of a disease [63].
In order to standardize the different sensing methods for NO, several attempts to introduce a joint language and measurement standard have been made by different organizations such as the American Thoracic Society and the European Respiratory Society [52]. They presented a list of requirements for the properties of a gas sensor for NO in the clinical field. The main benchmarks are summarized in table 1.3 and should be fulfilled at a flow of 50 ml/s, at a temperature of 37 °C and a pressure of 1 bar.

## 1.3 Technology readiness level 3

**"Analytical and experimental critical function and/or characteristic proof-of-concept:** *The proof of the element function or characteristic is done by analysis, including modeling and simulation, and by experimentation. The proof must include both analytical studies to set the technology into an appropriate context and laboratory-based experiments or measurements to physically support the analytical predictions and models [2]."*

Just as listed in the quote above, a top-down approach is taken to investigate the applicability of the proposed Rydberg based gas sensing method. A theoretical model is introduced, which, together with experimental results explained in the remainder of this thesis, allows to evaluate the applicability, impact of measurement errors and finally also possible roadblocks, which could prevent the realization of the sensor.
The results of two different experiments supporting the analytical model are summarized afterwards. The two experiments are in a sense very similar, but differ in the type of investigated species, the density range and the excitation method. Still, considering both as complementary fragments of a final prototype, the two experiments give valuable insights into the gas sensor's properties.
The first experiment is based on the Rydberg excitation of NO. It serves to demonstrate the applicability of the sensing method to a molecule of interest. Furthermore, it gives insight into the behavior of the sensor across a huge pressure range. The goal of the other experiment is the investigation of the Rydberg excitation of Rb in a background gas in a very controlled and predictable manner. This experiment serves to validate the theoretical model.

### 1.3.1 Modeling the behavior of the gas sensor

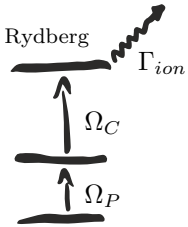


**Figure 1.3:** Level scheme.

One of the main advantages of the Rb experiment over the NO experiment is the possibility to theoretically estimate the amount of expected charges and the behavior of the Rydberg signal under the influence of the background gas. The Rydberg created current scales of course linearly with the density of analyte atoms $n$ inside the excitation volume $V$. Of those $n \cdot V$ atoms, only some are excited to a Rydberg state. The relative population of atoms in the excited state is denoted as $\varrho_{33}$. This population is a function of the Rabi frequencies $\Omega_P$ and $\Omega_C$ of the two excitation lasers. The Rabi frequency scales with the square root of the laser intensity and is a measure of the coupling strength between the light field and the atoms. Furthermore, the population $\varrho_{33}$ depends on the collisional processes, which lead to a depopulation and also an ionization of the Rydberg state. The rate $\Gamma_{ion}$ at which those collisions occur can be extracted from the width of the Rydberg signal. The quantity $\varrho_{33}$ can be calculated using the Liouville-von Neumann equation, as will be explained in chapter 3. A little level scheme with the involved variables is shown in figure 1.3. The overall amount of Rydberg atoms $n \cdot V \cdot \varrho_{33}$ is then ionized at a rate $\Gamma_{ion}$, which is assumed to be equal to the collisional rate being responsible for the broadening of the Rydberg line[2]. This rate is a function of the density and of the type of the background gas[3]. The overall measurable current is then given as

$$I_{Ryd} = e \cdot n \cdot V \cdot \varrho_{33} \cdot \Gamma_{ion}, \tag{1.9}$$

where $e$ is the elementary charge. This model has already been used extensively [19, 20, 72] and its validity is proven. This equation reflects the overall behavior of the Rydberg signal accurately. However, the absolute value often doesn't match the one obtained by the experiment. The reason is an insufficient knowledge of the experimental parameters. For example the laser power at the position of the atoms is not known exactly, due to absorption and scattering of the light at the cell walls. Furthermore, the exact overlap of the excitation

[2] In general, this is not true and will be explained in detail in chapter 3 and in chapter 4.
[3] Here again the validity is restricted. For example NO decays mainly through predissociation, which is not dependent on the background gas density

lasers is often not known well enough. Additionally, the collection efficiency of charges, meaning the efficiency by which already created charges are measured, and also the accuracy of the excitation volume lead to more discrepancies.
Consequently, this equation will be used to predict the properties of the gas sensor in terms of a rough scaling. The absolute estimated values for a given experimental situation will hence be calculated using the scaling obtained from equation (1.9) together with experimental measurements. This is exactly in the spirit of the definition of TRL 3.
The measurements of $\Gamma_{ion}$ as function of the background gas density are explained and presented in chapter 4. Two different background gases $N_2$ and Ar were investigated. From a linear fit to the width plotted in figure 4.4 and figure 4.5, the following behavior is determined[4]:

$$\Gamma_{ion}(n_{N_2}) = ((3.4 \pm 0.7) \cdot 10^{-15} \cdot n_{N_2} \cdot \mathrm{cm}^{-3} + (10.8 \pm 0.8)) \cdot 2\pi \cdot \mathrm{MHz} \quad (1.10)$$

$$\Gamma_{ion}(n_{Ar}) = ((5.3 \pm 0.9) \cdot 10^{-15} \cdot n_{Ar} \cdot \mathrm{cm}^{-3} + (11.6 \pm 1.1)) \cdot 2\pi \cdot \mathrm{MHz}. \quad (1.11)$$

The errors are deduced from the deviation of all fitted widths.
The Rabi frequencies $\Omega_P = (9.64 \pm 0.02) 2\pi \cdot \mathrm{MHz}$ and $\Omega_C = (4.75 \pm 0.01) 2\pi \cdot \mathrm{MHz}$ were inserted into the model, where the errors were measured by monitoring the fluctuations on the laser power over a certain time interval and reflect the fluctuations observable in a measurement time of 1 s.

### 1.3.2 Model calculation of the achievable detection limit

As a conservative back of the envelope estimation of the detection limit one can consider a minimum detectable current of 1 pA. This is well justified, since the current amplifiers employed for the proof of concept experiments have a noise level as low as $1\ \mathrm{pA}/\sqrt{\mathrm{Hz}}$. In order to create such a current around $6 \cdot 10^6$ ionized atoms/s are required, assuming that all atoms in a Rydberg state are ionized. This is in principle possible, for example by applying an electric field pulse. Since the atoms fly with a thermal velocity of at least 400 m/s across the excitation region, a volume of 8.8 $\mathrm{mm}^3$ can be exchanged at a rate

[4] The width of the Rydberg line is given in units of $2\pi \cdot$ Hz. Of course, the collisional rate $\Gamma_{ion}$ should be given in units of Hz, but will nevertheless be given in units of an angular frequency in order to simplify the comparison of collisional rates with the width shown in figure 4.4 for example.

of 400 kHz when the extension of the volume perpendicular to the laser beams is only 1 mm. Assuming an excitation efficiency of $\varrho_{33} = 10^{-5}$ based on the theoretical model, around 160,000 atoms have to be in a volume of 8.8 mm$^3$ in order to achieve a current of 1 pA. According to the ideal gas law, this corresponds to a partial gas pressure of $7 \cdot 10^{-10}$ mbar at room temperature. In a background gas pressure of 1 mbar this results in a detection limit of less than 10 ppb.
This estimation is based on the assumption that an atom can only be excited once into a Rydberg state while flying through the excitation region. It is in that sense a worst case estimation. Another way to approach the question of the detection limit is to evaluate $\varrho_{33} \cdot \Gamma_{ion}$ with the ionization rate given in equation (1.10). At 1 mbar background gas pressure, the expected amount of charges per Rb atom and second is $\varrho_{33} \cdot \Gamma_{ion} = 10^3$ Hz. For a current of 1 pA there are hence 6,200 atoms needed. In a volume of 8.8 mm$^3$ this corresponds to a partial gas pressure of $2.9 \cdot 10^{-11}$ mbar. Correspondingly, a concentration of 30 ppt can be detected with a current of 1 pA.
One result of the experiment in chapter 3 is that only around 1% of the collisions actually lead to an ionization. The actually achieved sensitivity is in the proof of concept experiment in chapter 3 accordingly 100 times less than predicted and is at approximately 5 ppb. This is in good agreement with the second estimation of 30 ppt, where this lower ionization efficiency was not yet taken into account. This estimate is valid for the employed laser powers and can be improved for higher laser powers.

### 1.3.3 External influences

The impact of external factors on the detection limit, such as pressure or fluctuating laser intensities imposed the performance limit also on other already presented gas sensors, for example purely optical gas sensors or detectors based on chemiluminescence.

**Density of the background gas** The behavior of the Rydberg population $\varrho_{33}$ and the expected amount of charges per Rb atom and per second $\varrho_{33} \cdot \Gamma_{ion} = \frac{I}{e \cdot n \cdot V}$ are plotted in figure 1.4 as function of the $N_2$ background gas density. The overall relative population $\varrho_{33}$ decreases from $10^{-4}$ by eight orders of magnitude for an absolute pressure of $10^3$ mbar. At the same time the

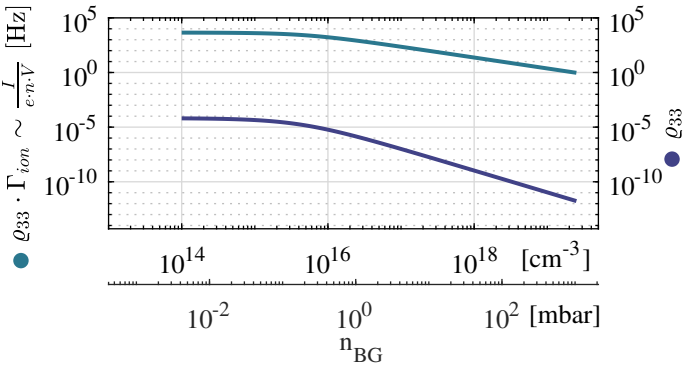


**Figure 1.4:** The number of charges per second and per Rb atom $\varrho_{33} \cdot \Gamma_{ion} \simeq \frac{I}{e \cdot n \cdot V}$ (upper curve) simulated for zero detuning as function of the background gas density $n_{BG}$ on the left axis and $\varrho_{33}$ (lower curve) on the right axis. $n_{BG}$ is once plotted as density in cm$^{-3}$ and correspondingly in mbar at a temperature of 300 K. Rabi frequencies of $\Omega_P = 9.6\ 2\pi \cdot$ MHz and $\Omega_C = 4.8\ 2\pi \cdot$ MHz were inserted. For $\Gamma_{ion}$ the relation $\Gamma_{ion}(n_{BG}) = ((3.4 \pm 0.7) \cdot 10^{-15} \cdot n_{BG} \cdot \text{cm}^{-3} + (10.8 \pm 0.8)) \cdot 2\pi \cdot$ MHz was used. This relation was determined from fitting the width of the current signal as function of the background gas density $n_{N_2}$ for the case of $N_2$. This will be discussed in detail in chapter 4.

amount of ionization events increases. Therefore, the amount of charges per Rb atom and second, which is proportional to the current $I$, decreases only by four orders of magnitude.

**Rabi frequency** The behavior of the amount of charges per Rb atom and second depending on the Rabi frequencies can also be estimated using the model in equation (1.9). The theoretical signal amplitude on resonance is shown in figure 1.5. For a low scattering rate $\Gamma_{ion}$, the expected current rises with $\Omega_P$ until it reaches a plateau. Beyond this maximum, power broadening and eventually Autler-Townes splitting start to decrease the signal amplitude on resonance. For an increase of the collisional rate, the maximum decreases and shifts to a different Rabi frequency. Examples of the signal shapes are shown in the insets of figure 1.5 for the indicated Rabi frequency $\Omega_P$. The same is true for the coupling Rabi frequency, shown in figure 1.5 b).

Obviously, the laser intensities need to be changed according to the collisional rate, if one wants to obtain the largest possible signal amplitude. Also, concerning the influence of fluctuating laser intensities, it is preferable to set the Rabi frequency to the maximum current. At this point, changes in intensity will lead the least to changes of the current signal.

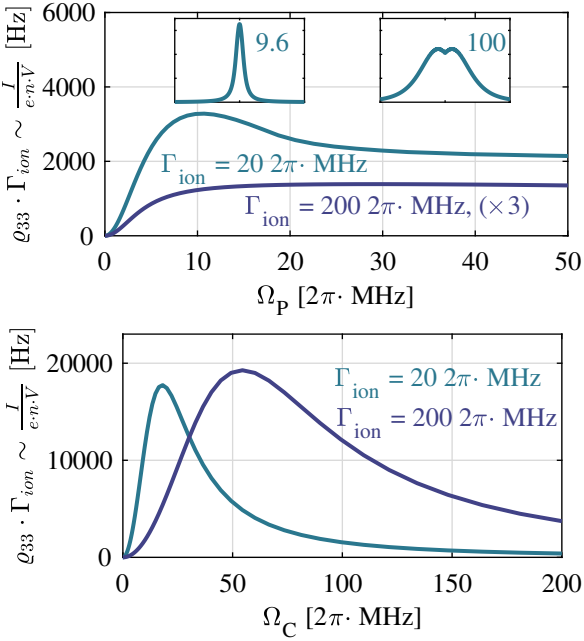


**Figure 1.5:** a) $\varrho_{33} \cdot \Gamma_{ion} \simeq \frac{I}{e \cdot n \cdot V}$ simulated for zero detuning as function of the $\omega_P$ Rabi frequency $\Omega_P$ for the two cases of $\Gamma_{ion} = 20\ 2\pi \cdot \text{MHz}$ and $\Gamma_{ion} = 200\ 2\pi \cdot \text{MHz}$ multiplied by 3 for visibility. For $\omega_C$ a Rabi frequency of $4.8\ 2\pi \cdot \text{MHz}$ was used and the temperature was set to 300 K. The insets show the theoretical spectra for $\Omega_P = 9.6\ 2\pi \cdot \text{MHz}$ and $\Omega_P = 100\ 2\pi \cdot \text{MHz}$ for the case of $\Gamma_{ion} = 20\ 2\pi \cdot \text{MHz}$ over a frequency range of $\pm 200\ 2\pi \cdot \text{MHz}$. b) $\varrho_{33} \cdot \Gamma_{ion} \simeq \frac{I}{e \cdot n \cdot V}$ for zero detuning as function of the $\omega_C$ Rabi frequency $\Omega_C$ simulated at the same conditions as in a) with a Rabi frequency of $\Omega_P = 9.6\ 2\pi \cdot \text{MHz}$.

### 1.3.4 Sources of measurement errors

The model in equation (1.9) can also be used to estimate the impact of systematic errors onto the gas sensor signal. There are three possible systematic error sources, which all occur for other gas sensors as well. One source of uncertainty are fluctuations of the Rabi frequencies $\delta\Omega$. The next source of error is insufficient knowledge of the background gas density or more precise the uncertainty of pressure $\delta p$ and temperature $\delta T$. Furthermore, considering a real-life application, the background gas composition $\delta c$ might change. As already indicated, measurements of NO depend also on the place where the measurement is performed. The analysis of all systematic errors was done by a linear propagation of uncertainty.

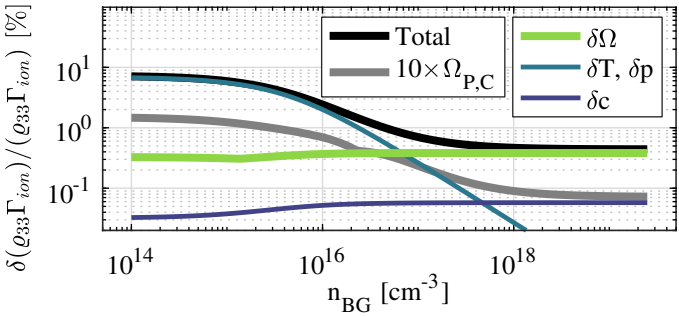


**Figure 1.6:** The relative error of the number of charges per second and Rb atom $\frac{\delta(\varrho_{33}\cdot\Gamma_{ion})}{\varrho_{33}\cdot\Gamma_{ion}}$ simulated for zero detuning as function of the background gas density $n_{BG}$. Rabi frequencies of $\Omega_P = 9.6\ 2\pi\cdot\text{MHz}$ and $\Omega_C = 4.8\ 2\pi\cdot\text{MHz}$ were inserted. For $\Gamma_{ion}$ the relation $\Gamma_{ion}(n_{BG}) = ((3.4\pm0.7)\cdot10^{-15}\cdot n_{BG}\cdot\text{cm}^{-3} + (10.8\pm0.8))\cdot2\pi\cdot\text{MHz}$ was used. This relation was determined from fitting the width of the current signal as function of the background gas density $n_{N_2}$ for the case of $N_2$. This will be discussed in detail in chapter 4.

**Rabi frequency** The impact of fluctuations of the Rabi frequencies $\delta\Omega$ on the current signal depends a lot on the absolute value of the Rabi frequency and the amount of collisional events. The relative error of the amount of charges created per Rb atom and second for the presented experiment is depicted in figure 1.6 as green line. With increasing $N_2$ background gas density the relative

error increases. This is again calculated for $\Omega_P = (9.64 \pm 0.02)\ 2\pi \cdot \text{MHz}$ and $\Omega_C = (4.75 \pm 0.01)\ 2\pi \cdot \text{MHz}$. It increases because the theoretically expected current as function of $\Omega_P$ shifts. This has the consequence that the fluctuations occur on a slope rather than on a flat top maximum, compare to figure 1.5.

**Temperature and pressure** Fluctuations of temperature $\delta T$ and pressure $\delta p$ lead to fluctuations of the background gas density, which in turn affects the trend of the Rydberg current with Rabi frequency. In order to model this type of error, the standard deviation of the offset of the linear polynomials is used, which origins from the fit of the Rydberg linewidth as function of the background gas density. The corresponding data is plotted in figure 4.4 and the resulting fit is written in equation (1.10). Since systematic inevitable errors are considered here, the slope is assumed to be known exactly, whereas the offset is caused by the unknown pressure and temperature. Obviously, the relative error decreases with increasing background gas density as it is depicted in figure 1.6 as a blue line.

**Other types of perturbers** In a real-life application, the gas composition might vary a little. Human breath consists of 78% $N_2$ and 1% rare gases. The discussion of the impact of other perturbing gases is omitted, since only collisions of $N_2$ and Ar with Rb were measured. The results are presented in chapter 4. One realistic scenario is to expect a concentration of the inert gas portion of 1% with a fluctuation of $\delta c = 0.01\%$. The resulting relative error is shown in figure 1.6 as purple line. Since it also effectively leads to a shift of the $\varrho_{33} \cdot \Gamma_{ion}(\Omega_P, \Omega_C)$ dependency, it rises with increasing background gas density.

The total relative error is depicted as black line in figure 1.6. Although around 10% relative error seems quite large for the present experiment performed at a $N_2$ density of around $10^{15}\ \text{cm}^{-3}$, it nevertheless fits to the experimental observations in chapter 3. For larger densities, the relative error decreases and is bound by the fluctuations of the laser intensities for the Rabi frequencies applied in the present experiment. By using ten times larger Rabi frequencies for $\Omega_P$ and $\Omega_C$, the total relative error can be decreased. This is due to the fact that the errors caused by the intensity fluctuation decrease and hence also the error caused by concentration fluctuations. This is depicted as gray line in figure 1.6.

**Statistical errors** The main contribution to statistical noise is caused by the current amplification. Depending on the gain, the thermal noise might dominate. For the experiments presented here, the main source of noise was emerging from insufficient electrical shielding. This is discussed in chapter 6. For the Rb experiment, this noise was increased by the current shot noise of the photocurrent. In both experiments, the technical noise limited the maximally achievable sensitivity of the proof of concept.

### 1.3.5 Summary of the two proof of principle experiments

After the theoretical consideration of the gas sensor, the experimental proof of concept is carried out. As already mentioned, two different experiments were performed, which support the theoretical model. Although both experiments are carried out on a very dissimilar parameter range, they can still give valuable insights into the performance of a gas sensor based on Rydberg excitations. The most basic properties, the parameter space in which the experiments were performed and the most relevant results are summarized in table 1.4.

**Investigations on nitric oxide** The primary aim of the first experiment is to demonstrate the applicability of the gas sensing scheme on a molecule of medical, biological and also industrial interest. The details of the methods and results can be found in chapter 2.
For this purpose, NO at room temperature is mixed with He and excited to a Rydberg state using two pulsed dye lasers. The gas composition is accomplished by mixing two different volumes containing the NO or He gas respectively at different pressures. A portion of the mixture is then transferred to the glass cell. The amount of NO in He is hence only estimated indirectly from the ratios of the volumes and pressures. Additionally, NO tends to form so called nitrosyl complexes with any transition metal and hence diffuses into the tubes connecting the glass cell. On the one hand there might consequently be less NO present than assumed, on the other hand the outgassing of NO from the metal surfaces prohibited the investigation of concentrations of less than 10 ppm.
The pulsed laser excitation has one advantage but also disadvantages. The advantage is the high laser power, which drives the transitions always in saturation. This makes this experiment superior to the Rb experiment, at least in this regard. Of course, the power was set in a way that no 2-photon ionization

**Table 1.4:** Summary of relevant properties of the two proof of concept experiments.

| | Nitric oxide | Rubidium |
|---|---|---|
| Species | Molecule | Atom |
| Excitation | Pulsed | cw |
| Time scale | $\approx 1$ ms | $\approx 1$ s |
| Model | / | 3-level |
| Gas mixing | Manual | Automatic |
| Background gas | He | $N_2$, Ar |
| Calibration | Volume + Pressure | Groundstate spectroscopy |
| Volume | 100 mm$^3$ | 8.8 mm$^3$ |
| Pressure range | $(10 - 10^3)$ mbar | $(10^{-2} - 10^{-1})$ mbar |
| Concentration | $(10 - 300)$ ppm | $(0.5 - 100)$ ppm |
| Efficiency | $(10^{-5} - 10^{-7})$ Ions/NO | $(6 - 5) \cdot 10^{-6}$ pA/Rb |
| Calibration limit | 10 ppm | 0.5 ppm |
| Accuracy | / | 5 ppb @ 0.5 ppm |

would occur. The disadvantage is that the excitation pulse is very broadband in linewidth and it is not stabilized onto a reference. Together with the pulse to pulse fluctuations of the laser power this leads to large fluctuations in the amplitude of the Rydberg created current. Another issue arising from the pulsed excitation is that, the true time at which the signal occurs, is much shorter than the whole cycle time of the experiment. In terms of signal acquisition and averaging this is surely unfavorable.
The two error sources, the gas mixing and the laser fluctuations, lead to large fluctuations of the data. Nevertheless, the experiment gives valuable input on the applicability of the sensing scheme.
First, it demonstrates that it is possible to excite NO in a gas mixture at room temperature. The results are very promising, considering that absolute concentrations as low as 10 ppm could be detected without further improvement

of the setup. Second, the excitation efficiency, meaning the amount of created charges per NO molecule decreases by only two orders of magnitude from a pressure starting at 4 mbar up to an ambient pressure of 1000 mbar. At ambient pressure a clear NO Rydberg spectrum is still visible.
The huge bandwidth of the pulsed NO Rydberg excitation prohibits most of the analysis on the lineshape of the Rydberg line. This is unfortunate, since the width of the line is directly related to the collisional processes occurring between NO and He. This would have given another possibility to estimate the actual population of Rydberg states. Additionally, the NO density was not measured with a complementary method, but instead estimated from the mixing ratios, which led to huge uncertainties in the experiment.

**Investigations on rubidium** Consequently, the gas sensing experiment was repeated in a more controlled manner, this time investigating the Rydberg excitation of the alkali atom rubidium.
Rb is constantly evaporated and diffuses through a background gas of $N_2$. The pressure and temperature is precisely known. Furthermore, the Rb density is now directly determined using groundstate spectroscopy. Yet, the disadvantage is that the amount of Rb is depending on the $N_2$ density, since the Rb needs to diffuse from the reservoir through the background gas to the excitation region. Additionally, the Rb tends to condense onto the walls of the glass cell. The upper Rydberg laser has sufficient energy to create photoelectrons emerging from bulk Rb sticking onto the glass walls. This photocurrent contributes to the Rydberg created current and increases the current noise due to the inherent shot noise.
Rb is being excited using two cw lasers with a very narrow linewidth and a well controlled and characterized laser power. The limitation is the power on the upper Rydberg transition, which is not sufficient to saturate the population. Together with the diffusion issue this limits the visitable pressure range to $(10^{-3} - 10^{-1})$ mbar.
Since the determination of the concentration of the gas mixture is done using groundstate spectroscopy, the characterization ends as soon as the optical thickness of the dilutions is too low for reliably determining the Rb density. Nevertheless, the Rydberg created current can be observed for even lower concentrations. This is proven by a signal to noise ratio of the Rydberg signal of 100 at an absolute concentration of 500 ppb and a pressure of $10^{-1}$ mbar.

**Comparison of the two experiments** Looking at the experiment with NO in chapter 2 and comparing the amount of charges per molecule with the measurements on Rb shown in figure 3.6 b) the low excitation efficiency becomes apparent: At a pressure of $p \approx 2{\cdot}10^{-2}$ mbar a current of $I_{Ryd}/N_{Rb} \approx 5{\cdot}10^{-6}$ pA per Rb atom is measured. Assuming an exchange rate of the whole excitation volume of 1.0 MHz estimated again from transit-time broadening (see chapter 4) one can estimate that one gets $Q_{ion}/N_{Rb} \approx 3 \cdot 10^{-5}$ charges per Rb atom. Here the Rb atom number is only the excitable amount of atoms in the $5S_{1/2}, F = 3$ groundstate at zero velocity, which is only 1.3% of all $^{85}$Rb atoms. Considering now the theoretical estimate of the scaling of the current, here $\varrho_{33} \cdot \Gamma_{ion}$, shown in figure 1.4, this means that one gets again four orders of magnitude less current at an absolute pressure of 1 bar. So in total around $Q_{ion}/N_{Rb} \approx 4 \cdot 10^{-11}$ charges per Rb atom are achievable. This is around three to four orders of magnitude worse than the amount of charges per NO molecule measured in the NO experiment shown in figure 2.9.
There are several reasons for the difference between the two experiments. First, the lasers for the NO measurement have a lot more power. That means the excitation efficiency is higher. Second, the ionization process in NO is a lot more efficient. NO can be ionized easier through collisions and additionally it predissociates on its own.

### 1.3.6 Advantages and possible roadblocks

Since both experiments are in some aspects very dissimilar, a clear statement is hardly possible. In the following, the advantages of a Rydberg based gas sensor are once again highlighted without concealing the problems that might arise.

**Detection limit and sensitivity:** For both experiments, the detection limit could not be identified. In both cases this is a consequence of the sample preparation. For NO, the outgassing from metal surfaces and for Rb the mixture preparation process were not controllable in a sufficient manner. In the case of NO there was no second characterization method employed and for the Rb the groundstate spectroscopy turned out to be not as sensitive as the proposed Rydberg gas sensing scheme. Nevertheless, in both cases a mixture of 10 ppm in the case of NO and a mixture with 1 ppm Rb was successfully

prepared. In the case of the Rb experiment the signal to noise ratio of the measured Rydberg signal was still 5 ppb at an absolute Rb concentration of 1 ppm. This is true as long as one assumes a linear dependency between the current signal and the concentration.
A result of the Rb experiment is the insight, that probably only 1% of the collisions lead to an ionization. This needs to be investigated more closely, which is not feasible with the current setup. Possible alternative setups and additional measurements are proposed at the end of chapter 3.

**Selectivity:** The selectivity has not been tested in any of the experiments. It is extremely unlikely that any other molecule will show similar energy levels as the molecule under investigation. Nevertheless, a current signal can be created by other processes. In the case of NO this can be a 2-photon ionization and in the case of Rb this is the photocurrent emerging from the photoeffect of the blue coupling light field on bulk Rb. Both current contributions could in principle be suppressed by Lock-in amplification. They nevertheless contribute to the noise floor of the measurement via their shot noise.
The pulsed dye lasers applied in the NO experiment additionally have a large bandwidth, so that the excitation of other species is indeed conceivable.

**Pressure range:** In the case of NO, the excitation efficiency drops by two orders of magnitude over a change of pressure from 5 mbar to $10^3$ mbar. This is depicted in figure 2.9. At $10^3$ mbar a clear Rydberg signal can still be observed. However, from the time traces of the arrival of the charges, shown in figure 2.10, one can conclude that although the excitation efficiency decreases as well, in this case charge recombination dominates the loss of efficiency. This is because the created charges need to diffuse through the background gas and there is hence more chance for recombination. This effect is not yet taken into account in the model calculation. The theoretical prediction for Rb is a drop of four orders of magnitude in the Rydberg population but also only a decrease of two orders of magnitude for the current signal on the same pressure increase as in the NO experiment. This scaling holds even if only 1% of the collisions actually lead to an ionization.

**Light fluctuations:** The discussion in section 1.3.4 showed that for each background pressure there is a certain Rabi frequency at which fluctuations lead to the least errors in the current signal. This has the consequence that for a gas sensor the laser intensities need to be monitored and if necessary readjusted to the optimal intensity. This is an optimization problem, since for the best Rabi frequency $\Omega_P$ the corresponding best Rabi frequency $\Omega_C$ needs to be determined for this certain background gas pressure. Of course, the induced error is only minor. Yet, having the maximum achievable current amplitude is in all cases favorable.

**Traceable measurement:** The analysis of possible errors, which affect the accuracy of the gas sensor, revealed that a change in the gas composition has an influence on the Rydberg signal. The discussion in section 1.3.4 was limited to a slight variation of the composition. For a completely unknown gas mixture, the exact determination of the amount of gas molecules of interest is consequently not possible since the collisional cross sections are not known. For such a task further investigations are required, for example testing the composition at a low pressure with a mass spectrometer. If one wants to apply the gas sensor for breath gas analysis a characterization needs to be done on a standardized model gas. The sensor is in that sense at most suited as a transfer standard.

**Chemical resistance:** The glass cells that are presented in chapter 5 withstand alkali vapor and can maintain an ultra-high vacuum. The encapsulation of sensitive electronics is possible as well. From this point of view the sensor will easily withstand also very harsh chemical environments. Nevertheless, the detection of small currents makes electrical shielding necessary. This might decrease the sensitivity in some application areas. Additionally, electrically conductive vapor such as water may lead to leakage currents, especially when a bias field is applied. Here, a smart cell design together with repellent surface properties can certainly lead to an improvement.

**Volume and Bandwidth:** A selling point of the proposed gas sensor is the small detection volume. This also permits a large bandwidth, since the gas volume can be exchanged very rapidly. This enables real-time monitoring in through-flow. Of course, the volume in the pipes connecting the cell are not

yet taken into account, but this fact is the same for other gas sensors as well. The need of a filter will depend on the final application.

**Applicability and ease of administration:** The operation of the glass cell including electronics could in principle be automatized and the cell can be shrank down to millimeter sized dimensions. The pumps for the vacuum have a high power consumption and are rather bulky. The same applies to the lasers. Fitting everything in a rack is certainly imaginable at the present state of the art. Nevertheless, this rack will certainly have a cubic meter sized volume. Additionally, there is a lot of maintenance necessary on the system itself. Also the interpretation of the acquired data is complicated as well. This is mainly due to the issue of the unknown total collisional cross section, which becomes important when investigating a gas mixture with an unknown composition.

The gas sensor based on Rydberg excitations so far shows some very interesting properties, which are promising for a real life application. Yet, there are some unresolved issues. These challenges apply also to other sensing methods and often lead to more unaccounted overhead. The issue of the unknown collisional processes and varying composition of the probe gas applies to the chemiluminescent sensor as well. But, compared to this sensor, the proposed scheme leaves still some room for improvement. For example an increase in laser power or a decrease of the current amplifier noise will immediately lead to an improved performance, whereas the chemiluminescent sensor is already at the physical limit in terms of best chosen pressure range, detection efficiency with single photon detectors and purity of the ozone gas. Compared to electrochemical sensors and optical sensors, the proposed sensor shows a much better selectivity and reproducibility already from a methodical point of view. It additionally has the potential to beat both sensors in terms of sensitivity and time response. The applicable pressure and concentration range exceeds the other two sensor methods already in the proof of concept experiments. Just as it is the case for all the other gas sensors, the sensing properties depend a lot on the final technical realization. Therefore it will be necessary to build a prototype where the characterization can be performed under well defined circumstances tailored to a real-life application. This stage of technological maturity is called TRL 4 and is the topic of the outlook in section 6.4.
But first the experiments by which the already presented results were obtained, are explained.

# 2 A gas sensor for nitric oxide

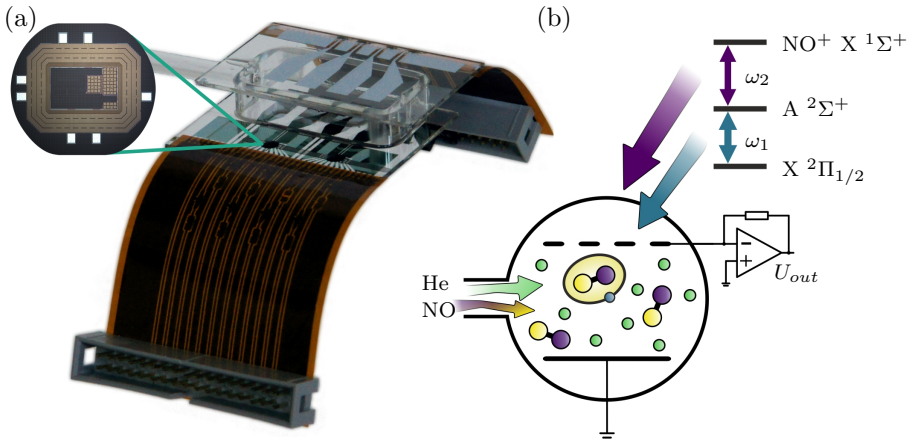


**Figure 2.1:** a) Picture of the glass cell with a microscope picture of the bottom of the TIA. b) Schematic of the experimental setup. Both pictures have been published in [73], all rights reserved. The glass cell is filled through an attached tubing with a mixture of NO and He, which was prepared and stored in a stainless steel vessel. NO is excited to a Rydberg state via the two laser pulses $\omega_1$ and $\omega_2$ shining through the frame of the glass cell. By subsequent predissociation and collisions with other particles the Rydberg excited NO molecules ionize. The charges emerging from the ionization of the excited molecules are detected and amplified with the transimpedance amplifier (TIA) shown in the zoom-in [74] as microscope picture imaged from the bottom.

## 2.1 Rydberg excitation of NO

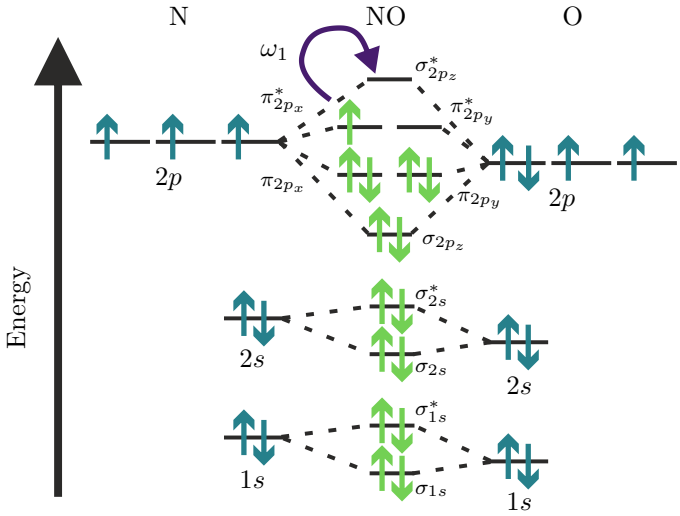


**Figure 2.2:** Molecular orbital diagram of NO.

### 2.1.1 The groundstate

Nitric oxide NO is a heteronuclear molecule and has in total 15 electrons. It is weakly polar and its molecular configuration is $1\sigma^2 2\sigma^2 2\sigma^2 4\sigma^2 5\sigma^2 1\pi^4 2\pi^1$. From the molecular orbital diagram shown in figure 2.2 one can see that it has an open shell, where only the $\pi^*_{2p_x}$ electron is unpaired. Consequently, the overall electronic spin is $\mathbf{S} = 1/2$. Since the symmetry of the field in which the electrons move is reduced compared to a single atom, the orbital angular momentum $\mathbf{L}$ is no longer a constant of motion. Nevertheless, its projection $\Lambda$ onto the internuclear axis is preserved. In case of the groundstate of NO, $\Lambda = 1$ and $\Lambda$ is designated as $\Pi$. Due to the orbital motion of the electrons, there is an magnetic field in the direction of the internuclear axis, which only vanishes for $\Lambda = 0$ (designated as $\Sigma$). This magnetic field lifts the degeneracy of the two possible electronic spin states $S$, because it causes a precession of the spin

around the molecule's axis, where again only the projection $\Sigma$ of the spin onto the internuclear axis stays conserved. The total electronic angular momentum is designated as $\Omega = |\Lambda + \Sigma|$ and has $2S+1$ different values for a given $\Lambda$. This multiplicity is designated in the superscript of ${}^{2S+1}\Lambda_\Omega$. These states are only degenerate in the case of $\Lambda = 0$ ($\Sigma$ state) and in the absence of rotation $\mathbf{N} = 0$ of the molecular core. The total angular momentum of the molecule $\mathbf{J}$ is the combination of $\Omega = |\Lambda + \Sigma|$ and the nuclear rotation $\mathbf{N}$.
Hence there exist two configurations for the groundstate of NO: ${}^2\Pi_{1/2}$ and ${}^2\Pi_{3/2}$, where each has their own rotational structure for the different $J$. Looking at the level scheme in figure 2.3, one can see that a difference in $\Omega$ (total electronic angular momentum) makes a much greater difference than a change in $N$ (nuclear rotation). This means the electron movement is mostly decoupled from the movement of the nucleus, since the $\mathbf{L}$ and $\mathbf{S}$ precess so fast around the internuclear axis. This is also called Hund's case a).
Still, the level scheme of the groundstate is somewhat complicated, since each rotational level splits up in two components. This phenomenon is called $\Lambda$-type doubling. Usually $\Lambda \neq 0$ states are doubly degenerate, since $\mathbf{L}$ could in principle show in either direction of the internuclear axis but its projection would still stay the same. Considering a rotating nucleus the situation changes, since the rotating charge distribution around the core atoms causes a magnetic field. Therefore, the rotation direction of $\mathbf{L}$ around the internuclear axis does indeed make a change, which becomes more pronounced for faster rotations $\mathbf{N}$ of the molecular core.
For historical reasons the groundstate of NO is called the X state. The absolute rotational and electronic ground state is hence X ${}^2\Pi_{1/2}$, $J'' = 0.5, N'' = 1$. Spectroscopically, one can observe a $\Lambda$-type doubling already in the lowest rotational groundstate, which is evidence for a rotation $N'' \neq 0$ of the molecular nucleus [75]. From $J'' = 0.5$ one can therefore calculate a hypothetical $N''$, if one treats this state mathematically already like a Hund's case b) as will be explained below.

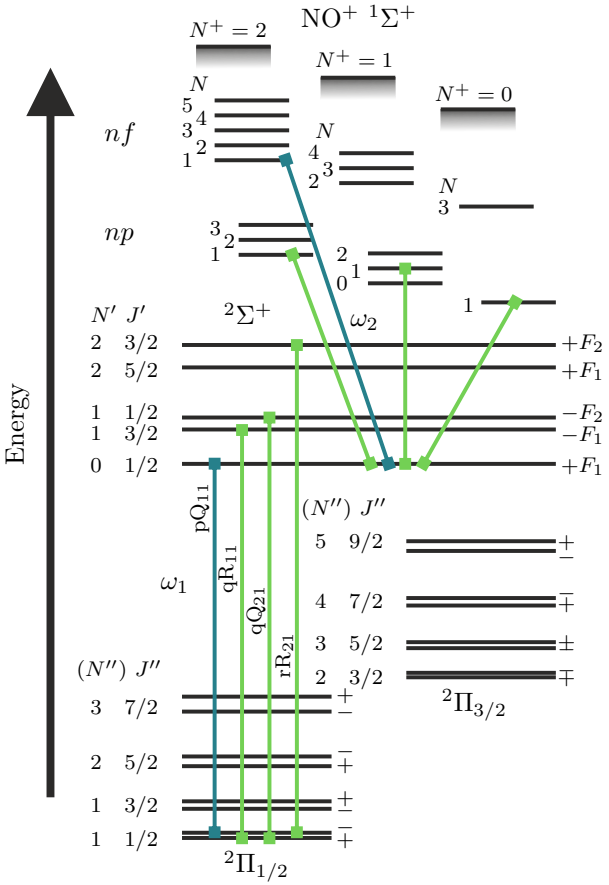


**Figure 2.3:** Levelscheme of NO.

### 2.1.2 The first excited state

The first excited state can be seen in the molecular orbital diagram of NO in figure 2.2. It is a $^2\Sigma$ state. That means the electronic angular momentum is $\Lambda = 0$ and hence there is no internal magnetic field. Consequently, the electronic spin **S** is no longer coupled strongly to the molecule's nuclear motion via its projection $\Sigma$ onto the internuclear axis. This uncoupling of **S** from the internuclear motion can also happen for very light molecules even for the case $\Lambda \neq 0$. This uncoupling is the signature of a Hund's case b). Nevertheless, just as in the case of the $\Lambda$-type doubling, the rotation of the nucleus induces a magnetic field, such that the position of the spin does make an energy difference. This difference is small though. The small dependence on the electronic spin, but comparatively large splitting due to the rotation of the nucleus is depicted in figure 2.3.
The rotation of the nucleus $N'$ together with $\Lambda$ form the new rotational state $\mathbf{K}'$. The total angular momentum is now given by $J' = |K' - S'|...(K' + S')$. Since $\Lambda = 0$ for the $^2\Sigma$ state, $N'$ will remain the denotation for the rotational state of the nucleus. The following selection rules apply: $\Delta J = 0, \pm 1$ and a change in the parity $(-1)^N$ has to take place. For a very cold ensemble of NO molecules the possible transitions are depicted in figure 2.3. By $p(P)$, $q(Q)$, $r(R)$ transitions where $N(J)$ change by $\Delta N(\Delta J) = -1, 0, +1$ are denoted. The spectroscopic labels $F_{1/2}(K)$ refer to rotational states $J = K \pm S$ and the subscripts in e.g $qR_{21}$ refer to a change from $F_1$ to $F_2$.
Again due to historical reasons the first excited state is called the A state. In general, addressing the transition from the X $^2\Pi_{1/2}$, $J'' = 0.5, N'' = 1$ state to the A $^2\Sigma$, $J' = 0.5, N' = 0$ state will be attempted.

### 2.1.3 The Rydberg state

The Rydberg state is once more a $^2\Sigma$ state, for which the electronic angular momentum is no longer quantized along the internuclear axis, but along the axis of rotation of the molecule. This scenario is often referred to as Hund's case d). The total angular momentum **K** is now given by a coupling of the rotation of the nucleus and the electronic angular momentum, $K = |N - L|...(N + L)$, where each level $K$ consists of $2S + 1$ components.
Since the movement of the electron is already independent of the nucleus one describes such a $^2\Sigma$ state with an $nl(N)$ state, just like in the case of a single

atom, where $n$ is the principal quantum number, $l$ is the angular momentum and $N$ remains the rotation of the nucleus. For increasing $n$, the $^2\Sigma$ state approaches the ionization continuum until it converges into the $^1\Sigma$ state of the $NO^+$ ion, where the electron is no longer bound. The rotation $N^+$ of the $NO^+$ ion is given by a coupling of the rotation $N$ of the nucleus of NO and its electronic angular momentum $l$: $N^+ = |N - l|...(N + l)$.
For the transition to a Rydberg state two things have to be taken into account. First, the intermediate state A $^2\Sigma$, $J' = 0.5, N' = 0$ can be described as a mixture of 94% $3s\sigma$ with a 5.5% contribution of a $3d\sigma$ state, the remainder is $p$ and $f$ like [76, 77]. It can therefore only be excited into another $np$ or $nf$ state [78]. Secondly for transitions from a $^2\Sigma$ state to another $^2\Sigma$ state the selection rule $\Delta N = \pm 1$ holds [79]. Consequently, from the $N' = 0$ rotational state of the A $^2\Sigma$ state only $N = 1$ states can be accessed. The possible transitions are shown in figure 2.3. Since the predissociation rate of the Rydberg states of NO drops for higher angular momenta of the electron [80, 81], $nf(N = 1)$ Rydberg states converging to the $^1\Sigma$, $N^+ = 2$ ionization continuum are excited [82–84]. All transitions used here are transitions in the lowest vibrational state $v = 0$ of the molecule and are hence not discussed.
The A $^2\Sigma$, $J' = 0.5, N' = 0 \longleftarrow$ X $^2\Pi_{1/2}$, $J'' = 0.5, N'' = 1$ groundstate transition has the disadvantage that it does not have the largest line strength of all transitions starting in the rotational groundstate $J'' = 1/2$ of the X $^2\Pi_{1/2}$ state at room temperature. The reason why this transition was still chosen as intermediate state is that one can only end up in a single rotational spin $N = 1$ state inside the Rydberg $nf$ series converging to the rotational state $N^+ = 2$ the $NO^+$ ion. The Rydberg states in a spectrum of such a transition appear in general a lot more pronounced [7].

### 2.1.4 Rydberg decay

Rydberg states in NO decay predominately via predissociation [80]. The Rydberg electron collides with the many-electron molecular nucleus and excites it to an unstable excited state. As a result the molecule breaks apart into neutral atoms. The rate at which this process takes places is getting slower for higher angular momenta $l$ of the Rydberg state [80, 81]. In a standard experiment lifetimes up to 100 ns [81] can be observed. This is much longer than would be expected for a Rydberg molecule excited to the $nf(N^+ = 2)$ manifold. This is due to angular momentum mixing caused by external electric and magnetic

fields, which overlap the eigenenergies of Rydberg states of the e.g. $ng(N^+)$ series with the addressed Rydberg state.
Charges can be created from a Rydberg excited NO molecule via collisions with other atoms and molecules, but mainly via collisions with charges, where the impinging electron transfers kinetic energy to the Rydberg electron [85–89]. There are also collisional processes which do not lead to the production of further charges, such as three body recombination, dissociative recombination and n-changing collisions [90].

## 2.2 Experimental setup

### 2.2.1 Laser system

The laser setup used to excite NO to the Rydberg states consists of two pumped dye lasers. For the $\omega_1$ transition, part of the 1064 nm pumping light is being frequency doubled first. It is subsequently mixed with the fundamental to generate a third harmonic. This emerging 355 nm light is used to excite transitions in a dye solution of coumarin 460 in methanol to result in emission of 452 nm light. The emerging 452 nm light is then frequency doubled using a doubling crystal to result in emission of 225 nm light. The emitted 225 nm light is filtered from undoubled portions using two prism pairs. The $\omega_2 = 328$ nm light[1] is produced by first frequency doubling the 1064 nm light. The emerging 532 nm light is used to pump transitions in a dye called DCM. The emitted 655 nm light is then yet again frequency doubled using a second harmonic generation crystal. The resulting 328 nm light is once more filtered through prism pairs and is sent through the glass cell via transmission through a dichroic mirror. The $\omega_1$ light is combined with the $\omega_2$ Rydberg excitation light via reflection at the dichroic mirror, such that both beams pass the cell in a co-propagating manner.
The $\omega_1$ beam has a diameter of $(3.4 \pm 0.6)$ mm and a pulse energy of $(4.5 \pm 0.3)$ $\mu$J radiated in a time less than 10 ns. The pulse energy was set as high as possible, such that yet no multi-photon ionization was measurable. The repetition rate of the both lasers is only 10 Hz. The $\omega_2$ has a diameter of

[1] Although it is a bit misleading, the notation $\omega$ was chosen for an wavelength designation. In this manner, the notation of the laser driving a particular transition remains in accordance with the other chapters of this thesis.

$(3.0 \pm 0.2)$ mm and a pulse energy of $(10.0 \pm 0.5)$ mJ. Both laser pulses are sufficiently energetic to saturate their respective transitions, which is clearly an advantage for the presented proof of principle experiment. A drawback of the employed lasers is the huge linewidth, since the lasers are not seeded by a narrow linewidth laser and not even an etalon is employed for spectral filtering. Therefore, the linewidth can easily exceed several gigahertz. The consequences for the presented experiment will be discussed in section 2.3.2.

### 2.2.2 Glass cell and current detection

The lasers shine through the frame of the cell shown in figure 2.1 a). Since standard borosilicate glass absorbs light of wavelengths less than 310 nm significantly [91], quartz glass was used for the frame, which has a thickness of 5 mm in the direction of the laser light and a height of 10 mm. The excitation volume inside the cell has a length of $(15.0 \pm 0.2)$ mm, which yields an excitation volume of only $(100.4 \pm 19.9)$ mm$^3$. Onto this frame a quartz tubing with a KF-16 flange is attached, through which the gas mixtures are filled into the cell. Above and below the frame are two glass substrates glued with Epotek-301 on which the footprint for the TIA and the electrodes for collecting the charges [6, 7, 19], consisting of 150 nm chromium, are sputtered. Since NO is not as reactive as alkali metals no special sealing method had to be applied here, as will be explained in chapter 5. The fast excitation pulses and therefore very rapid arrival of the Rydberg created charges made a fast TIA necessary. This allows to obtain a measurement of the arrival times of the ionic charges created by the pulsed laser excitation with as few harmonic distortion as possible. Details on the properties of the TIA and the manufacturing of the cell are presented in chapter 5 and chapter 6. For the present realization of the gas sensor, the transimpedance gain is set to 126 dBΩ, which permits a bandwidth of 2 MHz and an input referred current noise density of $7.4 \cdot 10^{-12}$ A$/\sqrt{\text{Hz}}$. The input of the amplifier is biased at a potential of 1.25V with respect to the counterelectrode, such that an $NO^+$ ion created in the middle of the cell in a distance of 2.5 mm from the electrodes would arrive after a flight time of roughly 900 ns in vacuum. This corresponds to an expected maximum frequency component in the current pulse of 1.1 MHz. This frequency will be somewhat lower because of the smaller mean free path length of the ions in the buffer gas. The arrival time of an electron will be 230 times faster than the ionic signal and can therefore not be observed.

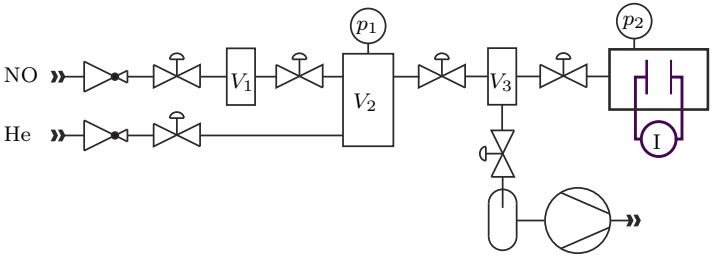


**Figure 2.4:** Schematic of the gas mixing apparatus.

For each laser shot a voltage trace is recorded and examples of which are shown in figure 2.10. With the known amplification factor the amount of ionic charges $Q_{\text{ion}}$ per shot is calculated by integrating over the whole voltage trace. By scanning the wavelength of the $\omega_2$ laser, spectra of the Rydberg series of thermal NO in a buffer gas of He are recorded, comparable to the ones shown in figure 2.8.

### 2.2.3 Gas mixing

In order to produce a mixture of NO with He a vacuum apparatus as depicted in figure 2.4 was set up. A small amount of gas mixed at a ratio of NO:He=1:9 is filled into a steel vessel $V_1$ at a certain pressure $p_1$. This small amount is then mixed with pure He inside a container $V_2$, which has a $(699.2 \pm 15.9)$ times larger volume than $V_1$. From this dilution only a small portion $(1 : (490.5 \pm 19.3))$ is transferred into $V_3$. This small amount is then expanded through a needle valve up to a certain pressure $p_2$ into the experiment chamber. The whole setup can be evacuated using a rotary vane pump.
A problem of this way of mixing gases is that a complete evacuation of the setup and therefore a precise concentration ratio can not be guaranteed. In the case of NO this can be especially dramatic, since NO forms so called nitrosyl complexes with any transition metal [92–94]. In those complexes NO is only weakly bound and therefore NO molecules diffuse into the metal [95]. The direction of this diffusion depends on the concentration of NO inside the metal and in the gas phase [96]. At low enough pressures a metal surface, which was once contaminated with NO, can outgas NO as well. As a consequence, this outgassing process deteriorates any dilution which is thinner than approx-

imately 10 ppm and sets a technical detection limit to this demonstration of our NO detection scheme. This will become apparent in section 2.3.4.
A better way to ensure at least well-defined concentration changes, is to build an experiment operated in through-flow [97] rather than in a static manner as done here. The overall concentration is then given by the conductivities of two massflow controllers and the whole setup can be flushed sufficiently long with a certain concentration. This ensures that a small outgassing rate will not be significant anymore.

## 2.3 Experiment and results

### 2.3.1 Groundstate spectrum - REMPI

Since there are no means of referencing or even stabilizing the $\omega_1$ laser in terms of an optical reference spectroscopy or a wavemeter, a groundstate spectrum has to be recorded. With this spectrum the exact wavelength position of the laser can be determined at which it will presumably stay for the time duration of the experiment. As will become apparent in section 2.3.2, this is not always the case. There are two ways to record a groundstate spectrum:

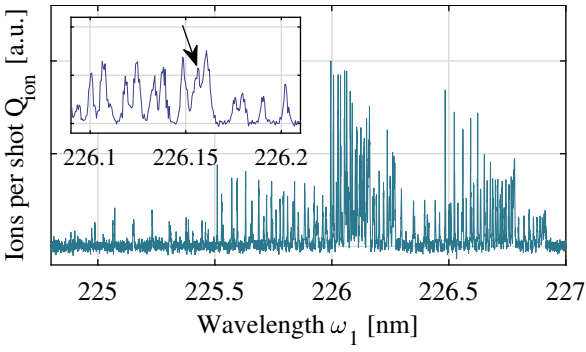


**Figure 2.5:** Groundstate spectrum of the A $^2\Sigma$ ($v = 0$) $\longleftarrow$ X $^2\Pi_{1/2}$ / X $^2\Pi_{3/2}$ transition in NO at room temperature obtained by REMPI. The $\omega_2$ laser was tuned to 327 nm. The arrow in the inset points at the addressed A $^2\Sigma$, $J' = 0.5, N' = 0$ $\longleftarrow$ X $^2\Pi_{1/2}$, $J'' = 0.5, N'' = 1$ transition.

- One can use sufficient pulse energy, such that multi-photon ionization of the $\omega_1$ laser excites molecules from the A $^2\Sigma$ state directly into the ionization continuum. This results for most lines in a broadening.
- One can also use only very small pulse energies of the $\omega_1$ laser and additionally shine in the $\omega_2$ laser with a wavelength set such that molecules from the A $^2\Sigma$ state are excited directly into the continuum. Compare here figure 2.6 a). For example setting $\omega_2 = 327$ nm will excite states inside the ionization continuum. This method is called **R**esonance-**E**nhanced **M**ulti-**P**hoton **I**onization (REMPI) [97].

To determine the correct line strengths using REMPI, the wavelength of $\omega_2$ should be adapted, such that for each $\omega_1$ wavelength the same position inside the continuum is addressed with $\omega_2$. This was not the case for the spectrum presented in figure 2.5. Therefore it does not reflect the theoretical spectrum in terms of signal amplitude. The spectrum was recorded at room temperature with a mixture of NO:He$= 2.6 \cdot 10^{-4}$ and a pressure of 40 mbar.
Another thing that becomes apparent from the inset of figure 2.5 is that already the $\omega_1$ laser has such a broad linewidth, that the single transitions can not be resolved. The arrow indicates the A $^2\Sigma$, $J' = 0.5, N' = 0 \longleftarrow$ X $^2\Pi_{1/2}$, $J'' = 0.5, N'' = 1$ transition, which is addressed for the Rydberg excitation.

### 2.3.2 Rydberg spectrum

In figure 2.6 a) an example of a Rydberg spectrum as function of the $\omega_2$ wavelength is plotted. Here an excessive amount of $\omega_1$ pulse energy has been used to further boost the single Rydberg lines via multi-photon ionization. For this spectrum also a different cell, electrode geometry, bias voltage and amplifier have been used. Therefore it can not be compared to any other Rydberg spectrum presented here. Still, from the distance of the Rydberg lines the $E = -R_y/n^2$ dependence can be seen very nicely. Another important aspect is that an excitation into the continuum is not as efficient as an excitation of a bound Rydberg state close to the ionization threshold. This holds true for other spectra recorded with less pulse energy of $\omega_1$ as well. Thinking in terms of an effective Rabi frequency for an off-resonant excitation of a state it is obvious, that the effective coupling efficiency has to decrease. Interestingly, the spectrum shown in figure 2.6 shows a major difference to other Rydberg spectra shown in e.g. 2.8 a). The numbers of charges decreases for higher Rydberg states. This is in fact not due to a decreasing excitation probability, since

the laser powers are by far sufficient to saturate their respective transitions. But from this one can see, that the major ionization process for this plot was indeed photoionization by the $\omega_1$ laser, since the photoionization cross section decreases with $n^{-5}$ [6, 7]. In comparison, in figure 2.6 b) the peak value of the

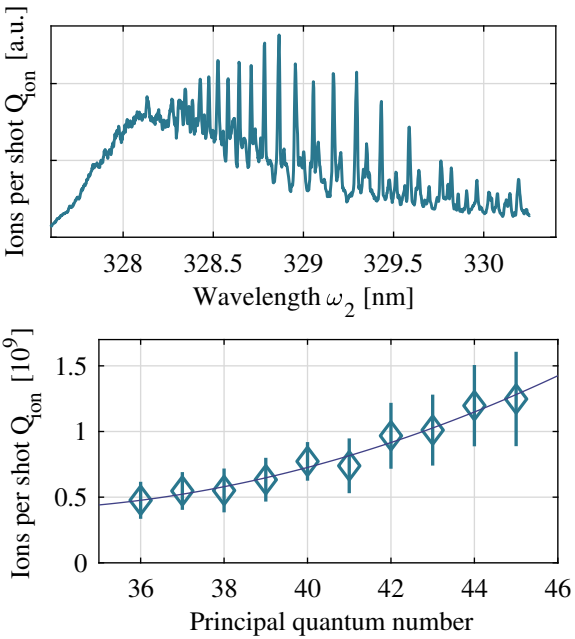


**Figure 2.6:** a) Rydberg spectrum of NO at room temperature with $\omega_1$ with an excessive pulse energy recorded in a different cell and with a different amplifier than all other spectra. The roll off at $\omega_2$ photon energies higher than 328 nm demonstrates the excitation of NO directly into the ionization continuum. b) Ions per shot obtained for each principal quantum number. The straight line is a quadratic polynomial fit showing the $n^{-2}$ dependency of the ionization probability.

Rydberg lines obtained from a spectrum shown in figure 2.8 a) is plotted. The straight line is a quadratic polynomial fit demonstrating the $n^{-2}$ dependence of the ionization probability. Clearly, higher states closer to the ionization continuum will be ionized more easily, since the valence electron is less strongly bound to the ionic core. This is indeed evidence, that the major ionization

process is due to collisions with other particles [6, 7].
The same is true for the experiment on Rb presented in chapter 3. Nevertheless, the insufficient laser power for higher Rydberg states would not allow to record a graph like in figure 2.8 a) without correcting for the changing Rabi frequency.
Consequently, the high pulse energy of a pulsed dye laser is an advantage for accessing high lying Rydberg states.

### 2.3.3 Lineshape

As already mentioned, the main disadvantage of the employed laser system is the huge linewidth. One consequence is that molecules not only from the A $^2\Sigma$, $J' = 0.5, N' = 0 \longleftarrow$ X $^2\Pi_{1/2}$, $J'' = 0.5, N'' = 1$ transition are excited to a Rydberg state but also from the nearby transitions $J' \longleftarrow J''$ (e.g. $4.5 \leftarrow 4.5$, $3.5 \leftarrow 3.5$, $1.5 \leftarrow 1.5$). This leads then to spectra as shown in figure 2.7 with one pronounced main peak and some other peaks at the side.

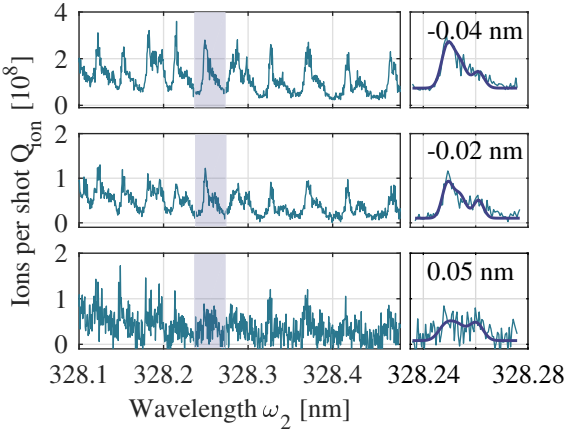


**Figure 2.7:** Rydberg spectra of NO as function of the $\omega_2$ wavelength. The data points marked with squares in figure 2.8 b) at a concentration of NO:He= $0.25 \cdot 10^{-4}$ were extracted from those spectra. The plots to the side are a zoom-in on the shaded regions at $n = 40$ plotted together with the fitted equation 2.1 and the relative position of the $\omega_1$ laser.

**Table 2.1:** Table holding the properties of the relevant transitions in the vicinity of the main A $^2\Sigma$, $J' = 0.5, N' = 0 \longleftarrow$ X $^2\Pi_{1/2}$, $J'' = 0.5, N'' = 1$ transition.

| $J'' \rightarrow J'$ | $\omega_{J''\rightarrow J'}$ [nm] | $A_{J''\rightarrow J'}$ |
|---|---|---|
| $5/2 \rightarrow 5/2$ | -0.0076 | 0.0027 |
| $7/2 \rightarrow 7/2$ | -0.0066 | 0.0034 |
| $3/2 \rightarrow 3/2$ | -0.0054 | 0.0019 |
| $9/2 \rightarrow 9/2$ | -0.0024 | 0.0041 |
| $1/2 \rightarrow 1/2$ | 0 | 0.0015 |
| $11/2 \rightarrow 11/2$ | 0.0051 | 0.0046 |

One question that arises is, what impact a slightly off-resonant positioning of the $\omega_1$ laser has on the Rydberg lineshape. As a very crude modeling of the Rydberg lineshapes, the theoretical lineshapes of the groundstate transitions are assumed to translate similarly into the Rydberg state. Accordingly, the theoretical groundstate spectrum is weighted with the envelope of the $\omega_1$ laser, modeled as a Gaussian function with a relative position $\omega_{shift}$ to the center wavelength $\omega_{n=40}$ of the $n = 40$ Rydberg state and a width $\Gamma_{\omega_1}$. The groundstate transitions are also modeled as Gaussian functions with a relative position $\omega_{J''\rightarrow J'}$ to the main $\omega_{1/2\rightarrow 1/2}$ transition, a line strength $A_{J''\rightarrow J'}$ and a width $\Gamma_{J''\rightarrow J'}$. This width was kept the same for all transitions.
The positions $\omega_{J''\rightarrow J'}$ and line strengths $A_{J''\rightarrow J'}$ were calculated with help of the program PGOPHER, which uses semi-empirical equations for simulating a spectrum at a certain temperature. The six strongest transitions $J'' \rightarrow J'$, their relative positions $\omega_{J''\rightarrow J'}$ and their line strengths $A_{J''\rightarrow J'}$ are shown in table 2.1. The complete fit function looks then like this

$$Q_{ion}(\omega_2) = \underbrace{A \cdot \frac{1}{\Gamma_{\omega_1}} e^{\frac{(\omega_2-\omega_{n=40}-\omega_{shift})^2}{2\Gamma^2_{\omega_1}}}}_{\text{Envelope of } \omega_1} \cdot \underbrace{\sum_{J''\rightarrow J'} A_{J''\rightarrow J'} \cdot \frac{1}{\Gamma_{J''\rightarrow J'}} e^{\frac{(\omega_2-\omega_{n=40}-\omega_{J''\rightarrow J'})^2}{2\Gamma^2_{J''\rightarrow J'}}}}_{\text{Groundstate transitions } \omega_{J''\rightarrow J'}}. \tag{2.1}$$

This fit is exemplified at the shaded areas in the spectra shown in figure 2.7 for $n = 40$. The spectra are the ones, where the data points at NO:He= $0.25 \cdot 10^{-4}$ in figure 2.8 b) were extracted.
The fitted width of the $\omega_1$ laser is $\Gamma_{\omega_1} = 0.03$ nm, which also has a contribution of the $\omega_2$ laser. The width of the transitions were determined by the fit to $\Gamma_{J'' \to J'} = (0.0023 \pm 0.0004)$ nm and the relative position of the $\omega_1$ laser is written into the insets of figure 2.7, where also the fit itself is plotted.
Although this estimation is very crude, it nevertheless shows that the position of the $\omega_1$ laser has a large impact on the Rydberg lineshape and therefore especially on the maximum value of the Rydberg line. It is therefore a major source of the large variances observed during the experiments, that are presented in the following section 2.3.4.

### 2.3.4 A proof of concept for a gas sensor

In order to test the applicability and the limits of a Rydberg excitation based gas sensor for NO, different dilutions of NO to He are prepared. As explained in section 2.2.2, Rydberg spectra are recorded, such as the ones shown in figure 2.8 a). In between each sample preparation the whole setup was evacuated. For further analysis the maximum value of the Rydberg peak at $n = 40$ was evaluated.

**Constant pressure** First, different dilutions are examined at a constant pressure of 11 mbar. Examples are depicted in figure 2.8 a). Clearly, all spectra look very similar apart from the decreasing amplitude for thinner dilutions. Unfortunately, there is also a Rydberg spectrum visible for a presumably evacuated cell. This can be attributed to the outgassing of NO as was discussed in section 2.2.3. This outgassing prohibits the preparation of any dilution thinner than 10 ppm and sets a technical limit to the characterization of our sensor scheme.
In figure 2.8 b) the maximum of the peak at $n = 40$ is plotted for each dilution. The maximum value decreases for decreasing concentrations of NO to He, which is what one expects from a gas sensor. Unfortunately, the spread of the maxima is very large, which is attributed again to the sample preparation as discussed in section 2.2.3. Another reason for the variances is given by the insufficient linewidth and positioning of the lasers as explained in section 2.3.3.

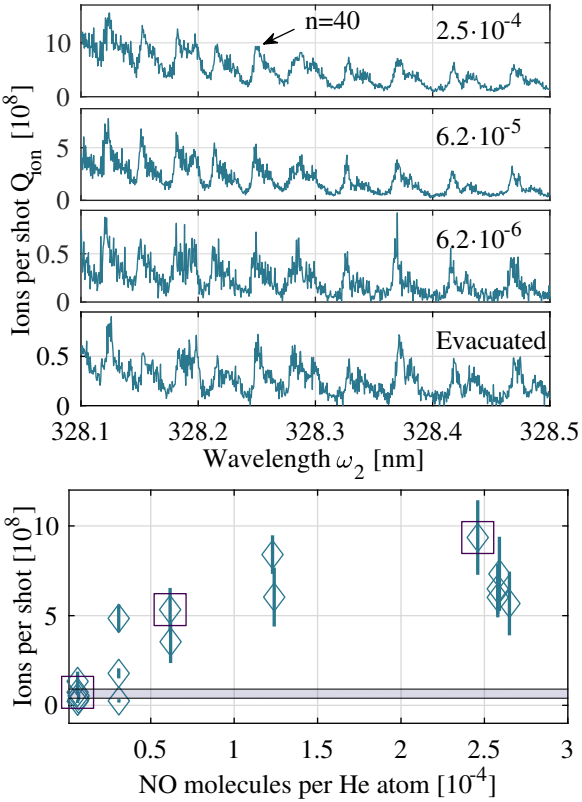


**Figure 2.8:** a) Rydberg spectra from $n = 35$ to $n = 44$ of NO in a mixture with He with different concentration ratios NO:He at a pressure of 11 mbar and room temperature. The last spectrum was recorded in a cell which was presumably evacuated. These are the spectra from which the data points in b), marked with squares, were extracted. b) Number of ions at each laser shot as function of the concentration of NO to He at a pressure of 11 mbar. The horizontal beam represents the number of charges measured for a cell, which was presumably pumped empty. The spectra of the data points marked with squares are shown in a).

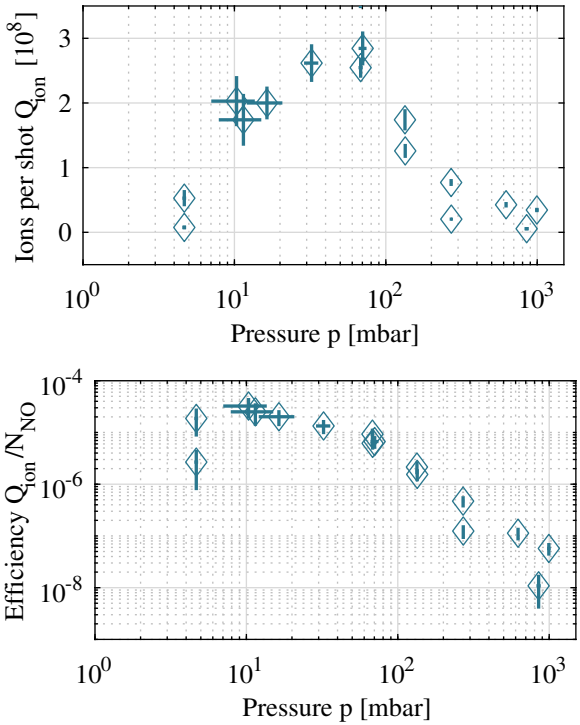


**Figure 2.9:** a) Number of charges measured at each laser shot as function of the pressure for a single dilution consisting of $2.0 \cdot 10^{-5}$ NO molecules per He atom. b) Efficiency calculated from a) as the ratio of the number of charges and the number of NO molecules presumably present inside the excitation region.

**Constant concentration** Taking now a single dilution NO:He = $2.0 \cdot 10^{-5}$ and varying the overall pressure of the mixture, a graph as depicted in figure 2.9 a) is obtained. Here, the number of charges $Q_{ion}$ as function of the pressure $p$ is plotted. From the pressure and the known concentration one can calculate the number of NO molecules being present inside the excitation volume, under the premise that no NO is outgassing or adsorbing. From this molecule number and the number of charges, the excitation efficiency $Q_{ion}/N_{NO}$ is calculated, which is plotted in figure 2.9 b) as function of the pressure. With the use of such a graph and figure 2.8 b) one can estimate how many charges one can expect at least for a certain dilution at some pressure.
Interestingly, the excitation efficiency changes over 2.5 orders of magnitude over a pressure range from 4 mbar up to 1000 mbar. The excitation efficiency increases first due to an increasing amount of collisional partners, such as charges and other Rydberg atoms. It then decreases again for higher pressures. This is a result of collisional deexcitation of the intermediate state but also due to recombination of charges during their flight time to the electrodes.

**Arrival time** Both effects can be observed directly at the single voltage traces $U_{out}$ shown in figure 2.10. After an excitation pulse, charges close to the electrodes arrive very rapidly with a risetime of 4 $\mu$s, which is well covered by the bandwidth of the employed TIA. The tail after this sharp rise is due to charges from further away from the electrode. For higher pressures this tail shifts to longer times as a result of the decreasing mean free path length of the ions inside the backgroundgas. During this flight time they also have the chance for more recombination processes, which decreases the relative amplitude of the tail to the first sharp peak. Moreover, the decrease of the first peak itself can be attributed to an overall decline of the excitation efficiency.

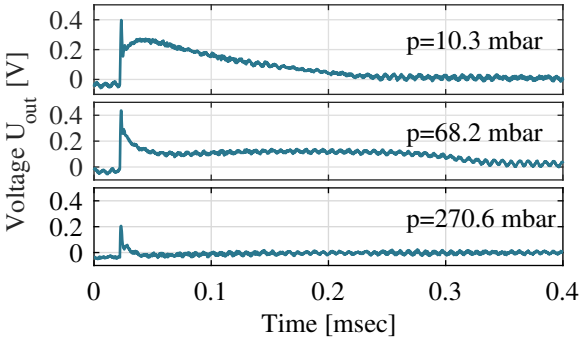


**Figure 2.10:** Voltage $U_{out}$ at the output of the TIA as function of time for different pressures of the same dilution.

## 2.4 Conclusion

### 2.4.1 Estimation of the detection limit

An interesting question is to see how good the excitation efficiency could become at most. The main portion of molecules no longer available to the Rydberg excitation is coming from the thermal distribution of the molecules' groundstate X $^2\Pi_{1/2}$ across the rotational levels $J$. The fraction of molecules populating the $J = 1/2$ state of X $^2\Pi_{1/2}$ state can be estimated using [79]

$$\frac{hcB}{k_B T}(2J+1)e^{-BJ(J+1)hc/k_B T}. \tag{2.2}$$

The population of higher vibrational levels at $T = 300$ K is only 0.14 ‰ and can thus be neglected [79]. The rotational constant is given by $B = 1.671854$ cm$^{-1}$ [98] and $k_B$ denotes the Boltzmann constant. This yields a fraction of 1.6 % of molecules in the lowest rotational groundstate. Only half of those molecules have spin $-\frac{1}{2}$ and for a pulsed excitation, which is not coherent, at most one fourth of the molecules can be excited to the Rydberg state. Consequently the maximally achievable efficiency is 0.2 %, as long as the

$\omega_1$ laser populates only one single intermediate state, the collisional ionization probability stays one and there are no recombination processes occurring.
The maximally achieved efficiency in figure 2.9 is about a factor of one hundred less than the theoretically possible value. Reasons are on the one hand the uncertainty in the absolute amount of NO owing to the sample preparation. Another reason is the huge linewidth of the lasers. Not all spectral energy is available at the comparably narrow transitions. Additionally it is possible that not all Rydberg molecules are actually ionized by predissociation or collisions. This is very similar to the experiment on Rb in the next chapter 3.
Still, an efficiency of approximately $10^{-7}$ was achieved at room temperature and ambient pressure. For a practical application such as breath analysis, a volume flow of exhaled breath of 50 ml/second is recommended [52]. This volume flow corresponds to a particle flow of $1.2 \cdot 10^{21} \frac{1}{\mathrm{s}}$ at 1 bar and 300 K. With the measured Rydberg excitation efficiency, shown in figure 2.9, and a minimum detectable current of 100 fA with the employed amplifier, which is far above the noise floor[2], a detection limit of 5 ppb could in principle be achieved at the flow rate mentioned above. Of course under the prerequisite of taking into account only signals with a frequency comparable to the design bandwidth of the amplifier.

### 2.4.2 Possible improvements

There are two obvious improvements. The characterization of the detection limit was unfortunately limited by the gas mixing setup. A mixing setup based on through-flow is therefore more suitable. Also, avoiding stainless steel parts and electrodes not made from a transition metal is favorable.
Another issue is the large linewidth of the employed lasers. Not only in terms of the shape of the Rydberg lines, but such a broad laser could in the end diminish the selectivity of the gas sensing scheme. Much smaller linewidths can be achieved by employing solid state based cw lasers. A cw excitation would also relax the requirements on the bandwidth of the TIA, which in turn would allow for higher amplification and hence lower noise. This is explained in chapter 6. In terms of signal processing a pulsed excitation is anyway not

[2] In chapter 1 and in chapter 6 it becomes evident that the employed amplifier showed a much higher current noise. The reasons are explained in chapter 6. The minimum detectable current estimate of 100 fA is extracted from [74] and applies to an ideal implementation of the amplifier at the design bandwidth.

favorable, since the actual signal is arriving only during a very short period of time, whereas there are long times where nothing is happening at all. Here 0.4 $\mu$s signal length compared to an overall 100 ms time period of the pulsed dye lasers.
In a cw excitation also modern signal processing tools, such as Lock-In amplification of the signal can further improve the signal quality. This might also help to get rid of a constant Rydberg-unrelated offset caused by multi-photon ionization of organic molecules by the $\omega_1$ laser. A possible excitation path, which also omits the use of the very energetic 328 nm $\omega_2$ laser could look like this: X $^2\Pi_{1/2} \rightarrow$ A $^2\Sigma \rightarrow$ H $^2\Sigma^+ \rightarrow$ nl [99]. Then one of the upper two lasers, which have wavelengths of 540 nm and 833 nm could be used to modulate the amplitude of the Rydberg signal.
Although the setup and the lasers employed in this experiment made it nearly impossible to characterize the gas sensing scheme in every detail, this experiment still serves as a proof of principle for our proposed gas detection scheme. Further analysis of our gas sensing method is done in the next chapter 3 on an idealized system, where cw lasers and a well-defined sample preparation are possible.

# 3 A gas sensor for rubidium

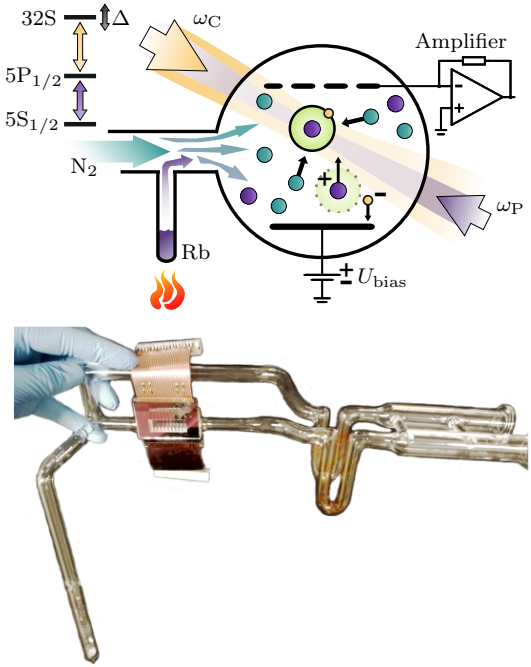


**Figure 3.1:** Top: Schematic of the Rb gas sensor. Rb is being evaporated from a reservoir and diffuses through the $N_2$ background gas into the excitation region. There it is excited to a high lying Rydberg state using the two excitation lasers $\omega_P$ and $\omega_C$. The Rydberg atoms collide with molecules of the background gas and ionize. The background gas is in the present experiment $N_2$. The emerging charges are driven towards the electrodes with the help of a small electric bias field. The charges are then detected as a current. Bottom: Picture of the glass cell. One of the two glass pipes on the right is the inlet for the background gas. The other one is shut close with a valve for the course of a measurement and is opened for evacuating the glass cell. The glass tube on the left is the Rb reservoir.

## 3.1 Rydberg excitation of Rb

In the following chapter, the most basic fundamentals of atom-light interaction is repeated in a very abbreviated manner in order to understand the analysis of the recorded data.

### 3.1.1 Groundstate population

Aiming to determine the density of atoms inside the excitation region, the absorption of light resonant to hyperfine transitions from the $5S_{1/2}$ state to the $5P_{1/2}$ state of $^{85}$Rb is examined. The intensity $I$ of light after traversing a medium with absorption coefficient $\alpha$ is given by the Lambert-Beer equation

$$I(x) = I(0) \cdot e^{-\alpha \cdot x}. \tag{3.1}$$

The absorption coefficient is in general related to the density of atoms $n$ and their ability to scatter light at a certain detuning $\delta$,

$$\alpha(\delta) = n \cdot \sigma(\delta), \tag{3.2}$$

where $\delta = \omega - \omega_0$ denotes the detuning of the excitation light from the atomic resonance.
The density can be determined by considering the following: In a thermal vapor, atoms moving towards or away from the propagation direction of the excitation light experience the light at a different frequency $\omega' = \omega - \mathbf{kv}$. This is known as Doppler effect. The density of atoms moving with a certain velocity and hence being resonant to the light field at a certain detuning is given by a Gaussian distribution with a temperature dependent width of $\omega_D$

$$\begin{aligned} n(\delta) \cdot d\delta &= n_0 \cdot \sqrt{\frac{m}{2\pi k_B T}} \cdot e^{-\frac{m}{2k_B T} \cdot \frac{c^2 \delta^2}{\omega^2}} \cdot \frac{c}{\omega} \cdot d\delta \\ &= n_0 \cdot \sqrt{\frac{ln(2)}{\pi}} \cdot \frac{2}{\omega_D} \cdot e^{-4ln(2)\frac{\delta^2}{\omega_D^2}} \cdot d\delta. \end{aligned} \tag{3.3}$$

In order to evaluate the absorption coefficient $\alpha$ in equation (3.2) the scattering cross section needs to be calculated. The scattering cross section of an atom

for small light intensities is also a function of the detuning $\delta$ and is given by a Lorentzian lineshape with a width $\Gamma$

$$\sigma(\delta) = \frac{\sigma_0}{1 + 4\left(\frac{\delta}{\Gamma}\right)^2}. \tag{3.4}$$

The complete absorption coefficient in equation (3.2) as a function of the detuning $\Delta$ of the excitation laser is now given by the integral over all possible Doppler detunings $\delta$: $\alpha(\Delta) = \int_{-\infty}^{\infty} (n(\Delta - \delta) \cdot \sigma(\delta))\, d\delta$. This convolution of a Lorentz function (equation (3.4)) with a Gauss distribution (equation (3.3)) will yield a Voigt profile, which has to be summed up for all possible hyperfine transitions of the two Rb isotopes

$$\begin{aligned}\alpha(\Delta) =& n_0\sigma_0\frac{\pi\Gamma}{2} \cdot \sum_{F,F'} \left[ \frac{(2F+1)(2F'+1)(2J+1)}{2(2I+1)} \cdot \left\{ \begin{array}{ccc} J & J' & 1 \\ F' & F & I \end{array} \right\}^2 \right] \cdot \\ & \int_{-\infty}^{\infty} \left( \sqrt{\frac{ln(2)}{\pi}} \cdot \frac{2}{\omega_D} \cdot e^{-4ln(2)\left(\frac{\Delta-\delta}{\omega_D}\right)^2} \cdot \frac{\frac{2}{\pi\Gamma}}{1 + 4\left(\frac{\delta}{\Gamma}\right)^2} \right) d\delta \Bigg].\end{aligned} \tag{3.5}$$

The atomic density of both Rb isotopes can be obtained by fitting this function to a recorded Rb groundstate spectrum. The whole sum including the Voigt profile will by definition equal 1. The resulting amplitude $n_0\sigma_0\frac{\pi\Gamma}{2}$ of the spectrum is directly proportional to the joint groundstate density of both Rb isotopes. The width $\Gamma$ is given by the fit and the resonant scattering cross section $\sigma_0$ can be found in [100] for example.

### 3.1.2 3-Level System

The time evolution of a quantum mechanical system including decoherence is in general given by the Liouville-von Neumann equation

$$\frac{\partial \varrho}{\partial t} = -\frac{i}{\hbar}[H, \varrho] + \hat{L}(\varrho), \tag{3.6}$$

where $\varrho$ is the density matrix describing the state of the system, $H$ is the Hamilton operator determining the time evolution and the energy eigenstates

and $\hat{L}$ is the Lindblad operator describing energy conserving as well as non-energy conserving decoherence mechanisms:

$$\hat{L}(\varrho) = \sum_{i,j} \Gamma_{i,j} \left( \hat{C}_{i,j} \varrho \hat{C}_{i,j}^{\dagger} - \frac{1}{2} \left( \hat{C}_{i,j}^{\dagger} \hat{C}_{i,j} \varrho + \varrho \hat{C}_{i,j}^{\dagger} \hat{C}_{i,j} \right) \right). \tag{3.7}$$

Here $\Gamma_{i,j}$ is the decay from the state $|i\rangle$ to $|j\rangle$ and $\hat{C}_{i,j} = |i\rangle\langle j|$ is the transition operator.
In order to theoretically estimate the population of atoms in the Rydberg state, the present system is modeled as a 3-level system. The groundstate $|1\rangle$ is coupled to the intermediate state $|2\rangle$ via the probe laser light $\omega_P$ with a Rabi frequency $\Omega_P = d/\hbar \cdot E_0$, with the transition dipole matrix element $d$ and the light field $E_0 = \sqrt{2I/(\epsilon_0 c)}$ and the detuning $\Delta_P$. The intermediate state couples to the Rydberg state $|3\rangle$ with the coupling laser light $\omega_C$ in the same way with a Rabi frequency $\Omega_C$ and a detuning $\Delta_C$. The Hamiltonian of such a system is a sum of the Hamiltonians for the light field, the atom and the atom-light interaction. After a shift in energy and by neglecting fast oscillating parts of the electric field the Hamilton operator reduces to

$$H = \begin{pmatrix} 0 & \Omega_P/2 & 0 \\ \Omega_P^*/2 & -\Delta_P & \Omega_C/2 \\ 0 & \Omega_C^*/2 & -(\Delta_P + \Delta_C) \end{pmatrix}. \tag{3.8}$$

Only the natural linewidth $\Gamma_{21} = 5.75\ 2\pi \cdot \mathrm{MHz}$ is considered as decay of the intermediate state into the groundstate. Similarly, $\Gamma_{31} = \Gamma_{ion}$ is the decay of the Rydberg state directly into the groundstate. In principle this direct decay is unphysical. One could as well introduce a fourth vacuum level, which is populated by the decay of $|3\rangle$. The $|4\rangle$ state would then decay into the groundstate $|1\rangle$ via a transit time decay. This represents a loss and gain of atoms in the excitation region due to their thermal motion. This decay will be explained further in chapter 4. Only a 3-level system is regarded due to its simplicity and because the results are indistinguishable from a 4-level system modeled in the described manner. The decay rate $\Gamma_{31}$ is determined from a fit with a Lorentz function to the Rydberg spectra. This will be explained in section 3.3.2 and possible broadening mechanisms will be explained in chapter 4.
The population of the Rydberg state $\varrho_{33}$ is determined by numerically solving equation (3.6). Comparable to the case of the moving groundstate atoms, a Gaussian weighted summation over all velocity-induced detunings

$\Delta_P = -k_P \cdot v, \Delta_C = k_C \cdot v$ has to be calculated. The overall relative population of the Rydberg state $\varrho_{33}$ is hence effectively decreased. The density of atoms moving with the velocity $v$ is given by

$$n(v,T) = \sqrt{\frac{m}{2\pi \cdot k_B \cdot T}} \cdot e^{\frac{-m \cdot v^2}{2 \cdot k_B \cdot T}}. \tag{3.9}$$

Of those atoms again only a fraction is excited to the intermediate state $|2\rangle$. This is because of the degeneracy of the Zeeman sublevels $m_F$ of the hyperfine groundstate transitions, which are still equally populated. With the linearly polarized excitation light only a fraction of transitions is possible. For the transition $5S_{1/2}, F = 3 \rightarrow 5P_{1/2}, F = 2$ only 7/12 of the whole $^{85}$Rb atomic density can therefore be addressed. For all presented analysis the relative Rydberg population $\varrho_{33}$ determined in the described manner is used. The following experimental parameters are fed into the calculation: the width of the Rydberg line as decay of the Rydberg state and also as ionization rate, the two Rabi frequencies, the temperature and also the excitation volume given by the diameters of the excitation lasers and the extension of the glass cell into the direction of the light propagation.

## 3.2 Experimental setup

### 3.2.1 Laser system

Rydberg states are excited by first driving transitions from the $5S_{1/2}, F = 3$ groundstate to the $5P_{1/2}, F = 2$ intermediate state using cw laser light $\omega_P$ at 795 nm. The involved transitions are depicted in figure 3.2. This light is emitted by a grating-stabilized laser diode. The laser is stabilized onto an ultrastable reference cavity. The laser beam passing through the excitation region has an $1/e^2$ diameter of 1.25 mm. A Rabi frequency of $\Omega_P = 4.3\ 2\pi \cdot$ MHz is used for the groundstate spectroscopy, which is more than ten times below the saturation intensity. This Rabi frequency is calculated for a power $1/e^2$ less than the peak power measured with a power meter in correspondence with the diameter measured with a knife edge.

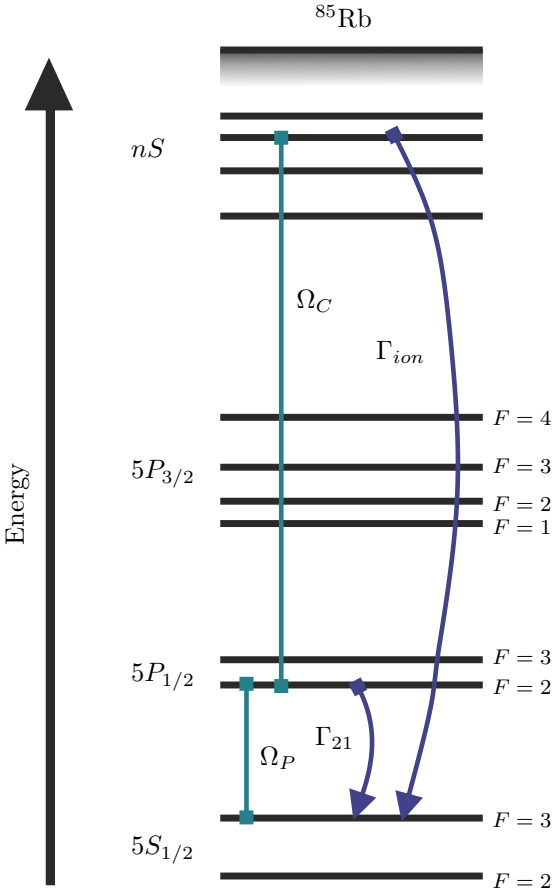


**Figure 3.2:** Level scheme of Rb for the transitions involved in this experiment.

During the Rydberg excitation, a Rabi frequency of $\Omega_P = 9.6\ 2\pi \cdot \mathrm{MHz}$ is used for $\omega_P$. This is sufficient to saturate the overall Rydberg population, for the given low Rabi frequency of $\omega_C$, but yet no power broadening of the Rydberg line is observable. Consider here also figure 1.5 in chapter 1 and the discussion in section 4.1.
The transition from the $5P_{1/2}, F = 2$ intermediate state to the $32S$ Rydberg state is driven by $\omega_C$, which is cw laser light at 474 nm. This light is emitted by a grating-stabilized laser diode, which is frequency doubled in a bow-tie cavity after amplification by a tapered amplifier. The laser frequency is referenced onto the same ultrastable cavity. The laser beam has an $1/e^2$ diameter of 1.06 mm and a Rabi frequency of $\Omega_C = 4.8\ 2\pi \cdot \mathrm{MHz}$, which is limited by the output power of the laser system.
The big advantage of this laser system over the system employed for the excitation of NO in chapter 2 is a linewidth of less than 100 kHz for the free-running laser. The disadvantage is the low output power though, which does not allow a saturation of the Rydberg transition. Compare here again to figure 1.5 in chapter 1. As a result, the excitation efficiency will suffer from fluctuations of the Rabi frequency $\Omega_C$ mainly caused by absorption of light at macroscopic Rb droplets on the cell windows. Additionally, the true detection limit and the highest possible sensitivity can not be achieved.

### 3.2.2 Glass cell and current detection

A picture of the glass cell, used for this experiment, is shown in figure 3.1. The frame has a thickness of 10 mm, which is also the distance of the electrodes deposited onto the two glass substrates attached to this frame. This gives a limit to the excitation volume in the propagation direction of the excitation light, such that the overall excitation volume is only 8.8 $\mathrm{mm}^3$ small. The whole cell is placed inside an oven where the glass pipe acting as a reservoir is heated independently.
The employed amplifier is an external one (DL Instruments Model 1211) connected to the glass cell via shielded flat ribbon cables. A more detailed analysis of the noise properties can be found in chapter 6. The high input capacitance including the low bandwidth of the amplifier restricts the scan speed of the Rydberg spectroscopy to 1 Hz for a frequency span of 3 GHz for $\omega_C$. In order to guide the Rydberg created charges towards the electrodes a small electric bias field of $-2.6$ V/cm was applied with respect to the amplifier's input. This

field is sufficient to maximize the amount of charges arriving at the electrodes without inducing a resolvable Stark shift on the Rydberg transition (see here also the discussion in chapter 4). Care was taken that no space charge distribution diminishes the shape of the Rydberg signal as is intensively discussed in [20] and mentioned in chapter 4.

### 3.2.3 Gas mixing

The gas mixture of $N_2$ and Rb is prepared by slowly filling the cell with $N_2$ through a massflow controller at a rate of 0.12 ml/min. At the same time Rb is evaporated from a glass manifold [101] at a temperature of around 90 °C, while the oven in which the whole cell is placed was held at a temperature of around 100 °C. This experimental strategy of mixing the alkali metal with the buffer gas turned out to be not beneficial. The alkali metal needs to diffuse through the background gas [102, 103]. At higher buffer gas pressures, the metal is therefore more likely to condense onto the glass walls than to fly into the excitation region. Hence, the partial pressures of the two dilution components can not be set independently. As a consequence also the speed at which the $N_2$ is filled into the cell is crucial for the final Rb:$N_2$ density ratio. This can be seen in figure 3.3[1]. For slower filling speeds the Rb evaporation

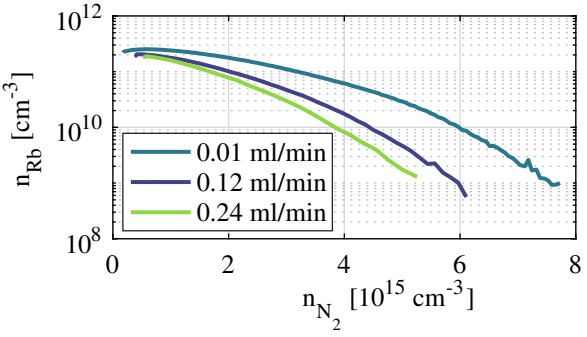


**Figure 3.3:** Rb density as function of the $N_2$ density for different filling speeds of the cell with $N_2$.

[1] Whenever the Rb density is mentioned, the density of $^{85}$Rb atoms is meant. This applies to all data shown in this thesis.

rate is sufficient to counteract the condensation rate onto the cell walls. A quantitative estimation is not possible due to the complicated cell geometry. In chapter 4 the consequences of this effect will be discussed further.
One possibility to lower the dependence of Rb density on the $N_2$ density is to bring the reservoir even closer to the excitation region, e.g. directly underneath at a third entrance to the cell.
The $N_2$ density is determined by the measurement of the temperature inside the oven (temperature sensor DS18B20) and the pressure measured with a Pirani gauge.

## 3.3 Experiment and results

The following data was taken over the course of one month. During this time the experimental setup and especially the heating temperatures were not changed. At the end of the month the Rb density began to shrink. An intended overheating of the reservoir led to an increase of photocurrent and a further decrease of the Rydberg current due to visible condensation of metallic Rb onto the cell walls. This condensation process was presumably already ongoing before and is most likely the explanation for the statistical spread in the Rydberg current data.
The experiment was always performed like this: First the cell was slowly filled with $N_2$. During this filling groundstate spectra were recorded. As soon as no absorption was visible anymore, the cell was pumped empty again and the filling was started from the beginning. But this time Rydberg spectra were recorded during the filling process. This allows to correlate the measured Rydberg current with the Rb density. Or in other words: the groundstate spectroscopy serves as a characterization tool for the Rydberg gas sensing scheme. Only succeeding data sets of groundstate and Rydberg spectra were correlated for the analysis. One complete experimental cycle took about 20 minutes.
The most basic properties of the experiment are listed below in table 3.1.

**Table 3.1:** Summary of the most relevant properties of the experiment.

| | $5S_{1/2}, F = 2 \rightarrow 5P_{1/2}, F = 3$ | $5S_{1/2}, F = 2 \rightarrow 5P_{1/2}, F = 3 \rightarrow 32S$ |
|---|---|---|
| $\Omega_P$ | 4.3 $2\pi \cdot$ MHz | 9.6 $2\pi \cdot$ MHz |
| $\Omega_C$ | | 4.8 $2\pi \cdot$ MHz |
| $n_{Rb}$ | $(10^9 - 7 \cdot 10^{10})$ cm$^{-3}$ | |
| $n_{N_2}$ | $(0.5 \cdot 10^{15} - 3.5 \cdot 10^{15})$ cm$^{-3}$ | |
| $\Gamma_{ion}$ | $(3.4 \cdot 10^{-15} \cdot n_{N_2}[\text{cm}^{-3}] + 10.8)$ $2\pi \cdot$ MHz (see also chapter 4) | |

### 3.3.1 Groundstate spectrum

Different Rb groundstate spectra are shown in figure 3.4 a) for different $N_2$ densities. Obviously there is barely any absorption visible for Rb:$N_2$ concentrations lower than $7.0 \cdot 10^{-7}$. Hence, also a fit of equation (3.1) to such a spectrum is not reliable anymore and is discarded if the density values and its associated error become too large. In figure 3.5 the density of Rb atoms is plotted as function of the $N_2$ density extracted according to equation (3.5) from a fit to the groundstate spectrum. As explained in section 3.2.3 the Rb needs to diffuse from the reservoir to the excitation region. For larger $N_2$ densities the mean free path length decreases and hence Rb can not be refilled with a rate larger than the rate of Rb condensing onto the glass walls. A change in the width can not be determined reliably, since the Doppler broadening is on the order of GHz and the expected increase in width is on the order of 2.3 $2\pi$·MHz/mbar. See also the discussion in chapter 4.
During the scope of this thesis several attempts have been made to investigate possible loss mechanisms in the first excited state $5P_{1/2}, F = 2$. These losses would directly transfer to the maximum possible Rydberg population and would hence inevitably limit the gas sensing scheme. This was the objective of the Master thesis of Ralf Albrecht [104]. The key results are summarized in chapter 4. For the density range considered for this experiment the contribution of pressure induced groundstate losses are negligible. The overall broadening is at most 1.0 $2\pi$·MHz of which only 0.2 $2\pi$·MHz lead to actual losses in the intermediate state.

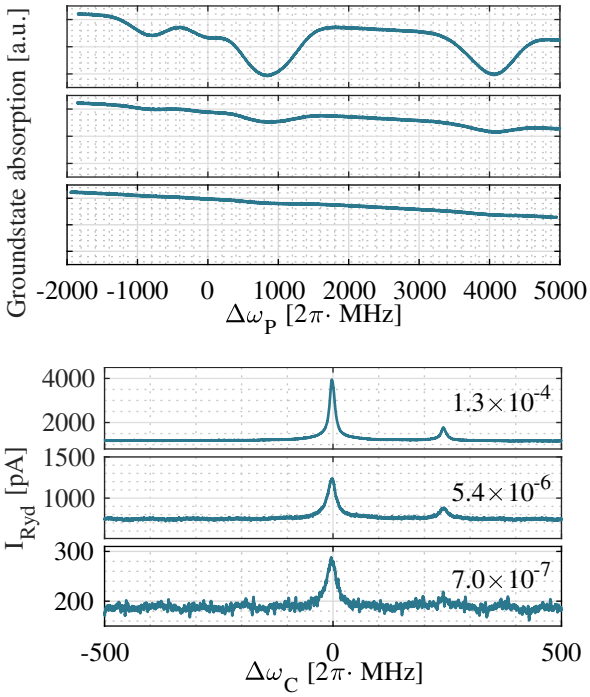


**Figure 3.4:** a) Different groundstate spectra and b) Rydberg current spectra as function of the detuning $\Delta$ of $\omega_P$ and $\omega_C$ respectively for different ratios of Rb:$N_2$. The density ratios are written inside the Rydberg spectra.

### 3.3.2 Rydberg spectrum

The Rydberg current spectra corresponding to the same dilution ratios as the groundstate spectra are plotted in figure 3.4 b). There are three different things to discuss on these spectra.

**Next hyperfine transition:** Next to the main $5S_{1/2}, F = 3 \rightarrow 5P_{1/2}, F = 2 \rightarrow 32S$ transition appears a second smaller peak. This peak is emerging from atoms moving towards the propagation direction of the $\omega_P$ light, which are resonant to the $5S_{1/2}, F = 3 \rightarrow 5P_{1/2}, F = 3$ transition due to the Doppler

effect. The transition $5S_{1/2}, F = 3 \rightarrow 5P_{1/2}, F = 3$ is $\delta_P = 361\ 2\pi \cdot$ MHz below the resonant $5S_{1/2}, F = 2 \rightarrow 5P_{1/2}, F = 3$ transition. Therefore the atoms need to move with a velocity $v = \delta_P / k_P$ towards the $\omega_P$ laser. The same atoms experience the coupling light $\omega_C$ detuned by $\delta_C = -k_C \cdot v$. The coupling frequency at which these moving atoms can be seen is hence $\Delta_2 = \delta_C + \delta_P = -k_C \frac{\delta_P}{k_P} + \delta_P = -241\ 2\pi \cdot$ MHz further away from the resonant $5S_{1/2}, F = 3 \rightarrow 5P_{1/2}, F = 2 \rightarrow 32S$ Rydberg line.

**Photocurrent:** All Rydberg spectra show an offset current. This current is due to the photoeffect caused by the blue $\omega_C$ light. The blue photons have an energy of 2.6 eV. In comparison, Rb has a workfunction of only 2.2 eV in the metallic bulk [105]. For thinner dilutions this current emerging from Rb sticking to the cell walls decreases. The photocurrent caused by Rb is discussed in-depth in [20].

**Lorentz fit:** The amplitude of the Rydberg created current without the photocurrent offset is determined by fitting a Lorentz function to the spectra. We observed that the width of the Rydberg peak is not reproduced sufficiently by just one Lorentz function. Since the probe laser light $\omega_P$ is very intense, a small reflection on the order of 4% at the second cell window led to an overlap of two Lorentz functions: One for the counter-propagating configuration of $\omega_P$ and $\omega_C$, the other one for the co-propagating case caused by the back reflection of $\omega_P$. For the following analysis, only the resulting amplitude and width of the much larger Lorentz peak for the counter-propagating case is taken into account.

Further investigations on the lineshape, including possible pressure induced loss mechanisms and especially the width of the Rydberg signal, will be part of section 3.3.3 and chapter 4.

### 3.3.3 A proof of concept for a gas sensor

The main properties of the gas sensing scheme based on Rydberg excitations are discussed now. In contrast to chapter 2 this analysis is no longer restricted to a proof of principle experiment, but properties such as the detection limit, the linearity and efficiency and also the signal to noise ratio are investigated.

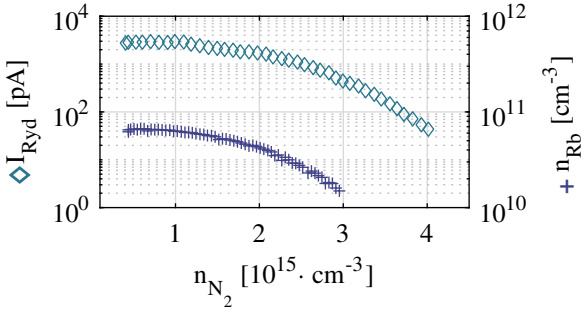


**Figure 3.5:** On the left axis marked with diamonds: Amplitude of a Lorentz function fitted to the Rydberg current spectra as function of the $N_2$ density. On the right axis marked with crosses: $^{85}$Rb density as function of the $N_2$ density determined by fitting equation (3.1) to the groundstate spectra.

**Detection limit** From measurements exemplary shown in figure 3.4 the amplitude of the electrical current and the Rb density can be plotted. This is depicted in figure 3.5. From such a plot the current as function of the $N_2$ density can be correlated to the Rb density as function of the $N_2$ density. Unfortunately, this implies that all properties of the gas sensor are limited by the quality of the determination of the Rb density, which was done using purely optical groundstate spectroscopy.
It is nevertheless remarkable to see that the current signal continues further on for higher $N_2$ densities, further than the optical determination of the Rb density.
This can be achieved by using sufficiently intense light fields for $\omega_P$, such that the groundstate transition remains saturated for all $N_2$ densities and by applying as strong light fields as possible on the Rydberg transition. As mentioned

in the beginning of this section 3.3, the condensation of Rb led to a visible obstruction for the excitation lasers. This prohibited the application of high Rabi frequencies for most measurements, because the $\omega_C$ light was scattered already at the first entrance glass window. Therefore the current signal oftentimes did not continue further on compared to the groundstate spectroscopy. Nevertheless, if a constant heating was applied to the Rb reservoir and a steady $N_2$ flow of 0.12 ml/min was maintained, the layer of bulk Rb on the walls showed only small changes, such that the overall properties of the gas sensor remained unchanged in the limits of statistical errors. This is confirmed by the measurements plotted in the following, which were taken over the course of a whole month. As mentioned before, all analysis is restricted by the lowest Rb density that is still quantifiable with the groundstate spectroscopy.

**Linearity and Efficiency** In figure 3.6 a) the amplitude obtained from fitting a Lorentz function to the Rydberg spectrum is plotted as function of the Rb density, which is extracted from correlating the current measurement to a groundstate spectroscopy. The color code indicates the $N_2$ density. The statistical spread towards low Rb densities is caused by the increased difficulty to reliably determine the Rb density from the groundstate spectroscopy. Another reason leading to fluctuations in the amplitude $I_{Ryd}$ rather than in the density $n_{Rb}$ are fluctuations of the $\omega_C$ Rabi frequency $\Omega_C$. Since the laser power is not sufficient to saturate the Rydberg population small variations already translate into fluctuations in the amplitude of the current signal. These fluctuations can be caused for example by intensity fluctuations in the fiber guiding the laser light to the experiment. Another source of intensity variations is scattering at bulk Rb condensing onto the walls of the glass cell, as was mentioned before.
In order to access the detection efficiency theoretically, the current per Rb atom is calculated by solving the Liouville-von Neumann equation (3.6) for a 3-level system. As explained in section 3.1.2, the width of the Lorentz function fitted to the Rydberg spectra is used as decay rate $\Gamma_{ion}$ of the Rydberg state $|3\rangle$. From equation (1.9) it is known that $\varrho_{33} \cdot \Gamma_{ion} \cdot e = \frac{I}{n \cdot V}$ holds.
The theoretical prediction is plotted on the right axis of figure 3.6 b) as function of the $N_2$ background gas density. As explained in section 3.1.2, the width of the Rydberg line as decay of the Rydberg state and also as ionization rate, the Rabi frequencies, the temperature and also the volume determined from the experiment are fed into this calculation. However, since contributions of possible broadening mechanisms, that do not lead to an ionization, are not

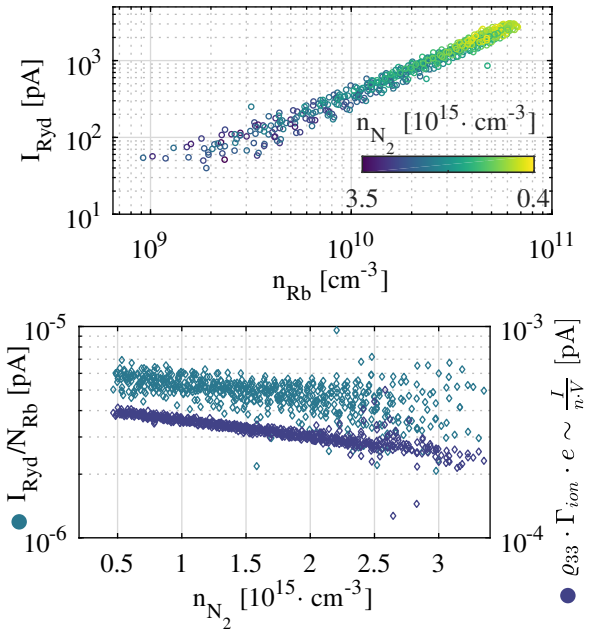


**Figure 3.6:** a) Amplitude of the Rydberg current signal as function of the Rb density. The color code indicates the $N_2$ density. b) Current per number of $^{85}$Rb atoms as function of the Rb density. On the left axis, the experimental data and on the right axis the theoretical prediction is shown. Compare here also figure 1.4 in chapter 1.

subtracted, this is an upper estimate of the theoretically achievable current. The experimentally determined amount of current per Rb atom is plotted on the left axis. Here $N_{Rb}$ denotes the amount of all $^{85}$Rb atoms inside the excitation volume.

The ratio of both curves or in other words, the ratio of the measured current to the theoretically expected current, is the detection efficiency. That is the efficiency at which the charges are collected in the experiment without taking into account contributions arising merely from the shrinking excitation efficiency. This detection efficiency is plotted in figure 3.7 a) for the case of $N_2$. It remains the same for all Rb and $N_2$ densities. This proves that for this experiment possible loss mechanisms do not spoil the linearity of the measurement although they are certainly present.

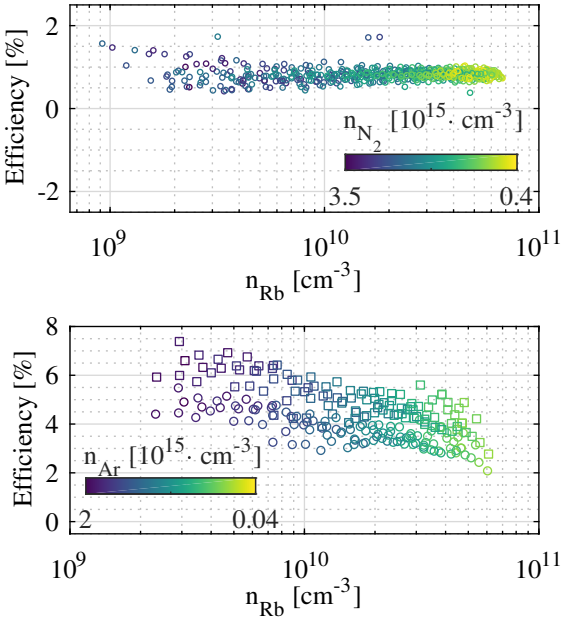


**Figure 3.7:** Efficiency as function of the Rb density calculated by the ratio of the measured current to the theoretically expected current. The theoretically expected current was calculated from solving equation (3.6) for a 3-level system in the steady state. In a) the result is shown for the Rb-$N_2$ system. In b) the efficiency is plotted for the Rb-Ar mixture. The circles depict the efficiency taking into account the complete width of the Rydberg line. The squares are calculated by subtracting the share of elastic collisions from the width of the Rydberg line. This is discussed in detail in chapter 4.

There are several possibilities which might cause the detection efficiency to be only at around 1%. One could assuredly be a charge recombination, comparable to the observation in the NO experiment in chapter 2. Since the efficiency does not change over the investigated range of $N_2$ densities, the increasing recombination possibility at higher background gas pressures does surely not play a major role at the pressures considered here. A very likely reason for the low efficiency is given when one considers that collision events do not necessarily lead to an ionization. The collisional cross section of Rb Rydberg atoms colliding

with $N_2$ molecules leading to ionization is according to [106] about 500 times less than the cross section leading to quenching of the Rydberg state [107, 108]. In this case, $\Gamma_{ion}$ would have been overestimated by far although the general behavior is reproduced well. A more in-depth discussion of the width of the Rydberg spectra is held in chapter 4.

**Signal to noise ratio** A benchmark which is used for the classification of sensors is the response $R$. The response is the output value $A$ at a certain input value compared to the output $O$ of the sensor without an input signal

$$R = \frac{A - O}{O}. \tag{3.10}$$

In the current case, the output signal without input is the off-resonant part of the spectrum, exemplary shown in figure 3.4. As discussed before, the output signal in this part of the spectrum is caused by the photoeffect of the blue coupling light on bulk Rb sticking onto the walls of the glass cell. The response determined in this fashion is plotted in figure 3.8 b). Obviously, the result is not very meaningful. There are several reasons why.
First, the amplitude of the photocurrent changed over time. Consequently, the results are not comparable with each other anymore.
Second, this offset is interlinked with the actual measurement variable. For increasing amount of Rb also the amplitude of the photocurrent will increase. Apart from this, the photocurrent is a problem specific to the Rydberg excitation of alkali metals using this particular excitation scheme. Actually the response is intended for characterizing e.g a gas detector with a variable resistance $A$, where $O$ is the resistance of the sensor without the medium of interest. In the present case, the output of the Rydberg based gas sensor without atoms of interest is zero. Apart from leakage currents caused by a bias field, offset of the current amplifier or its' noise. The response hence is a measure specific for the electro-mechanical realization of the sensor and not the measurement principle in general.

Third, this problem can be circumvented in principle by using e.g. a Lock-in amplifier, which only amplifies the signal correlated to the Rydberg excitation when one modulates the amplitude of $\omega_P$. A Lock-In amplifier was not employed on this experiment due to two reasons. First of all, the transimpedance amplifier does not have a bandwidth large enough. Moreover, this additional device in the signal chain would have made the setup more complex without

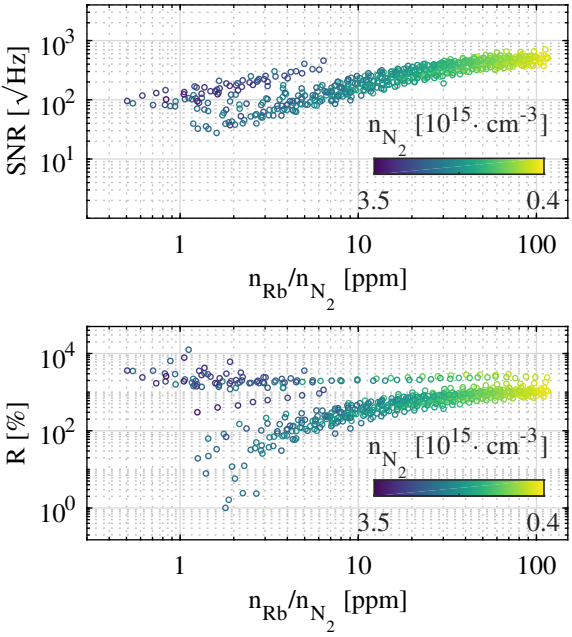


**Figure 3.8:** a) Signal to noise ratio $SNR$ as function of the concentration of Rb to $N_2$. The color code indicates again the $N_2$ density. b) Response as function of the concentration.

providing a gain in signal quality. In fact the main noise source in this experiment at low frequencies is microphonic and ambient noise picked up on the cables connecting the transimpedance amplifier with the cell. Another large contribution to the overall noise is emerging from the large input capacitance caused by the electrodes' capacitance and the capacitance of the wires.
A more meaningful characteristic value of the sensing principle is the signal to noise ratio

$$SNR = \frac{A}{N}. \tag{3.11}$$

The amplitude of the output value $A$ is in the present case given by the amplitude of the Lorentz function fitted to the Rydberg signal. For the amplitude of the noise $N$, the rms noise amplitude is determined. Details on obtaining

the rms noise amplitude is given in chapter 6. In short: The far-offresonant ($\Delta\omega\_C$) part of the Rydberg signal trace is Fourier transformed into the frequency domain, this yields the spectral current noise density. The root mean square of this noise density up to the $1/e$ response time of the utilized amplifier is the rms current noise density.
The resulting signal to noise ratio $SNR$ is plotted in figure 3.8[2]. For an absolute concentration of 1 ppm a change of 10 ppb is still visible and likewise for an concentration of 100 ppm a change of a little more than 100 ppb is observable with an signal to noise ratio of 1.
The sudden increase in $SNR$ is due to the different gain settings used at the amplifier. The noise behavior of transimpedance amplifiers will be further discussed in chapter 6. The SNR still suffers from the disadvantages, which applied to the response $R$. The offset caused by the photocurrent also contributes to the noise by its' shot noise. Therefore, the $SNR$ shows no linear behavior and flattens for large signal values.
Yet, the $SNR$ demonstrates once more that a significant current signal well above the noise floor can be measured although the means of a comparative characterization is not given since no groundstate absorption is visible anymore.
Another characteristic property of a sensor is the sensitivity. That is the response $R$ of the sensor per change in concentration

$$S = \frac{R}{\Delta(n_{Rb}/n_{N_2})}. \tag{3.12}$$

Since it suffers from the same disadvantages as the response and is no more insightful for the present proof of concept experiment, this performance benchmark is not used.

[2]In general the SNR is given as ratio of the power of the signal and the noise. Here, the ratio of the amplitudes was calculated and hence the SNR is not in units of dB

## 3.4 Conclusion

The present experiment serves as an investigation tool to determine the limits of our gas sensing scheme. For this purpose, an experiment on an idealized model system, namely Rb and $N_2$ was set up. The properties and behavior of Rb are well known and it is also known that Rb will interact only weakly with $N_2$. The Rb density as well as the $N_2$ density can be tuned very precisely and can also be optically verified by measurements. Furthermore, there is a complete theoretical framework reproducing the behavior of the sensor. Additionally, the cw excitation enables a precise characterization in terms of noise properties and sensitivity. This makes this experiment a valuable contribution to the already presented sensor for NO.

### 3.4.1 Other background gases

The background gas $N_2$ was chosen, because it is known to interact only weakly with Rb Rydberg atoms. The same gas sensing experiment was repeated with Ar as a background gas. The resulting efficiency is depicted in figure 3.7 b). The circles depict the efficiency taking into account the whole width of the Rydberg line. By quantifying the contribution of elastic collisions to the broadening of the Rydberg line (see chapter 4) one can improve this lower estimate of the efficiency. The total Rydberg population is still deduced from the total width of the Rydberg line, but the collision rate $\Gamma_{ion} = \Gamma_{total} - \Gamma_{elastic}$ is now only dependent on the inelastic contributions to the scattering cross section. Hence, the expected current is given by $I = e \cdot n \cdot V \cdot \varrho_{33}(\Gamma_{total}) \cdot \Gamma_{ion}(\sigma_{total} - \sigma_{elastic})$. This improved estimate is depicted as squares in figure 3.7 b).

### 3.4.2 Possible improvements

There are two ways to further enhance the sensitivity and consequently lower the detection limit. Obviously increasing the Rabi frequency $\Omega_C$ on the upper Rydberg transition will boost the Rydberg signal. In fact, up to 35 % of the Rb atoms can in principle be excited to the Rydberg state with sufficient laser power by using e.g. a pulsed excitation [109]. Attempts have been made to increase the $\Omega_C$ Rabi frequency by employing a laser amplifier. This was the

topic of the Bachelor thesis of Rebecca Schmieg [110]. A blue multi-mode laser diode with an output power of 1 W was seeded by a narrow linewidth master laser. Unfortunately, stabilizing the driving current of the slave diode turned out to be very challenging. Also, the emitted spatial mode was not single mode such that focusing of the emitted light was not feasible. By spatially filtering the light by focusing through a pinhole, 100 mW of output power could be achieved with the master laser seeding with 25 mW. Still, due to the experimental difficulties this approach was abandoned.
The other possibility to improve the gas sensing scheme is to decrease the noise level. One contribution to the overall noise is the photocurrent caused by Rb sticking to the cell walls. This thin metal coating can also lead to a small current driven by the bias voltage from one electrode to the anode connected to the amplifier. In fact, the bias voltage increases also the input voltage noise of the amplifier [111]. Another noise source was already mentioned. A lot of noise originates from insufficient shielding and microphonic noise on the cables. These long cables also increase the input capacitance of the amplification circuit. Hence, the increased capacitance will transfer the input voltage noise of the amplifier into an effective input referred current noise. An easy way to circumvent these problems is therefore to place the amplifier as close as possible to the source of the current, that is onto the glass cell. The approaches investigated in this regard are presented in chapter 6.

### 3.4.3 Open issues

There are still some open issues especially regarding the low detection efficiency. There is certainly a much smaller collisional cross section leading to ionization than the cross section responsible for the line broadening in general. One way to investigate the real fraction of ionizing collisions to $n$- and $l$-changing and elastic collisions in the Rydberg state is to monitor the fluorescence. Unfortunately, collecting the fluorescence is extremely inefficient and the resulting spectra are hardly interpretable. This is getting even worse, when comparing Rydberg states with different principal quantum numbers. In addition, the changing Rabi frequencies and additional scattering of laser light at condensed Rb will make such measurements challenging.
Another way could be to apply selective field ionization. In this manner the fraction of $n$- and $l$-changing collisions can be separated from ionizing collisions. By applying electric field pulses sufficient to ionize all Rydberg atoms one could

also get an estimate of the overall Rydberg population.
Although the detection efficiency is three orders of magnitude worse than in the experiment on NO, this experiment provides a good estimate of the possible sensitivity and the detection limit. The necessary improvements, namely the excitation efficiency and decreasing the noise became apparent. The broadening of the Rydberg line was used a lot for the estimation of the efficiency. The behavior of the linewidth and also its position will be discussed extensively in the next chapter 4.

# 4 A gas sensor in through-flow

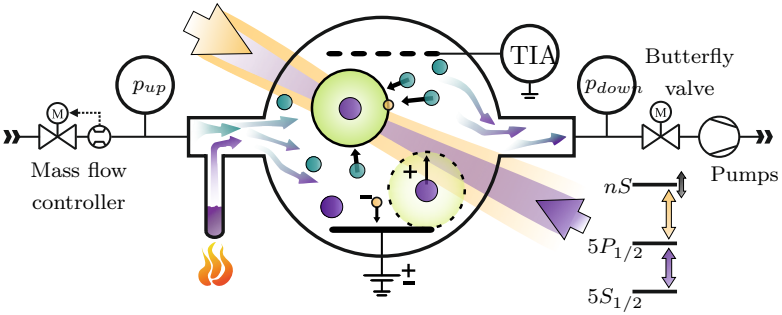


**Figure 4.1:** Schematic of the through-flow setup. Rb is mixed with $N_2$ and excited to a Rydberg state similar to the experiment presented in chapter 3. The emerging charges are measured with a TIA. The $N_2$ flow is controlled with a mass flow controller and the pressure is regulated downstream with a butterfly valve. This valve artificially throttles the pumping speed of the vacuum pumps. The pressure can be measured up- and downstream ($p_{up}$, $p_{down}$).

In this chapter the collisional processes are investigated in more detail. Therefore the line shape of the Rydberg line and its dependence on external factors are examined. The linewidth has already been used extensively in chapter 1 in order to estimate the application potential of a gas sensor based on Rydberg excitations. In chapter 3 the linewidth was necessary for estimating the achieved excited state fraction and hence the efficiency of the proposed gas sensing scheme. The progression of the gas sensing experiments in chapter 2 and chapter 3 is a gas sensor operated in through flow. This is the next step demonstrating the applicability of the scheme for a real-life operation, for example when someones breath is analyzed in real-time.
A difficulty arising from a through-flow experiment is the pressure drop across the vacuum tubings and the cell. For the glass cell shown in figure 3.1 the

pressure can only be measured before and after the glass manifold. Those two pressure values show a significant pressure drop when a background gas flow is maintained. Consequently, the pressure at the position of the excitation region is not known exactly and hence the background gas density cannot be determined. In order to estimate the pressure at the position of the Rydberg excitation one can make use of the linewidth of the Rydberg line, which depends strongly on the background gas density. This opens up the possibility of employing Rydberg excitations as a pressure gauge or even as a transfer standard for the calibration of pressure gauges. This outlook is discussed at the end of this chapter.
But, before this, the various broadening mechanisms are explained in a qualitative way with special attention on collisional broadening. Afterwards the measured lineshape is discussed and the results are applied on determining the pressure inside the through-flow sensor. A short comment on the results of a trace gas sensor in a through-flow configuration is given afterwards.

## 4.1 Broadening mechanisms

The absorption of excitation light as well as the current $I$ generated from exciting Rydberg states has the generic form of a Lorentzian function [4]:

$$I(\Delta\omega_C) = \frac{\Gamma/2\pi}{(\Delta\omega_C + \delta)^2 + (\Gamma/2)^2}. \tag{4.1}$$

This is the current as function of the detuning $\Delta\omega_C$ of the coupling light $\omega_C$ from a Rydberg transition. The Rydberg line might be shifted by $\delta$ and has a full width at half maximum (FWHM) of $\Gamma$.
There are several possible mechanisms leading to a broadening of the Rydberg line. Some of these are caused by the thermal motion of the atoms, such as residual Doppler broadening and transit-time broadening. Furthermore, power broadening contributes to the width of the Rydberg line caused by the spectroscopic methodology. Other contributions are external perturbations, such as black-body radiation or electric fields, which also leads to a shift of the Rydberg line. Since these broadening mechanisms are either inevitable for a thermal atoms experiment or lead only to a minor linewidth broadening, they are shortly introduced at first. Afterwards, the main contribution to the linewidth broadening, the collisional induced broadening is investigated in more detail in

section 4.2. This mechanism can also be responsible for a shift of the Rydberg line and is the main contribution to the generation of charges in the present alkali experiment.

**Residual Doppler broadening** The effects emerging solely from the motion of the atoms with respect to the excitation lasers were already discussed in section 3.1.2 and section 3.3.2. The transition $5S_{1/2}, F = 3 \rightarrow 5P_{1/2}, F = 2$ has a natural linewidth of $\Gamma_{nat} = 5.75\ 2\pi \cdot \mathrm{MHz}$. Atoms moving towards the $\omega_P$ excitation light with a velocity $v_{max} = \frac{\Gamma_{nat}/2}{k_{\omega_P}}$ are still in resonance with $\omega_P$ due to the Doppler effect. But these atoms move away from the $\omega_C$ light driving the transition $5P_{1/2}, F = 2 \rightarrow nS$ and appear therefore detuned by $\Delta = -v_{max} \cdot k_{\omega_C}$. The width of the Rydberg line is hence at least $2 \cdot |\Delta| = \Gamma_{nat} \cdot \frac{k_{\omega_C}}{k_{\omega_P}} \approx 9.6\ 2\pi \cdot \mathrm{MHz}$ broad. This is called the residual Doppler width.

**Transit-time broadening** Atoms moving out of the excitation volume have only a limited interaction time with the excitation light. This leads to the so called transit-time broadening. For a mean thermal velocity of $\bar{v} = \sqrt{8k_BT/(\pi m)}$ and a beam diameter $d$ this leads to a broadening of the line by [112]

$$\Gamma = \frac{4\bar{v}}{d} \cdot \sqrt{2 \cdot ln(2)}. \tag{4.2}$$

In the present setup, introduced in section 3.2.1 this broadening is only around $0.3\ 2\pi \cdot \mathrm{MHz}$ for the groundstate transition.

**Power broadening** If the excitation light $\omega_P$ has a sufficient intensity $I$, the laser will cause induced emission of the excited state with a rate faster than its average decay rate $\Gamma_{21}$. This leads to a power broadening. The dependency of the effective linewidth on the light intensity looks like this

$$\Gamma_{eff} = \sqrt{\Gamma_{21}^2 + 2\Omega_P^2} = \Gamma_{21}\sqrt{1 + I/I_{sat}}. \tag{4.3}$$

Here, the saturation intensity $I_{sat} = \pi hc\Gamma_{21}/(3\lambda^3)$ is introduced. With an increasing number of collisional events also the saturation intensity will increase and hence it is possible that, in the presence of power broadening, the linewidth of the Rydberg signal first decreases with increasing pressure. The power of

the probe light $\omega_P$ was therefore set such that the current amplitude reached a maximum without showing any visible power broadening. Compare here also section 3.2.1. This ensures that the linewidth will increase linearly with increasing collision events. This is discussed in section 4.2.

Apart from these main contributions to the linewidth there are other sources of broadening, which, however, do not contribute significantly to the experiments considered in this thesis.

**Inhomogeneous electric fields** In a thermal vapor a lot of charges can be generated by e.g. the Rydberg excitation or also by the photoeffect. At sufficiently large excitation intensities even plasmas can be generated [113]. Additionally, a fraction of the charges remains sticking to the glass walls. This leads to inhomogeneous charge distributions along the excitation paths. The dc-Stark induced shift along the excitation beams can cause an inhomogeneous broadening. This is extensively discussed in [20]. Furthermore, collisions of the Rydberg excited atoms with charges can cause broadening too. By spectroscopically investigating D-state Rydberg atoms, possible Stark effect induced effects, that would in the case of a D-state lead to a splitting of the line, were ruled out. These effects are hence minor on the scale of the linewidth of the Rydberg line. This is not so much surprising, since the total alkali atom density is kept low.

**Stark effect** In order to distinguish collisional induced shifts of the Rydberg line from shifts caused by electric fields, the Stark effect is briefly introduced. Since the valence electron of a Rydberg excited atom is far apart from the ionic core, an atom in a Rydberg state has a large polarizability $\alpha_0$. That means a dipole moment can be induced very easily by an electric field $\mathcal{E}$. The impact of an external electric potential $V(r) = \epsilon_0 \cdot r \cdot \mathcal{E}$ onto the eigenenergies $E_n$ can be calculated using perturbation theory:

$$E_n = E_n^{(0)} + \langle \psi_n | V | \psi_n \rangle + \sum_{p \neq n} \frac{|\langle \psi_n | V | \psi_p \rangle|^2}{E_n^{(0)} - E_p^{(0)}}. \tag{4.4}$$

High $l$ states are degenerate. This is due to the low probability density of finding the electron close to the ionic core. Hence the eigenenergies do not have to be corrected by the quantum defect. For these high $l$ states ($l > 3$),

only the linear Stark effect in first order (equation (4.4)) has to be taken into account [114]. For low $l$ states like the $nS$ states that are considered in this experiment, the quadratic Stark effect is dominant for low electric fields and shifts the eigenenergies accordingly:

$$\Delta E = -\frac{1}{2}\alpha_0 \cdot \mathcal{E}^2. \tag{4.5}$$

The polarizabilities $\alpha_0$ can be calculated for $^{85}$Rb according to [8] by

$$\alpha_0\ [\mathrm{MHz/(V/cm)^2}] = 2.202(28) \cdot 10^{-9} n^{*6} + 5.53(13) \cdot 10^{-11} n^{*7}. \tag{4.6}$$

**Collisions with electrons** A significant amount of charges detected in the present experiment are created by the photoeffect on bulk Rb sticking onto the walls of the glass cell (see section 3.3.2). According to [115], the electron induced broadening is given by $\Gamma = n_e \cdot v \cdot \sigma_e$. The density of electrons $n_e$ can be estimated from the photocurrent and the time the electrons need to pass the glass cell (see section 3.3.2, figure 3.4 b)). Using a current of $I_{photo} = 1$ nA, a distance $d = 1.0$ cm between the electrodes, a voltage of $U_{bias} = 2.6$ V and an excitation volume of $V = 7.9$ mm$^3$ one obtains an electron density of $n_e = 8.2 \cdot 10^9$ m$^{-3}$ moving with an electric field driven velocity of $v = 9.6 \cdot 10^5$ m/s through the excitation region. With a collisional cross section of $\sigma_e = 9.2 \cdot 10^{-15}$ m$^2$ [20] one receives a broadening of $\Gamma = 11.6\ 2\pi \cdot$ Hz, which is negligible.

**Other broadening mechanisms** Other possible broadening mechanisms such as blackbody radiation [116] or photoionization [117] do not contribute in an observable manner to the Rydberg line [20] in the present experimental realization. The same is true for Rydberg-Rydberg collisions [5] since the excited state fraction and the alkali atom density are so small.

## 4.2 Collisional broadening

In this section the broadening mechanisms induced by collisional processes will be discussed. A collision disrupts the phase of the atomic wavefunction. Hence, the frequency of the atomic transition will be less well defined and the transition will appear broadened [4]. There are in general three types of collisions contributing to the broadening of an atomic line. Inelastic collisions lead to a change of the state. These can be $n$- or $l$-changing collisions, but also ionizing collisions. Then there are elastic collisions with the valence electron, where the collisional event induces a phase shift on its wavefunction. The third process is a scattering of the perturber at the ionic core of the Rydberg atom. For most experiments this process contributes the least to the linewidth and is difficult to separate from other broadening effects [118]. The last two processes additionally lead to a shift of the eigenenergies of the wavefunction. This will be explained in section 4.2.2.
The present spectroscopic accuracy allows only the observation of two-body collisions. Hence for any type of collisional process the broadening $\Gamma$ is given by [4]

$$\Gamma = n_B \cdot \bar{v} \cdot \sigma. \tag{4.7}$$

The mean relative velocity $\bar{v}$ between the two collisional partners is given by $\bar{v} = \sqrt{\frac{8k_B \cdot T}{\pi\mu}}$, where $\mu$ is the reduced mass $\mu = \frac{m_A m_B}{m_A + m_B}$ and $\sigma$ is the collisional cross section for the considered collisional process.
The temperature dependence of $\Gamma$ is often included in a semi-empirical manner referenced to a temperature $T_0$ at which $\Gamma_0$ was determined [119]:

$$\Gamma(T) = \Gamma_0 \left(\frac{T}{T_0}\right)^{\kappa}. \tag{4.8}$$

The temperature scaling coefficient $\kappa$ depends on the exact form of the interaction potential, which is mostly modeled as $V(R) = \sum_p C_p/R^p$. Here $R$ is the distance of the collisional partners and $C_p$ are the interaction coefficients. Often $\kappa$ is given by $\kappa \approx (p-3)/(2p-2)$. In case of a van der Waals type potential $\kappa$ is given by $\kappa_{p=6} \approx 0.3$. For most of the analysis presented so far it was assumed that $\sigma$ is temperature independent and one can hence set $\kappa = 1/2$ as a result of the relative mean velocity dependence of $\Gamma$.
In general this approach of modeling the temperature dependence is only valid

for rare gas perturbers. It can as well be applied for collisions of Rb groundstate atoms with rare gas like molecules such as $N_2$ or $CH_4$ [119]. It is in fact not valid for collisions between Rydberg atoms and perturbers, where the thermal distribution of the internal degrees of freedom coupling to the Rydberg lines can vary in a very nonlinear manner [106, 120, 121], as it is the case for molecules. This will be discussed in-depth in section 4.2.2.

### 4.2.1 Groundstate scattering

The broadening of the groundstate can be attributed to different processes. Apart from collisional broadening $\Gamma_{collision}$ there are in general three contributions to the width of the groundstate transition in Rb:

$$\Gamma = \Gamma_{nat} + \Gamma_{dipole} + \Gamma_{collision}. \tag{4.9}$$

The natural linewidth $\Gamma_{nat}$ is in our case 5.75 $2\pi \cdot$ MHz [100]. Resonant dipole-dipole interactions between two Rb atoms cause an additional broadening $\Gamma_{dipole}$:

$$\Gamma_{dipole} = n_{Rb} \cdot \beta. \tag{4.10}$$

The self-broadening coefficient $\beta$ for the $D_1$ line is given by $\beta = (0.69 \pm 0.04) \cdot 10^{-7}$ $2\pi \cdot$Hz cm$^3$ [122]. In our experiments the Rb density is typically very low such that one can neglect this type of broadening.
Nevertheless, the collisional broadening $\Gamma_{collision}$ can be significant. For a $N_2$ background gas the broadening can be calculated using equation (4.8). In [123] $\Gamma_0$ was determined to $\Gamma_0 = (12.2 \pm 0.3)$ $2\pi \cdot$ MHz/mbar at a temperature of $T_0 = 394$ K. In the absence of a temperature scaling coefficient one can set $\kappa = 0.3$ [119].
This was also verified in the Master thesis of Ralf Albrecht [104]. At an $N_2$ pressure of e.g. 10 mbar a linewidth of $(116.5 \pm 0.8)$ $2\pi \cdot$ MHz was observed on the $D_2$ line, which is on the same order of magnitude as 142.2 $2\pi \cdot$ MHz as predicted in [123].
This broadening includes population losses as well as dephasing mechanisms. Since the gas detection scheme is mainly limited by collisional deexcitation processes we started investigating the pressure dependent lifetime and spin-flipping collisions. This was the topic of the Master thesis of Ralf Albrecht [104].

**Collisional decay** A pulsed pump-probe scheme was set up. A short pulse pumped atoms from the $5S_{1/2}$ state to the $5P_{3/2}$ state of $^{87}$Rb. The population in the excited state was probed by a variable delay after the pump pulse. The result of this experiment is that the lifetime of the excited state does not change in the boundaries of the experimental uncertainties. For three different cells filled with $N_2$ as a background gas at a pressure of 0.5, 5.0 and 10.0 mbar the lifetime was determined to (5.05±3.32), (6.67±3.99) and (6.44±3.73) $2\pi\cdot$MHz. This is in essence the natural lifetime $\Gamma_{nat} = 6.065\ 2\pi \cdot \text{MHz}$ [100].

**Spin-flipping collisions** The collisional decay does not only consist of state transfers from the $5P_{3/2}$ to the $5S_{1/2}$ state, but also spin-flipping collisions. They can decrease the population in the excited state. For instance atoms excited to the e.g. $5P_{1/2}$ state are excited to the $5P_{3/2}$ state via collisions and vice versa. By monitoring the fluorescence emitted vertically to a pumping beam the relative populations in the $5P_{3/2}$ and the $5P_{1/2}$ were measured. This was done for pumping either the $5P_{3/2}$ or the $5P_{1/2}$ state. The collisional cross sections for the decay of the $5P_{1/2}$ state in $^{87}$Rb by the collision with $N_2$ molecules were determined to $\sigma_{5P_{3/2}\rightarrow 5P_{1/2}} = (1.8 \pm 1.0) \cdot 10^{-19}\ \text{m}^2$ and $\sigma_{5P_{3/2}\rightarrow 5S_{1/2}} = (16.6 \pm 12.0) \cdot 10^{-19}\ \text{m}^2$. This is in good agreement with [124]. The spin-flipping rate of the groundstate transition for the pressure range investigated for the gas sensing scheme in chapter 3 and in this chapter is at most $0.2\ 2\pi \cdot \text{MHz}$.

The overall decay of the groundstate transition is therefore always only on the order of the natural lifetime. In the following the pressure induced population losses of the intermediate state will be neglected.

### 4.2.2 Rydberg scattering

Collisions with Rydberg atoms are interesting to investigate because the Rydberg electron is more or less independent from the ionic core and can be treated as slowly moving through the background gas of perturbers. Although one might expect that the collisional cross sections are extremely large due to the large size of the Rydberg orbit and the low binding energy, in fact Rydberg

excited atoms appear rather dilute and show cross sections which are comparable to groundstate atoms [4]. As mentioned in the beginning of this section, collisions can be separated into three categories.

**Fermi shift** Elastic collisions between the Rydberg electron and a perturber lead to a phase shift, which is called the Fermi shift. This pressure induced shift has been observed first by Amaldi and Segrè [125, 126] and was explained by Fermi [127]. It has been investigated extensively in the last years and a vast amount of literature is available on this topic [4, 128–130]. The shift can be described by introducing the so called Fermi-Pseudo potential $V = 2\pi \cdot \frac{\hbar^2}{m_e} \cdot a \cdot a_0 \cdot |\psi(r)|^2$. Here $a$ denotes the scattering length normalized by the Bohr radius $a_0$. This energy shift will in first order lead to an $n$-independent line shift increasing with the density $n_B$ of perturbers

$$\delta = 2\pi \cdot \frac{\hbar}{m_e} \cdot a \cdot a_0 \cdot n_B. \tag{4.11}$$

By assuming the scattering cross section to be $\sigma_{elastic} = 4\pi \cdot a^2 \cdot a_0^2$ [131] and using the velocity of the Rydberg electron $v = \frac{2 \cdot R_y}{\hbar} \cdot a_0 \cdot \frac{1}{n^*}$, one obtains the elastic contribution to the width by inserting this into equation (4.7)

$$\Gamma = 8\pi \cdot a_0^3 \cdot \frac{R_y}{\hbar} \cdot a^2 \cdot \frac{1}{n^*} \cdot n_B. \tag{4.12}$$

This is only valid for Rydberg states exceeding $n^* = 30$. For the states investigated here, instead of the Rydberg-$e^-$ velocity the mean thermal velocity of the two colliding partners is used, in accordance to [132]:

$$\Gamma = 4\pi \cdot a^2 \cdot a_0^2 \cdot \bar{v} \cdot n_B. \tag{4.13}$$

The interaction between the Rydberg electron and the pertuber can either be attractive or repulsive. That means that the shift can either be towards lower or higher energies depending on the type of perturber [128]. Generally this interaction is only short-range [4].

**Collisions with the ionic core** The elastic collisions between the perturbing atom and the Rydberg ionic core lead to a broadening as well. This broadening and shift is mostly only observable for high energy collisions or very high $n$ states. For most collision experiments with varying background gas this sets the lower limit of the magnitude of the collisional cross section.

**$n$- and $l$-changing collisions** Inelastic scattering events lead to $n$- and $l$-changing collisions, similarly to the results presented in section 4.2.1. Speaking in a physical picture, the perturbing atom collides with the Rydberg electron. This scattering event leads to a reorientation of the electron and hence a change in $l$. Additionally, it can also lead to a change of the principal quantum number $n$ [4, 120]. The excess energy is either transferred from or into the translational energy of the colliding perturber. This immediately shows that this kind of collision is also a short-range interaction. For higher $n$ states the wavefunction becomes more dilute and consequently the collisional cross section decreases. If the perturbing scatterers are molecules this cross section can be significantly larger than it is in the case of rare gas atoms. Regarding molecules the excess energy can additionally be absorbed or released from the internal degrees of freedom, that is the rotational and vibrational transitions [106].

**Collisions with rare gases** Collisions with rare gases result to 90% in a Fermi shift and hence broadening as well. The remaining portion is attributed to the polarization broadening. Collisions between alkali Rydberg atoms and rare gases can also lead to $n$- and $l$-changing collisions. Yet, this contribution is only small compared to the elastic broadening effects, because all energy has to go or come from the translational energy of the rare gas atom. Still, for Rb where the $(n-3)F, G, ...$ levels are energetically close to the $nS$ levels, the broadening due to inelastic collisions is significant [133]. In [132] the broadening and shifts of the Rb Rydberg lines from collisions with rare gases have been measured. They found perfect agreement with the theory taking into account all three broadening contributions. For example for Ar they measured a total collisional cross sections of $\sigma = (4.7 - 5.3) \cdot 10^{-18}$ m$^2$ for the $nS$ states from $n = 20 - 30$ and a shift to the red.

**Collisions with molecules** For molecules the situation changes. Here also long-range interactions due to electron-dipole or electron-quadrupole interactions are possible [4]. This is more dominant for polar molecules such as CO [120] compared to nonpolar molecules such as $N_2$ [106]. In the case of $N_2$ the electric dipole has to be induced by the Rydberg electron first, meaning that the $N_2$ has to be closer to the Rydberg atom in order to access these higher order moments. This interaction will always lead to a red shift.
The $n$- and $l$-changing collisions form the lower limit of the cross section for

high $n$. The exact cross section is mainly given by the internal population distribution of the rotational and vibrational levels and is hence temperature dependent. For fast rotating molecules the collisional cross sections can vary a lot [134]. That is the reason why a simple scaling of the temperature, as it is the case in equation (4.8), is not applicable for molecules. Although for example $N_2$ behaves a lot like a rare gas atom in the sense that the $n$- and $l$-changing collisions show a similar $n$-dependent behavior. This means that the coupling to the internal degrees of freedom as well as electron-quadrupole interaction play only a minor role for high Rydberg states. Unfortunately I found only publications investigating solely the depopulation mechanism, that is $n$- and $l$-changing collisions for the Rb-$N_2$ mixture. The collisional cross section for these processes according to [106] is between $\sigma = (1-3) \cdot 10^{-18}$ m$^2$ for the $nS$ Rydberg states with $n = 24...34$ and the shift is reported to be towards the blue [128].

**Self broadening** Collisions of Rydberg atoms with alkali metals show a very different structure compared to collisions with rare gases [4, 108, 135]. Although the broadening rises for small $n$ and declines to a plateau for large $n$, in between the broadening rate shows an oscillatory behavior with $n$, due to resonances in the electron-alkali metal scattering length. The self broadening rate was measured in [108] to be $2.2\ 2\pi \cdot \frac{\text{MHz}}{\text{mTorr}}$ at a temperature of 200 °C. Assuming a van der Waals interaction ($\kappa = 0.3$) this yields, according to equation (4.8) and the properties of the experiment written in table 3.1, a broadening of at most $11.8\ 2\pi \cdot \text{kHz}$. This is not resolvable in the present experiment.

**Remark on ionizing collisions** Most of the literature points out [106, 136, 137], that the cross section leading solely to ionization of the Rydberg excited alkali atom is two orders of magnitude less than the total collisional cross section. This is also the main explanation for the low efficiency obtained in chapter 3, when taking the full Lorentzian width of the Rydberg line into account.

## 4.3 Experimental setup

The setup used for this experiment is the same as introduced in section 3.2. The difference to the gas sensing experiment presented in section 3.3 is that the experiment is now operated in flow rather than in a static manner. The experimental setup is depicted in figure 4.1. The amount of background gas entering the experiment is again set by a massflow controller. The pressure inside the cell is regulated using a butterfly valve downstream on the side of the vacuum pump. By decreasing the tube diameter with the valve the effective pumping speed can be throttled. The pressure before and after the experiment can be determined with two vacuum gauges. These will be called the up- and downstream gauge from now on.

### 4.3.1 Flow characteristics

Any tube has a certain flow resistivity and induces a pressure drop along its length. For this reason a different pressure can be measured at the up- and downstream gauges for a certain massflow. The pressure range achievable for a completely opened and a fully closed valve is depicted as colored area in figure 4.3 for the two pressure gauges. Here, the important aspect is that the actual pressure at the position of the excitation region is not known exactly as will be explained in the following.

In figure 4.3 a) the pressure in a prototype cell is shown. There the thickness of the cell was only 5 mm and hence the diameters of the tubes attached to it were only on the order of 2-3 mm. The difference in pressure measured up- and downstream is significant. Assuming that the largest pressure drop occurs at the outlet of the glass cell, we can also assume that the pressure measured upstream is also present inside the cell. Hence, a pressure range of only 0.1 -1 mbar can be covered. The minimum background pressure is already too large to controllably set the Rb density without excessive heating (compare also the remarks in section 3.2.3). The employed cell has a diameter of 10 mm instead and hence the pressure drop along the whole glass manifold is a lot less as can be seen in figure 4.3 b).

As already mentioned, the real pressure at the point of the cell is not known, unless one fills the cell in a quasi static manner as was done in chapter 3. For the considered dynamic flow condition exist semi-empirical equations for

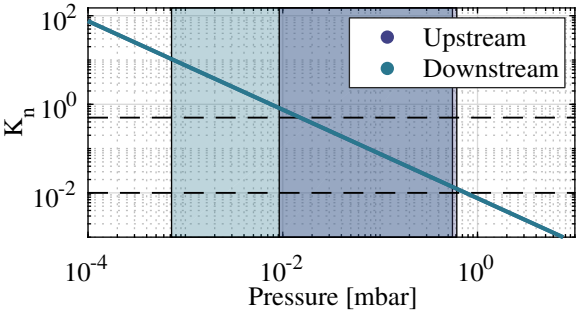


**Figure 4.2:** Knudsen number $K_n$ as function of the pressure inside the excitation region. The nearest cell wall distance is 10 mm and the temperature is for most experiments about 350 K. The colored patches indicate the achievable pressure range as plotted in figure 4.3. The dashed lines indicate the borders of the flow regimes.

estimating the pressure after a certain flow constriction. Nevertheless, the type of flow has to be known and is for the known equations either a purely viscose flow or a purely molecular flow [138]. The flow regime can be estimated by using the Knudsen number

$$K_n = \frac{k_B \cdot T}{\sqrt{2} \cdot \pi \cdot p \cdot \sigma^2 \cdot d}. \tag{4.14}$$

In this equation the pressure $p$, the geometric hard-shell diameter $\sigma$ of the background gas and the smallest distance $d$ of the walls of the apparatus have to be known. For the diameter of $N_2$ a value of $\sigma = 379.3 \cdot 10^{-12}$ m is used [138]. For $K_n < 0.01$ the main collision partners of a gas molecule are other gas molecules and therefore a viscose flow is present. For $K_n > 0.5$ the main collision partners are the walls of the vacuum apparatus and hence molecular flow is given. The regime in between is called Knudsen flow and is a mixture of both regimes. The Knudsen number $K_n$ for the present experiment is depicted in figure 4.2. The dashed lines indicate the onset of the different flow regimes. The colored patches mark the achievable pressure range measured up- and downstream. Apparently the present experiment is mostly in the regime of Knudsen flow where e.g a pressure drop along a tube can not be calculated, apart from the difficulty of reliably estimating the diameters and lengths of the glass manifold, see also the picture in figure 3.1.

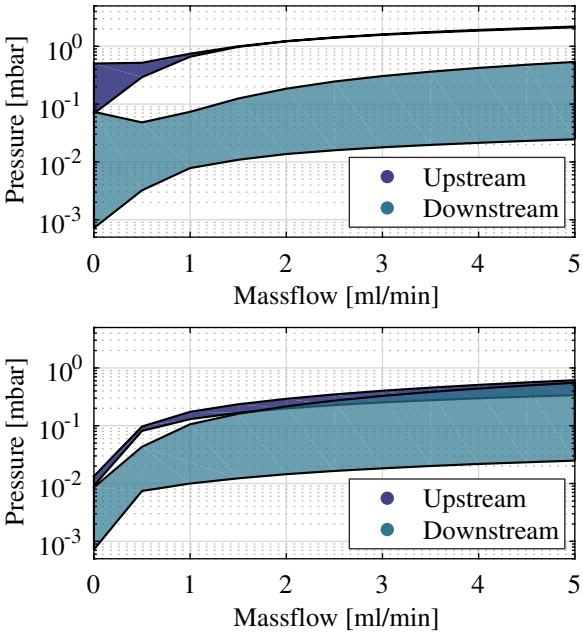


**Figure 4.3:** The pressure range, which is achievable with the butterfly valve and the employed vacuum pump as function of the massflow. The pressure is measured up- and downstream of the glass cell. a) Old cell, which had only a thickness of 5 mm. b) New cell with a thickness of 10 mm.

## 4.4 Experiment and results

In the following the attempts to measure the background gas pressure inside the excitation region are explained. Afterwards the difficulty of calibrating a gas sensor operated in through-flow using a groundstate spectroscopy is described. The measurement is always performed like this: First, the background gas density is increased slowly in a quasi static manner just as described in section 3.2.3 without pumping. While doing so Rydberg spectra are continuously recorded. As soon as no signal is visible anymore, the experiment is pumped empty. Then, while pumping, a certain massflow is set and the position of the butterfly valve is varied. Between each setting the system is allowed to

settle for at least one minute to equalize at a certain background gas flow and Rb density. This is sufficient to establish an equilibrium between the rate at which the Rb is diffusing out of the reservoir and the rate at which the alkali metal is condensing onto the glass walls, which largely depends on the overall background gas density.

### 4.4.1 Rydberg broadening and shift

The impact of the background gas density on the line shape is investigated first. For this purpose the background gas density is increased in a quasi static manner and the evolution of the lineshape is plotted in figure 4.4 for $N_2$ and in figure 4.5 for Ar for a variety of $nS$ Rydberg states. Apparently the linewidth increases linearly with the background gas density in agreement with equation (4.7). It starts from an offset given by the residual Doppler width and presumably charges present inside the cell. One can also observe fluctuations in the offset of the broadening. These fluctuations of the offset are used in chapter 1 for the estimation of the accuracy of the proposed gas sensing scheme. Also the slope itself shows fluctuations, which are uncorrelated from the principal quantum number $n$. Since both fluctuations may also be caused by a changing Rabi frequency $\Omega_P$ of the probe transition $\omega_P$, a single correlation between broadening and accumulating charges due to a coating of the walls with Rb can neither be confirmed nor ruled out.
Following equation (4.7) the cross section $\sigma_{total}$ can be determined from the slope of the width of the Rydberg line for each Rydberg state $nS$. The resulting cross section is plotted in figure 4.6 as function of the principal quantum number for both perturber gases. The values of the cross section show a large statistical spread. This is connected to the already mentioned fluctuations. Moreover, the linear fit to the data from which the collisional cross section is extracted introduces another error source.
Apparently the $1/n^*$ behavior predicted for a Fermi shift in equation (4.12) is not observable. This is very likely due to the already small principal quantum number.

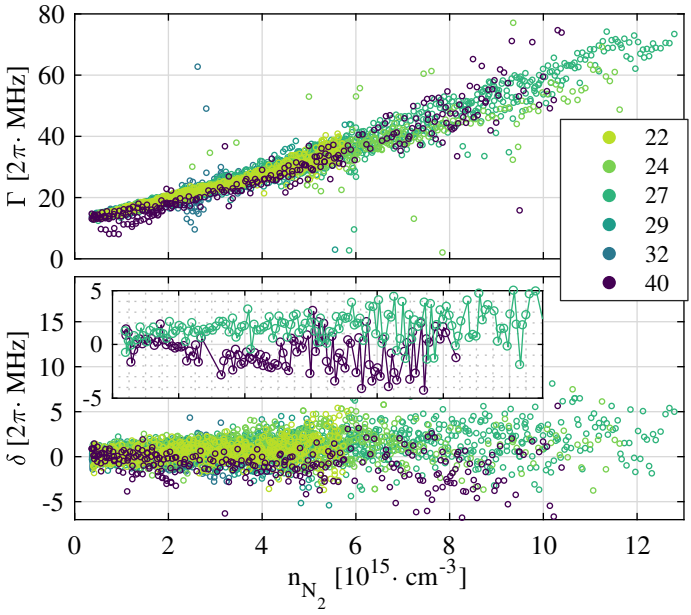


**Figure 4.4:** a) Width of the Rydberg line for different Rydberg states as function of the $N_2$ background gas density. b) Shift of the Rydberg line. The mean value of the first five data points was subtracted from the measurements. The inset shows two exemplary traces. They serve to exemplify the difficult reproducibility of the experiment due to Stark induced shifts.

**Collisions with $N_2$** The collisional cross section for the scattering at $N_2$ is about one order of magnitude larger than the results presented in [106]. Two reasons are responsible for this discrepancy:
First, the experiment here is performed at a temperature of 100 °C more than in [106]. This leads to a different population distribution of the rotational levels of $N_2$ and hence a different $n$- and $l$-changing cross section. The second reason is that in [106] only inelastic processes leading to a depopulation of the Rydberg state were investigated. An $n$-independent offset of the cross section caused by the scattering of $N_2$ at the ionic core of the Rydberg atom or an electron-quadrupole interaction was not taken into account. Unfortunately I found no suitable literature values quantifying the impact of elastic collisions

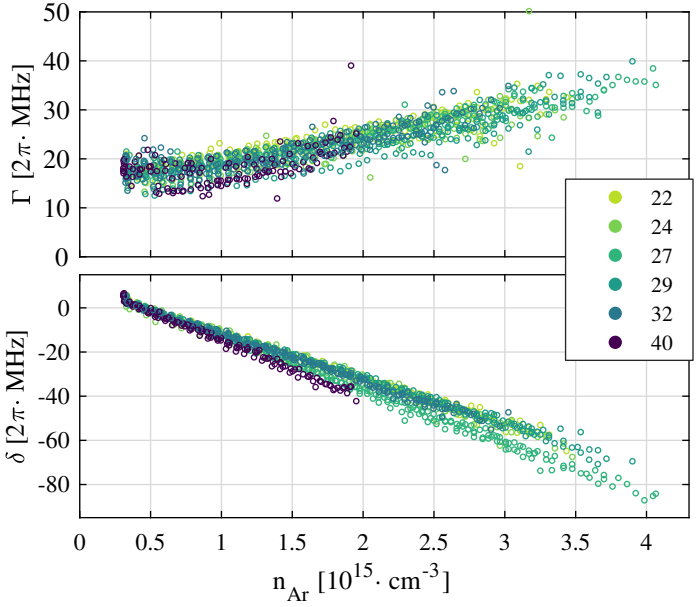


**Figure 4.5:** a) Width of the Rydberg line for different Rydberg states as function of the Ar background gas density. b) Shift of the Rydberg line. The mean value of the first five data points was subtracted from the measurements.

of $N_2$ with Rb on the width of the Rydberg line.
In any case, the best way to quantify the contribution of elastic collisions onto the Rydberg line is to investigate the shift of the Rydberg line. However, the shift plotted in figure 4.4 for the case of $N_2$ shows no clear behavior. There are reports about shift measurements of the Rydberg line at higher temperatures. This can only be due to elastic scattering [4, 126]. A blue shift was also measured by [128] for a Cs-$N_2$ mixture, which turned to red for high pressures. They also measured a red shift for a K-$N_2$ mixture. But in figure 4.4 are also measurements visible going to smaller energies uncorrelated from the principal quantum number. Some shift measurements even show an oscillatory behavior. This is attributed to charges inside the glass cell.
In between the measurements the glass cell was exposed to excessive heating. Moreover, the measurements for the $40S$ state were done in a freshly cleaned

and refilled glass cell. That means, the surface coating changed completely. A possibility to obtain more significant measurements is to increase the background gas pressure even further. The Rb density is strongly linked to the $N_2$ density as was already discussed in section 3.3.3. Consequently more Rb should be heated outside the reservoir, which in turn leads to a faster coating of the cell walls. An increase of the oven temperature was avoided in order to not destroy the electrical contacts and the cell itself. The fundamental physical explanation for the difficulty of determining the elastic cross section of collisions of $N_2$ with Rb Rydberg atoms is that $N_2$ interacts only little via elastic collisions with Rb Rydberg atoms. This was already reported in one of the first publications on the Fermi shift [126], where the direction of the shift could not be identified as well. It could even be possible, that the quadrupole interaction between $N_2$ and the Rydberg atoms cancels a presumably present blue shift caused by elastic $e^-$-$N_2$ scattering.

**Collisions with Ar** The situation changes completely, when investigating collisions of Ar with Rb Rydberg atoms. Here a significant shift is observable on the same order of magnitude as was already reported in [132]. By determining the slope of the shift and using equation (4.11), this opens the possibility to extract the contribution of elastic collisions $\sigma_{elastic}$ to the total cross section $\sigma_{total}$. The determined cross section $\sigma_{elastic}$ is depicted in figure 4.6 b). Since the amount of inelastic collisions, which include $n$- and $l$-changing collisions as well as ionizing collisions, is smaller than $\sigma_{total}$ the lower efficiency estimate for the gas sensor principle introduced in chapter 3 (section 3.4.1) can be improved.

### 4.4.2 Determination of the pressure inside the excitation volume

In order to determine the background gas pressure at the position of the Rydberg atoms, the width of a Rydberg signal measured in flow is compared with the width of a Rydberg signal measured in a quasi static manner.
With the intention to become more immune against fluctuations, a first order polynomial is fitted to the width as function of the background gas density, which is shown in figure 4.4. These fluctuations mostly arise from the uncertainties in the Lorentz function fitted to the Rydberg signal.

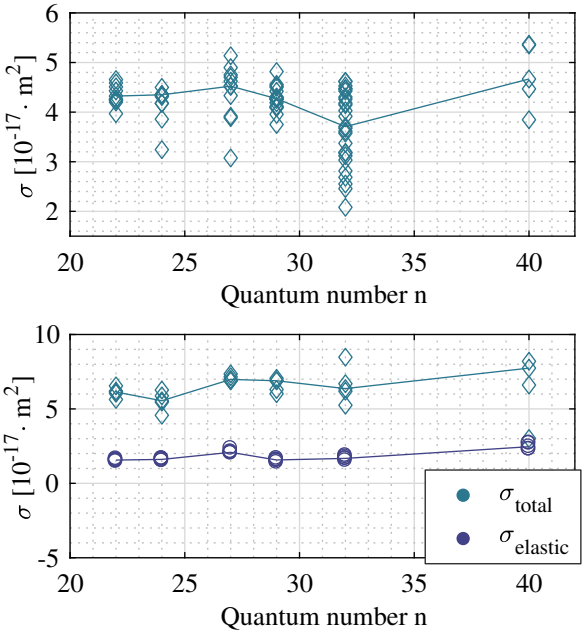


**Figure 4.6:** Cross section obtained from the slope of a linear fit to the width of the Rydberg line shown in figure 4.4 and in figure 4.5. The straight lines connect the median value of the measurements for each principal quantum number as guide to the eye. a) Cross section $\sigma_{total}$ for the Rb-$N_2$ mixture. b) Cross section $\sigma_{total}$ and $\sigma_{elastic}$ for collisions between Rb Rydberg states and Ar atoms. $\sigma_{elastic}$ is obtained from the slope of a linear fit to the shift of the Rydberg line.

This fit is subsequently used for looking up the $N_2$ density that is causing a certain broadening of the Rydberg line in a through-flow configuration of the experiment. The width as function of the background gas pressure determined in a static measurement hence serves as a look-up table to determine the pressure corresponding to a width measured during a through-flow experiment.
The background gas pressure determined in this way is plotted as stars in figure 4.7 as function of the $N_2$ massflow. The pressure values are between the pressure values measured with the up- and downstream gauges, which is what one would expect. Unfortunately, there are a lot of fluctuations. For example

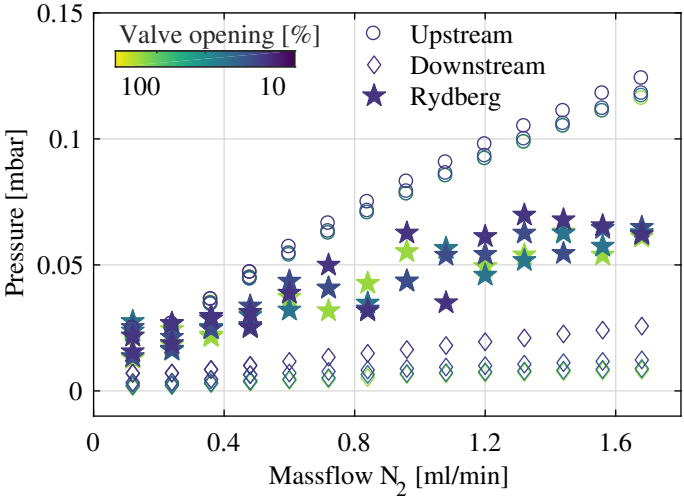


**Figure 4.7:** Pressure as function of the massflow for different valve openings. The measured pressure at the up- and downstream gauges is marked in open circles and diamonds respectively. The pressure determined from a comparison of the measured Rydberg linewidth with the linewidth measured in a static experiment (compare figure 4.4 a)) is marked with filled stars.

some pressure values determined for an opened valve are larger than for a closed valve. This is again attributed to uncertainties in the fitting of the Rydberg line combined with the overall fluctuations in the experiment as was already discussed in section 4.2.2.

### 4.4.3 A gas sensor for rubidium in through-flow

By using the determined background gas pressure one could in principle look up the Rb density from e.g. figure 3.5, which is supposedly present inside the cell. But the resulting graph of the current as function of the Rb density does not resemble to plots like figure 3.6. This is again caused by the need of Rb to diffuse through the $N_2$ background gas density and hence the Rb density is correlated to the $N_2$ density. This was already discussed in section 3.2.3. There it was shown that different filling speeds with $N_2$ resulted in different amounts

of Rb inside the cell. An independent characterization of the gas sensing scheme in through-flow by correlating it to a static determination of the Rb density as function of the background gas density is therefore not possible. Moreover, measuring the Rb density with groundstate spectroscopy already in flow is not feasible due to the low optical density.

## 4.5 Conclusion

Characterizing the gas sensing scheme in flow rather than in a static manner turns out to be unfeasible. The main problem is the correlation between the Rb and the $N_2$ density. This problem is a result of the fact that Rb needs to be evaporated in order to go to the gas phase. Nevertheless, Rydberg states can still be used as a pressure sensor for determining the background gas pressure.

### 4.5.1 A pressure sensor based on Rydberg excitations

The standard for high pressures in the range between $10^3$ mbar and a few $10^5$ mbar are mostly piston gauges [139]. For low vacuum conditions ($10^{-3}$...1.1 mbar) manometers are used. For even lower pressures the definition of pressure as force per area is not suitable anymore. The pressure is then a measure of the particle density and is defined in first order via the ideal gas law

$$p = \frac{N}{V} \cdot k_B \cdot T. \tag{4.15}$$

Apparently, pressure metrology becomes a counting problem [139].
Nevertheless, the standard for ultra high vacuum is still given indirectly through the conventional pressure definition [140]. One standardized method to create an ultra high vacuum with a well-defined pressure is the following: A gas at a determined high pressure is expanded into a larger volume, such that the resulting pressure is defined through the ratio of the volumes and the initial pressure. In this way also the vacuum in chapter 2 was prepared. The other possibility is to maintain a well defined flow through an apparatus with a precisely characterized orifice in between two volumes. The pressure drop between

the two volumes can be calculated if the conductance $C$ of the orifice is known sufficiently well

$$p_{up} - p_{down} = \dot{N} \cdot \frac{k_B \cdot T}{C}. \tag{4.16}$$

Both methods are a standard in vacuum metrology. They both suffer from the disadvantage that the apparatus itself has to be designed very carefully. Furthermore, both methods are restricted to so called non-sticky gases. The employed calibration gases are therefore limited to rare gases, nitrogen and methane. Additionally the methods also suffer from outgassing of residuals from the walls of the apparatus.
Therefore a significant effort was made to invent a new primary standard. That means a standard that needs no calibration and is solely based on SI units [141]. Optical methods such as the already explained REMPI (section 2.3.1), cavity ring down spectroscopy, optical refractometry [142] for high pressures or rovibrational and groundstate spectroscopy [143, 144] all rely on the precise knowledge of the absorption coefficient and the refractive index of the medium. Hence, most of the methods make use of ab initio calculations of the response of the system on He. The response of all other gases is then acquired through ratiometric measurements in comparison to He. Another approach is to make use of a magneto-optical trap (MOT) [139, 145–148]. The trap's lifetime is a function of the background gas density. Through a precise theoretical determination of the collisional cross section of He for example with the trapped atoms, one can deduce the background gas density by measuring the trap lifetime. Again, ratiometric measurements enable the expansion of this method to other background gases apart from He. For this reason it is called a functionally primary standard, since it does not need calibration but it is still based on a one-time measurement of a physical quantity, which is not part of the SI units.
Most of the aforementioned problems would also apply to a pressure sensor based on Rydberg excitations. That is, the collisional cross section of the background gas atoms with the Rydberg atom has to be known. Compared to already standardized methods a pressure sensor based on Rydberg excitations shows several promising advantages.
First, the interaction of alkali Rydberg states with the non-sticking gases is sufficiently well known and thoroughly understood. Even more, the collisional cross section with the slow Rydberg electron can be determined from ab initio calculations. For all rare gases the interaction with Rydberg atoms has already been measured and the theoretical models reproduce the data very well. How-

ever, the interaction with $N_2$ and $CH_4$ has not been investigated in every detail yet. Nevertheless, the big advantage is that the cross section can be tailored by choosing a certain quantum state. In this way one can choose whether the interaction of the Rydberg electron and the background gas should dominate the line broadening, or whether collisions with the ionic core or $n$- and $l$-changing collisions influence the lineshape most. Furthermore, a measurement of the position of the Rydberg line can give decisive evidence on the type of collisional process and hence the type of perturbing background gas.
Second, the dilute alkali vapor itself does not impose a constriction on the flow. Hence, such a pressure sensor is applicable for dynamic measurements inside a flow of background gas. Although there are in fact already investigations on optical rotational spectroscopy of e.g. $CO_2$ [143, 144] with very high repetition rates, these experiments are so far limited to a pressure regime of several 100 mbar. Additionally, there is so far no standardized way to measure dynamic pressure changes.

### 4.5.2 Open issues

Still, there are some possible roadblocks. Rb is an alkali which evaporates already at a very low temperature of around 60 °C. This has the consequence that it easily contaminates the whole vacuum chamber. In contrast lithium (Li) goes to the gas phase at around 150 °C. A pressure sensor operated with Li could hence be baked in order to minimize outgassing of contaminants [139]. The high temperature needed for evaporation also leads to outgassing. Hence creating a dilute vapor using e.g. light induced atomic desorption (LIAD) could be a possible method.
Another issue is the temperature dependence of the scattering process itself. This is especially critical for background gases consisting of molecules where the different rotational degrees of freedom couple to the Rydberg atom and lead to $n$- and $l$-changing collisions.
Unfortunately, the collisional processes happening when molecules collide with Rydberg atoms are not fully investigated. The presented experiment has in principle the potential to shed light on the elastic processes and at the same time allow the determination of the inelastic portion of the scattering process. However, the charges created by the photoeffect and the unpractical design of the glass cell inhibit such investigations. Of course one could calculate the inelastic collisional cross section from [106] and compare it to the linewidth

of the Rydberg transition. One would then argue that the remaining part of the cross section must be due to elastic collisions. Notwithstanding it would be desirable to compare this value to the shift, which is unfortunately not clearly identifiable or at least compare it to other literature values, which do not exist though. A possible experiment, which would allow to quantify the elastic processes is a modern version of the old fluorescence experiments. Rydberg atoms inside a dense Rb vapor with $N_2$ as a background gas are excited using a very weak Rydberg excitation. The fluorescence and hence the position of the Rydberg line is then monitored over a long integration time with a modern spectrum analyzer. Also $n$- and $l$-changing collisions might be quantifiable [149, 150]. The weak excitation ensures that no charges created by the Rydberg excitation disturb the measurement. Those charges might also have been the reason for an observed red shift in [128] at high temperatures.
Although there are still a lot of important questions to clarify until Rydberg excitation might become a serious functionally primary pressure standard, one should keep in mind that most other proposed spectroscopy based pressure standards suffer from very similar challenges.

# 5 Fabrication of vapor cells

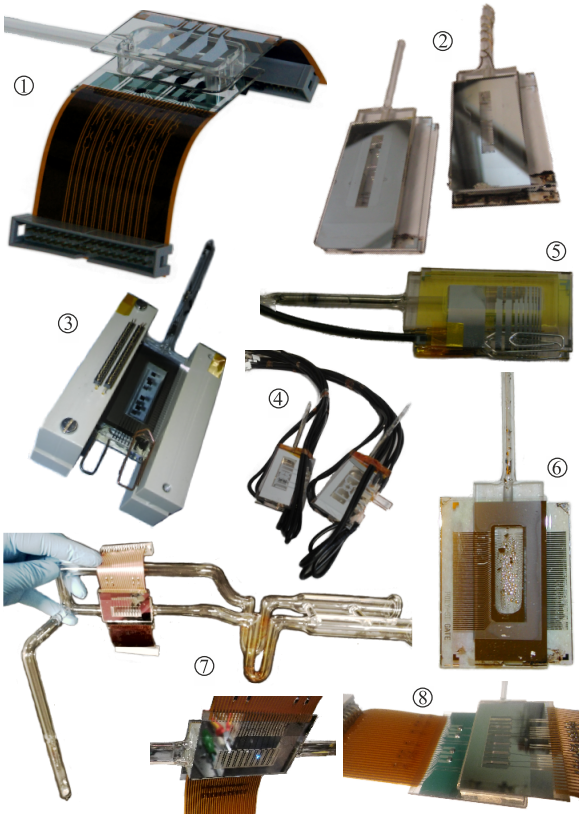


**Figure 5.1:** Selection of some of the vapor cells. Description on the next page.

**Selection of some of the vapor cells fabricated during this thesis**

1. Vapor cell used for the NO gas sensing experiment presented in Ch. 2. The glass substrates are glued on to the frame with an epoxy glue (Epo-Tek 251). The frame consists of quartz glass to allow the transmission of UV light through the cell frame.
2. Cells with a glass barrier in the middle. Made for an experiment in the group of C. S. Adams in Durham.
3. Vapor cell with operational amplifiers and ringoscillators based on an LTPS process inside. The contact to the feedthroughs is accomplished with pogo pins.
4. Cells with a special electrode design, which permits compensating electric fields in all directions and allows the realization of quadrupole fields. Made for an experiment in the group of J. Shaffer in Oklahoma. The electrodes are connected by gluing cables with conducting epoxy onto the thin-film metal layer.
5. Cell bonded with SiN as intermediate layer. On top of the electrodes lies a mono-layer graphene as transparent electrode. This was part of an investigation for finding a suitable transparent electrode material.
6. First encapsulation test of the LTPS TFTs. The feedthroughs connect the drain, source and gate contacts of TFTs, which are covered with the alkali metal Rb inside the cell.
7. Glass manifold used for the Rb-$N_2$ proof of principle experiment discussed in the chapters Ch. 3 and Ch. 4. The picture below is a closer few on the cell with the two entrance tubings.
8. Prototype of a cell with solid state amplifiers attached. The connections to the circuits are realized by ACF bonding a flexible flat ribbon cable onto the glass substrate.

The previous chapters were about the application of Rydberg physics to gas sensing and the underlying physics. Oftentimes the vapor cells in which the experiments were performed, have been mentioned. In this chapter the manufacturing of the cells will be explained. In general, glass cells containing alkali metals have to fulfill very different requirements:

- Optical access: For the present experiment and many other experiments involving Rb or Cs as the constituent of investigation, laser light roughly in the range between 450 nm and 800 nm has to be applied. Therefore the cell has to be transparent in the visible light spectrum, which naturally leads to glass as material of choice. Additionally, a cell fully made from glass has another advantage. We observed, that the vapor pressure can be set much more precise and a thermal equilibrium forms much quicker in a glass cell than in a steel chamber. For a thermalized vapor first the whole steel chamber needs to be coated by the alkali metal.

- Vacuum tightness: The experiments with alkali metals are mostly performed inside vacuum below 1 mbar. For some application, such as atomic clocks or rf-field sensing the alkali vapor is immersed in a certain well-defined buffer gas [119].

- Chemical resistance: Alkali metals react heavily with oxygen. Reactions of alkali metals and materials with functional OH groups lead to a release of hydrogen and hence a violent oxyhydrogen reaction at air. The result is a white alkali oxide. Alkali metals are also able to replace hydrogen from compounds, which leads to the formation of alkali salt compounds. By using glue or inappropriate sealing materials the cell might in the worst case be no longer vacuum tight. Yet, most often will the long-chained residuals remaining from the reaction with the alkali metal lead to an increase of collisional events and an unwanted broadening of the atomic transitions. This aggressive behavior prohibits for most applications the use of organic materials, such as most commercially available glues for example. An exception can be given, when the cell is constantly being pumped. Then any disturbing residuals will be pumped away, as was the case in the experiments presented in chapter 3 and chapter 4.

- Heat resistance: Rb goes to the vapor phase at around 60 °C [100]. For a decent optical density the experiments are therefore mostly performed at temperatures starting at 80 °C ranging up to 400 °C. A method to lower the constraints on the heat resistance and still allow the formation of an

optically dense vapor is for example the already mentioned LIAD method (see section 4.5.2).

- Size: A small cell is beneficial for most applications. It allows in general a more uniform temperature distribution across the excitation region and hence a better control on the alkali density. It also enables the application of vapor cells as chip-scale components in measurement devices.

- Other interconnects: The mere optical access is oftentimes not sufficient. But also the application of magnetic fields, rf-fields, the operation of technical components inside the vapor cell and also, as it is the case here, electrical feedthroughs connecting electrodes are necessary for a certain application.

The combination of the aforementioned requirements led to the development of a huge variety of vapor cells in all imaginable sizes and forms [151]. Especially the efforts to realize chip-scale atomic clocks has boosted the development of manufacturing techniques in the last years [152–155]. Others were cells with fibers fed through directly to the vapor [156]; very thin cells, consisting of a narrow slab between two glass plates [157]; cells with a very thin window on one side [119] to mention just a few. For all those cells a lot of development effort had to be taken.
The cell geometry that is used throughout this thesis was already presented in [20, 158, 159] and is in general the following: A frame consisting of standard borosilicate glass $(5 \times 3)$ cm in size and with a thickness of $(0.5 - 1)$ cm is used in which a hole of around $(3 \times 1)$ cm is drilled using ultra-sonic drilling. At one or sometimes two sides a hole with a diameter of around 0.3 cm is drilled and a glass tube is attached. This tube acts either as in- and outlet for the gas mixture or as a reservoir for the alkali metal. In this case the tube is heated to generate a certain vapor pressure, whereas the cell itself is kept at a higher temperature in order to omit excessive condensation of alkali metal on the cell surfaces. This tube is molded on to the glass frame. The molding process leads to a large waviness of the glass frame. Consequently the frame has to be polished mechanically to a surface waviness of $\lambda/2$ and better in order to comply with our method of attaching two substrates to the top and bottom of the glass frame. After the cell is finalized the reservoir tube is molded to a manifold consisting of a flange and a break seal containing the alkali metal. The whole manifold is pumped to a pressure below $10^{-7}$ mbar. Then the break seal is broken via a little steel ball and a magnet on the outside of the glass.

The metal is heated with a fan and a liquid alkali droplet is transferred to the cell by shaking the whole filling manifold. Afterwards the reservoir is manually melted off, while at the same time maintaining the vacuum pressure inside the cell and in the filling manifold. With this method in general a much lower background pressure can be achieved [155, 160].

## 5.1 Anodic bonding with aluminum

Apart from directly melting [161] or gluing [159] the two glass plates onto the glass frame, there is a method called bonding. During bonding of two materials, atoms diffuse into the other material or at least to the interface and lead to chemical interconnects between the two materials. Bonding processes have in general the advantage that they introduce only very little strain into the material, since the process takes mostly place at temperatures of at most only half of the melting temperature of the involved materials. One of the most used methods is direct bonding or also fusion bonding [162, 163]. Here, the two materials are polished to such a low waviness that the van der Waals interaction between the two plates pulls them together and leads to a chemical bond. A very similar method is diffusion bonding [164], but here the process does not take place at room temperature but instead at temperatures of around one half of the melting temperature and often pressure is applied additionally. Another often used method is eutectic bonding [165–168]. One of the materials is coated with e.g. Au, which together with Si for example forms a binary alloy with an eutectic point. The melting temperature at this eutectic point is lower than the smaller melting temperature of each of the two materials. Hence, the materials can be bonded at a temperature lower than the melting temperature. This is also the underlying principle of glass transfer tape.
Apparently, all bonding methods have in common that only materials with a very similar coefficient of thermal expansion can be connected. Otherwise the bond would crack up again during cooling down from the bonding process. This also applies to the bonding process we use: that is anodic bonding.

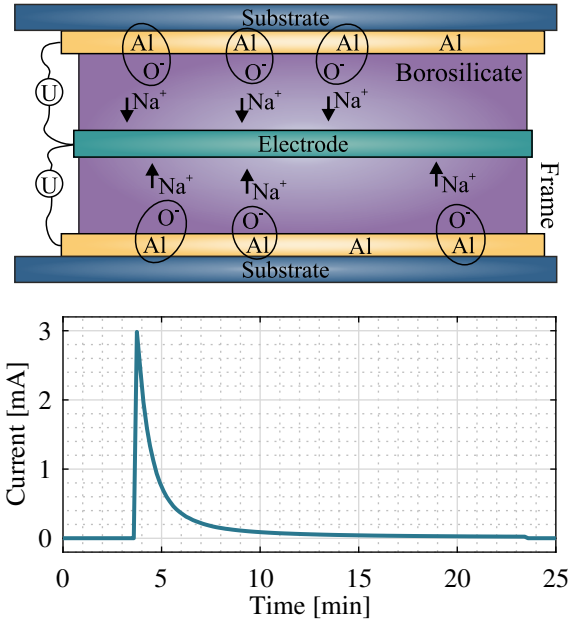


**Figure 5.2:** a) Schematic of the bonding process. b) Total current flowing across the borosilicate frame during the bonding process.

### 5.1.1 Method

There are several variations of the anodic bonding method [169–171]. The method is used for example to place silicon and also silicon on insulator wafers on glass [167, 172, 173]. One can also bond massive pieces of metal on to glass [174, 175] and various materials are suited as intermediate layer [176]. For the process pursued here, a metallic intermediate layer of Al with a thickness of around 100 nm is sputtered onto the glass substrate. The glass substrate is made from Corning XG borosilicate glass. This glass is a special display grade glass with no alkali content in it. This allows using this substrate material also at elevated temperatures in e.g. chemical vapor deposition without contaminating the machine with highly mobile alkali residues. The other material, in

this case the frame, has to contain a certain amount of alkali oxides. In the case of standard borosilicate glass, here Schott Borofloat 33, this is up to 4 %. In general one can use different intermediate layers, but for this kind of anodic bonding mostly Al is used. This also introduces the least problems regarding material-process compatibility into the fabrication process. The thickness of the Al layer is not crucial, but should be more than 10 nm to still provide a good anode. On the other hand the thickness should be less than 200 nm, since thicker layers of Al tend to crack during cooling down. This is because the coefficient of thermal expansion is ten times higher for Al than it is for borosilicate glass.
After a thorough cleaning of all materials involved the coated substrates are placed on the top and bottom of the borosilicate frame, as it is shown in the schematic in figure 5.2. A wire is wrapped around the center of the frame and acts as cathode, whereas the Al layer acts as an anode. The whole stack is heated up to a temperature of 300 °C and held at this temperature for around 20 minutes to allow thermalization of the whole stack. At this temperature the $NaO_2$ molecules inside the borosilicate frame crack up. By applying an electric field between the wire and the Al layer, the highly mobile $Na^+$ ions diffuse towards the negatively charged wire, whereas the immobile $O^-$ cations stay at their position. The field is up to 4 kV/cm. The $O^-$ cations at the interface form now $AL_2O_3$ molecules with the atoms of the Al layer.

### 5.1.2 Results and advantages

The current during the bonding process is shown in figure 5.2. It increases sharply before it slowly drops. The steep rise marks the time at which the $Na^+$ ions start to diffuse to the cathode. The slow decrease is due to the formation of a depletion region in the vicinity of the materials' interfaces [177–180]. After approximately 20 minutes no significant current is flowing anymore and the process can be stopped. The finished cell is then cooled down slowly over the course of one hour to omit a thermally induced cracking of the bond.
The figure 5.3 shows microscope slides of the finalized bond. In the first picture, which was taken when the sample was illuminated from the bottom, one can see a lot of speckles appearing in white. Those are regions where the whole Al was used up to $Al_2O_3$, which appears transparent. Converting all Al to sapphire is in general not possible, since the Al layer also provides the anode. The second image shows the regions around electric feedthroughs. The feedthroughs can

be as thick as 200 nm and the cell will not show any leakages. Between the feedthroughs and the Al layer is a dielectric layer of chemical vapor deposited SiN with a thickness of 600 nm. This layer will later act as encapsulation layer for the active electronics inside the cell. It also prevents the Al layer from growing dendrite-like spikes into the substrate material [175] and thereby short-circuiting any active electronics. This can happen, when Al is heated up and the Al atoms become mobile. Of course, the region directly around the feedthroughs is not as well bonded as the rest and is therefore also the first weakness, which will be deteriorated by the alkali vapor. This is shown in the third picture. There, Rb metal is already creeping in the gap between the frame and the substrate. Still, a cell made in such a manner can easily maintain its quality for more than three years even during rugged handling, for example numerous heating cycles up to 300 °C and above.

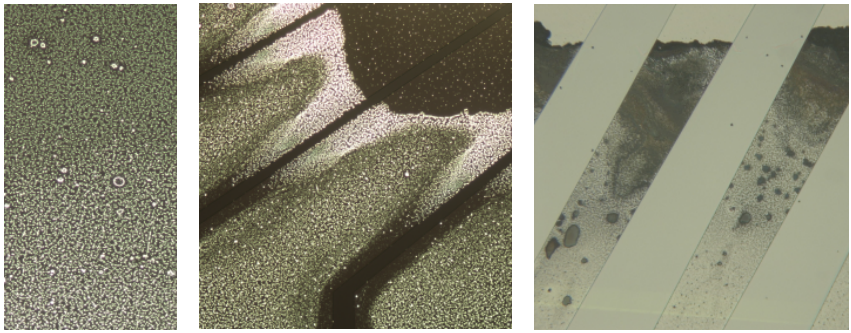

**Figure 5.3:** Microscope slides showing the bonded areas illuminated from the bottom. The description is in the text.

Another very similar method for building such cells is by using again anodic bonding, but this time by utilizing a layer of 100 nm thick SiN. This method for assembling vapor cells was introduced in [158, 170, 176]. An advantage of the SiN bond is the lack of metal in the bond, which makes an isolation layer between the wires and the bond unnecessary and leads to lowest parallel stray capacitance. Additionally, it simplifies the application of rf electric fields from the outside, e.g. with a horn.

However, there are two drawbacks. First, both glass pieces in contact have to contain alkali oxides, which makes the use of e.g. alkali free display grade glass impossible. Second, the surface quality and cleanliness of the glasses have to be far better than for bonding using Al. This allows a thickness of only 20 nm and makes the whole assembly of a vapor cell more failure prone. Nevertheless, a successfully SiN bonded cell can survive similar treatment like the Al bonded cells.

# 6 Current detection

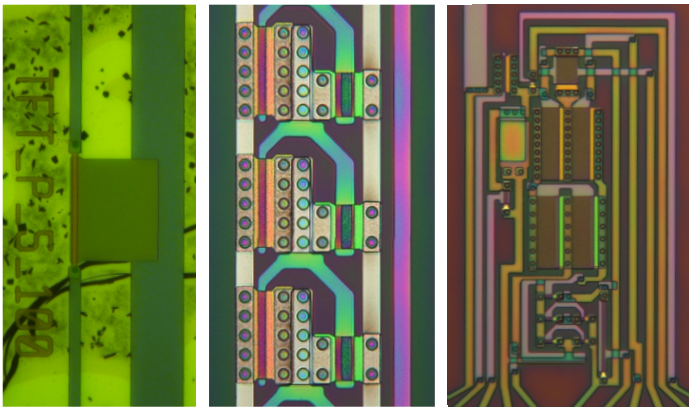

**Figure 6.1:** a) p-type TFT underneath bulk Rb, imaged from the bottom. b) Part of a ringoscillator intended for measuring the switching time of inverters and their change of characteristics due to further process steps, such as anodic bonding and exposure to alkali vapor. c) Microscope image of the charge sensitive amplifier. This one is additionally coated with spin on glass (similar to the ringoscillator in b)), which was intended to planarize the vias of the drain/source contacts and hence help to improve the SiN encapsulation. This additional planarization turned out to be unnecessary.

This chapter deals with one of the main technical parts of the previously introduced experiments; namely the current amplifier that is used to amplify the Rydberg created ionization current. As already explained in chapter 1 the current is directly proportional to the population of the excited Rydberg state. Compared to the measurement of the fluorescence of the decaying Rydberg states it can be measured with much better signal to noise ratio, since it can be directed onto one electrode rather than radiating in all spatial directions.

Depending on the type of experiment the current amplification should fulfill several requirements on which the following discussion is focused:

- Gain: The amplified output signal should be in the range of 0.1...1 V in order to be compliant with the bit resolution of analog to digital converters.
- Bandwidth: In chapter 2 the bandwidth had to be on the order of MHz, in chapter 3 and chapter 4 the bandwidth should at best be more than several kHz to allow experimental practicality without harmonic distortion. Also the application of an Lock-in amplifier could in future be advantageous for the recovery of small signals from $1/f$ noise.
- Noise: The best performance is achieved when single charges can be measured or the noise of the amplification is limited by the shot noise created by the incoming current.
- Decoupling: Rydberg atoms are very sensitive to electric fields and can be shifted out of the excitation frequency bandwidth for sufficiently large electric fields. In that sense a Rydberg created current is not an ideal current source, since it can not provide arbitrarily large voltages to drive the current. Hence, in order to not compromise the Rydberg experiment the measurement of the current needs to be decoupled from the Rydberg excitation.
- Chemical resistance: As already mentioned in chapter 5 every device in contact with the alkali vapor needs to be encapsulated in order to not deteriorate.

In most cold atom experiments investigating Rydberg states, one also tries to measure the population via detection of ions [14]. In contrast to the experiments presented here, in such experiments the ions are created via state-selective electric field pulses, since the collisional rates are being kept low to ensure long lifetimes of the excited states. The single ions are then measured using a channeltron or a microchannel plate, where the impinging charges create a charge avalanche inside the device. With such a device, single charges can easily be resolved on timescales as low as some picoseconds with nanoseconds in between for recovery. The dark counts are mostly on the order of 10  Hz. The drawback is that those avalanche devices must be operated at pressures below $10^{-6}$ mbar to prevent a breakthrough inside the device [15]. Additionally, the semiconducting surface of the multiplier tubes do not withstand the chemically

reactive alkali metals, at least not in such comparatively large amounts as they are occurring in the experiments here. So, in some sense these multiplier tubes are the ideal device to measure the Rydberg current apart from not being applicable at high pressures and in alkali vapors as dense as here.
Oftentimes thermionic diodes were used to measure the Rydberg created charges. This approach was not taken into account here, since these devices are hardly scalable and have a comparatively large volume. Additionally they show different sensitivities depending on the type of gas flowing through and their properties can vary a lot when exposed to sticking materials in particular alkali metals [16, 17].
A much simpler method could be to translate the current into a voltage simply by using a resistor. A simple resistor is more or less easily fabricated and can in any case be encapsulated sufficiently well. The overall current noise $i_n$ created by this measurement is given by the square root of the sum of squares of the thermal noise $i_t$ and the shot noise $i_s$ of the current $I$ itself [181]:

$$i_n = \sqrt{i_t^2 + i_s^2} = \sqrt{\frac{4k_B T}{R} + 2 \cdot e \cdot I}. \tag{6.1}$$

For a current of 1 nA the shot noise would be larger than the thermal noise of a resistor with a resistance of $> 50$ MΩ. For the geometry of the vapor cells used in this thesis, the capacitance of the Rydberg current collecting electrodes is on the order of 4 pF. Hence, the bandwidth would be on the order of 800 Hz. This is the highest achievable value, while still being shot noise limited. Yet, the output voltage is only 50 mV. Additionally, the output voltage is directly applied onto the Rydberg atoms, which are hence shifted out of resonance by an energy given by the Stark effect (see section 4.1). This shift is getting larger for higher resistance values.
A natural choice for the amplification of a current is a so called transimpedance amplifier (TIA). This operational amplifier circuit provides high gain together with high bandwidth at low noise and decouples the current source from the measurement device. The approaches we took to implement such an amplifier into the vapor cells and their properties are presented in the following. First, general properties of this circuit are introduced and the results of our different approaches are compared. Then the single circuit implementations are explained separately.

## 6.1 Transimpedance amplifiers

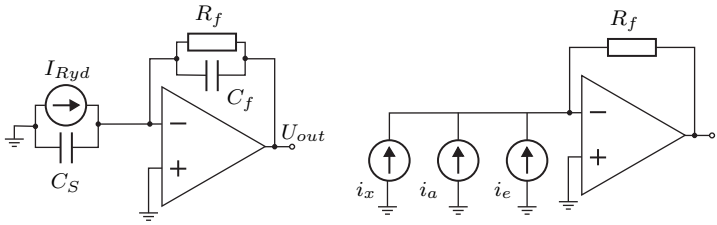


**Figure 6.2:** a) Schematic of the TIA circuit with the feedback resistor $R_f$ and compensation capacitance $C_f$. The current $I_{Ryd}$ is created by the Rydberg excitation and collected with electrodes with a capacitance $C_s$. b) Equivalent TIA circuit symbolizing the different noise contributions. $i_x$ is the noise of the source, which also includes shot noise, $i_a$ is the amplifiers' current noise and $i_e$ is the current noise created by the voltage noise $e_a$ of the amplifier.

The circuit of a transimpedance amplifier is depicted in figure 6.2 a). Starting on the left side of the schematic, the current source is shown with its' intrinsic capacitance $C_s$. An intrinsic resistance is not taken into account. The capacitance also includes the input capacitance of the operational amplifier.
The output of the amplifier is fed back to the inverting input node via a resistor $R_f$. As long as the voltage difference at the input nodes is not zero, the amplifier will swing the output voltage by an amplitude, which is the input voltage difference times the open-loop gain of the amplifier. In order to keep the input nodes at zero voltage difference, the amplifier has to drive a current back through the feedback, which is as large as the incoming current $I_{Ryd}$ [111]. The output voltage necessary for this current is given by

$$U_{out} = -R_f \cdot I_{Ryd}. \tag{6.2}$$

The inverting input node of the amplifier will hence be on the same potential as the noninverting input as long as equation (6.2) holds across the covered frequency range and for a perfect operational amplifier. The inverting input is therefore also called virtual ground. The input impedance of this circuit is consequently zero, whereas the output of an operational amplifier can drive as much current as required. It is hence a perfect current drain with a low input impedance and a perfect voltage source also with a low impedance. This is why

this circuit is called a transimpedance amplifier and why this circuit is suited best for the measurement of small currents.

### 6.1.1 Gain, bandwidth and noise

There are numerous books and papers written about the correct layout of TIAs [111, 181, 182]. A notion all author eventually agree on is that the interplay between the single components is rather complex and should be tested and tweaked on the actual circuit rather than putting hands on with equations and simulation programs. There are still some rules of thumb, which will be summarized in this chapter.
The basic challenge in designing an TIA circuit is the following. The capacitance $C_s$ including the source capacitance as well as the capacitance of the input nodes of the amplifier form a lowpass filter together with the feedback resistor $R_f$. At the rolloff frequency $f_{RC} = 1/(2\pi \cdot R_f \cdot C_s)$ this lowpass filter will induce a 90° phase shift on the signal. The amplifier itself also acts as a lowpass element with rolloff frequency $f_T$ being equal to its' gain bandwidth, which one can retrieve from the datasheet or simulations respectively. At some frequency $f_i$ the output signal will be 180° out of phase with the input signal. Since the output signal is fed back to the input it will be superimposed constructively with the input and hence the circuit will start to oscillate on its own and become unstable. In order to recover stability one includes a feedback capacitance $C_f$ in parallel to $R_f$. This reduces the phase shift for high frequencies and suppresses this oscillating behavior[1].

**Gain:** The overall frequency dependent output voltage for a real amplifier without considering possible offset voltages is given by [111]

$$U_{out} = \frac{-R_f}{1 + \frac{1}{A_{OL} \cdot \beta}} \cdot I, \tag{6.3}$$

[1] $C_f$ is chosen in the following way [111]. If $\left(\frac{R_f}{R_{in}+1}\right) \geq 2 \cdot \sqrt{f_T \cdot R_f \cdot C_s}$, then $C_f = \frac{C_s}{2 \cdot \left(\frac{R_f}{R_{in}+1}\right)}$. If this does not hold, then $C_f = \sqrt{\frac{C_s}{f_T \cdot R_f}}$.

where $A_{OL}$ is the open-loop gain of the amplifier and $\beta$ is given by [111]

$$\beta = \frac{1 + R_f \cdot C_f \cdot 2\pi \cdot f}{1 + R_f \cdot (C_s + C_f) \cdot 2\pi \cdot f}. \tag{6.4}$$

**Bandwidth:** The -3dB rollover frequency of the uncompensated TIA is the geometric mean of the rollover frequency of the input lowpass filter and the gain bandwidth of the amplifier [111]

$$f_{CL} \approx \sqrt{f_{RC} \cdot f_T}. \tag{6.5}$$

By using a proper feedback capacitance for the frequency compensation this frequency reduces roughly to [111]

$$f_{-3\text{dB}} \approx \frac{\sqrt{f_{RC} \cdot f_T}}{2}. \tag{6.6}$$

Compared to a simple resistor as current to voltage converter the TIA circuit can boost the bandwidth of the current to voltage conversion if one uses an amplifier with sufficiently large bandwidth.

**Noise:** The noise created by the TIA circuit has several contributions. First, the amplifier itself shows current noise $i_a$ as well as voltage noise $e_a$ referred to its input. The voltage noise translates via the feedback resistor into an effective current noise $e_a/R_f$ at the input. Additionally, the voltage noise will translate via the input capacitance $C_s$ into a frequency dependent input current noise $e_a \cdot 2\pi \cdot C_s \cdot f$. Apart from this, the feedback resistor will induce thermal noise $\frac{4k_BT}{R_f}$. Including any further non-thermal excess noise $i_x$ of the current source leads to the following overall noise [183]:

$$i_n = \sqrt{\left(\frac{e_a}{R_f}\right)^2 + e_a^2 \cdot (2\pi \cdot C_s \cdot f)^2 + i_a^2 + \frac{4k_BT}{R_f} + i_x^2}. \tag{6.7}$$

For a design with as low noise as possible there are consequently the following rules of thumb to obey:

- The amplifier should not only have low current noise, but even more important, low input voltage noise.
- The input capacities should be kept as low as possible.
- $R_f$ should be chosen as large as possible.

### 6.1.2 Overview of the different implementations

There exists an abundance of possible circuits with which existing TIA designs can be improved, such as an input cascode, bootstrapping or building a composite amplifier, where the TIA is followed by another amplifier [111, 181, 182]. During the course of this thesis several approaches were investigated to design and produce a TIA that fulfills the gain and bandwidth requirements of the experiment as well as being as noiseless as possible. The properties of the amplifiers are summarized in table 6.1 and their root mean square noise density is plotted in figure 6.3. For this purpose a time trace was measured for zero current flowing into the TIA circuit with the glass cell attached to the input node of the TIA. The calculated current signal was Fourier transformed into the frequency domain and the square of it summed up to the 3 dB bandwidth of the circuit and normalized by this bandwidth. The square root yields then the spectral current noise density.
Also plotted in figure 6.3 is the shot noise $i = \sqrt{2 \cdot e \cdot I}$ that one obtains from a current $I$ that is large enough to provide 1 V output voltage at a given amplification [181]. This is depicted as green line. The output voltage of 1 V was chosen arbitrarily but with the reasoning in mind that 1 V is an easy measurable and realistic value in terms of further signal processing such as analog to digital conversion with high bit resolution. This serves to generate a feeling for the magnitude of noise values.
The various amplifier setups are summarized in the following overview.

**DL 1211:** In chapter 3 and chapter 4 all measurements were performed using the TIA Model 1211 by DL Instruments. This general purpose TIA has already been used in a huge variety of physics experiments and also in the PhD thesis by Renate Daschner [20]. The gain can be set manually over several decades and

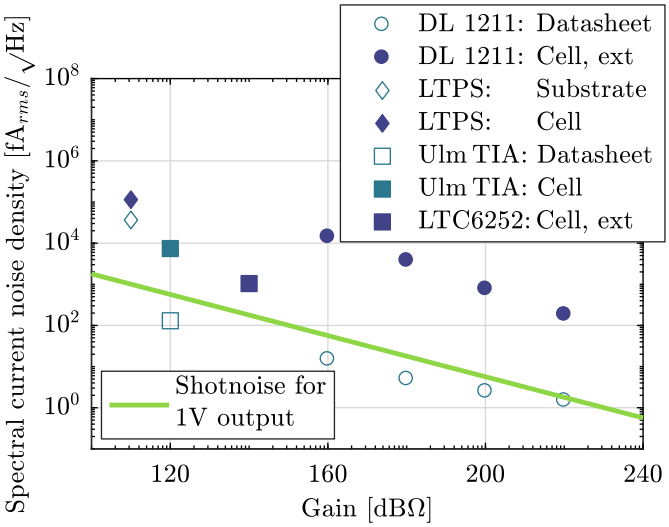


**Figure 6.3:** Spectral current noise density for the TIAs used in the different experiments presented in this thesis. The green line depicts the shot noise one obtains when measuring a current that is large enough to create 1 V output voltage at a given current to voltage transimpedance gain.

for all measurements the bandwidth was limited to 1 kHz by an internal lowpass at the output. The current noise density as specified in the datasheet [184] is plotted in figure 6.3 as empty circles. In contrast the noise density one obtains in the experiment is depicted as filled circles and is clearly above the chosen shot noise limit. The reason for the increased noise is the additional capacitance at the input of the amplifier emerging from the cell's capacitance and the shielded connection wires. A lot care was taken to omit any ground loops and ensure a proper unbroken shielding along the signal path. Still the glass cell with the unshielded electrodes inside picks up a lot of stray electromagnetic noise. Additionally, there is a lot of microphonic noise on the signal. This noise is created by slight bending and shaking of the connecting leads. The dielectric insulation gets quenched and due to the piezo electric effect varying electric fields are induced in the signal wire [185]. This kind of slow noise uncorrelated from the signal generation can in principle be circumvented by utilizing a Lock-in amplifier.

**LTPS:** One way to further decrease the input capacitance is to place the TIA as close as possible to the current source. In our case that is directly inside the cell at the point of the alkali vapor. Since there is no known way to encapsulate a common solid state amplifier in die form we decided to build an amplifier directly on glass. The best known technology for realizing active electronics on glass is based on low temperature polycrystalline silicon (LTPS). Methods like this are very common in the fabrication of e.g. high-resolution active matrix displays [186, 187]. Although working amplifiers based on the LTPS process were built and operated in an encapsulated cell filled with Rb (see section 6.2), the handling and especially the fluctuations between each device made a practical use of the amplifiers challenging. Furthermore, the noise performance of the TIAs is not competitive with e.g. the Ulm TIA as can be seen in figure 6.3. There the current noise density is plotted for the bare device on the substrate and also for the TIA inside the cell with the electrodes attached. Although the noise is rather large one should take into account that no means of shielding or decoupling from noise in the power supplies were taken.
The LTPS technology is intended for switching between two voltage levels without excessive loss of power, as it is required for active-matrix displays. In general, transistors based on polycrystalline silicon show a bunch of detrimental properties, which nevertheless allow the realization of complex electronic circuits. More insight in the fabrication process and the properties of the transistors will be given in section 6.2.

**Ulm TIA:** In chapter 2, two different TIAs were used. One of them was provided by the Institute for Smart Sensors at the University of Stuttgart, which was formerly at the University of Ulm [74]. This TIA utilizes a so called pseudo-resistor, which realizes the transimpedance using appropriately biased transistors. In this way the transimpedance gain becomes immune against temperature fluctuations, voltage changes as well as variations in the fabrication process. The whole device is based on silicon on insulator (SOI) technology, which allows to realize very fast electronics. The transimpedance can be set externally with one single resistor. This allows to set the transimpedance gain from 1 MΩ to 1 GΩ with a bandwidth as high as 2 MHz. For the experiment presented in chapter 2 a very high bandwidth was needed to measure the arrival of the charges created by the nanosecond short excitation pulses without harmonic distortion. The gain was therefore set to 1 MΩ to achieve the 2 MHz bandwidth and a minimum current noise density at this design bandwidth of

$1.3 \cdot 10^{-13}$ A/$\sqrt{\text{Hz}}$ according to [74]. The TIA was attached directly to the side of the glass cell as shown in figure 2.1. The process technology for the interconnect will be explained later in section 6.3.1. The bias resistor for setting the gain and also the whole circuit supplying the voltage to the TIA were connected via a flat ribbon cable to the cell.
The noise density measured in the experiment is roughly 15 times more than originally measured in [74] owing to several reasons. First, the current noise is increased due to the input capacitance, which was around 3.5 pF. Second, since the supplies are some distance apart from the supply nodes of the TIA the noise filtering and buffering of current demand was only insufficiently achieved. Additionally the increased length of the connection between the bias resistor and ground led to an additional inductance. In such a case the biasing of the amplifier lags behind the global fluctuations of the ground plane and hence shows fluctuation with reference to ground. Above all, the cell to which the amplifier was attached, was not shielded at all. It needs to be remarked that the current noise density given by [74] is only the minimum noise density at the design bandwidth. The rms value is expected to be much larger, since the $1/f$ noise will increase for lower frequencies.

**LTC6252:** This is a self-built TIA circuit, which was also used for the measurements shown in chapter 2. The circuit is explained in section 6.3.2. This circuit was placed on a PCB board and connected to the electrodes inside the glass cell with a flat ribbon cable. Due to its design it shows very low noise for small frequencies but nevertheless a lot noise for high frequencies. The reason is that this circuit was intentionally designed for a bandwidth of at least 2.5 MHz. Additionally, as was the case for the Ulm TIA the cell with the electrodes attached to the TIA was not shielded against external electromagnetic noise.

**Table 6.1:** Summary of the most relevant properties the TIAs used in the presented experiments.

| Name | DL 1211 | LTPS | Um TIA | LTC6252 |
|---|---|---|---|---|
| Position | External | Internal | Cell | External |
| Gain [dBΩ] | 160 . . . 220 | 110 | 120 | 140 |
| Bandwidth [Hz] | $1.0 \cdot 10^3$ | $1.0 \cdot 10^4$ | $2 \cdot 10^6$ | $2.5 \cdot 10^6$ |
| Noise [A/$\sqrt{\text{Hz}}$] | $1.4 \cdot 10^{-11}$ @160dBΩ | $1.1 \cdot 10^{-10}$ | $7.4 \cdot 10^{-12}$ | $1.0 \cdot 10^{-12}$ |

## 6.2 TIA based on an LTPS process

Glass as a substrate material has the drawback that it is amorphous and hence its surface properties are not periodic on an atomic scale. Nevertheless, active semiconductor devices can be realized on glass for example for active matrix displays. Apart from organic semiconductors or amorphous silicon (a-Si) a wide range of devices are based on polycrystalline silicon (poly-Si). This is silicon, which is crystalline only across several micrometer wide domains, but shows mobilities of up to $100\frac{\text{cm}^2}{\text{Vs}}$ for electrons and up to $60\frac{\text{cm}^2}{\text{Vs}}$ for holes. This is more than a factor of ten more compared to a-Si, which additionally shows no usable mobility for holes. Hence, complementary circuit consisting of $n$- and $p$-type transistors on basis of poly-Si are possible.
As already mentioned, this technology has some drawbacks, which will be explained after the process was introduced in some detail. The development of the fabrication process was not part of this thesis [186, 188], yet ever necessary adaption onto the condition of the cleanroom facilities had to be done nevertheless. A challenge was to encapsulate the CMOS structures against the aggressive alkali vapor and to match the process to the necessary bonding layer (see chapter 5) [2]. A rough summary of the process steps will be given now.

[2] Detailed information on the exact machines, chemicals and process details will not be given due to the protection of intellectual property rights on the side of the Institute for Large Area Microelectronics. Nevertheless, all process steps are well documented and can be asked for at the executive persons, e.g. Prof. Dr. Norbert Frühauf.

For more details I refer to [186, 188–190]. Each process step is illustrated in figure 6.4.

### 6.2.1 LTPS process

The fabrication starts of by depositing a $SiO_2$ layer as buffer onto the display-grade glass substrates. This buffer layer serves as thermal decoupling of the semiconducting structures from the substrate and acts as a diffusion barrier. Directly afterwards a layer of $n^+$-doped microcrystalline silicon is deposited with the same plasma enhanced chemical vapor deposition (PECVD). The microcrystalline property of Si is achieved by mixing hydrogen in addition to the silane base material. The plasma enhanced deposition always leads to some part to an etching of the growing layer. The hydrogen assists in saturating open bindings in plasma created silane radicals. In this way less well bound amorphous silicon structures are more likely to be etched away than better built-in microcrystalline silicon. Furthermore the hydrogen prolongs the diffusion length along the surface and thereby silicon atoms can be built more easily into the crystal structure. The result is a layer consisting of a huge amount of randomly oriented crystalline domains.
After structuring the $n^+$-doped islands with a plasma etching process, amorphous silicon is deposited with PECVD. This time the plasma contains again a lot of hydrogen to saturate open silane bindings. Like this, a lot of hydrogen in the plasma leads to less built-in hydrogen in the deposited layer. The plasma energy is chosen less to omit etching of the anyway better bound microcrystalline layer. The substrates are annealed in vacuum at 450 °C for several hours to allow outgassing of remaining hydrogen. This is necessary that the following recrystallization step does not lead to an ablation of the layer.
The amorphous silicon is then recrystallized to polycrystalline silicon using an Excimer laser. A 210 ns long UV pulse shortly melts the a-Si layer, such that the Si atoms can restructure into large domains consisting mainly of crystalline Si. At the same time the phosphor of the heavily doped $n^+$-islands diffuses into the poly-Si such that in vertical direction a heavy doping is accomplished, which allows ohmic contacts to the drain/source metalization. In lateral direction the doping gradient leads a gradual transition to the intrinsic Si of the semiconducting channel.
The poly-Si is then structured and a 100 nm thick gate oxide is deposited with PECVD. On top, the gate metal is deposited, for which an alloy consisting

of molybdenum and tantalum is used. The gate overlaps a bit with the the $n$-doped islands, such that a GOLDD (gate overlapped low doped drain) structure is created. The MoTa metal alloy is especially resistive against radiation damage occurring during the now following ion implantation step, which includes another exposure to the Excimer laser created UV light pulse.
The $p^+$-doped islands are realized by implanting $BF_2$ ions. There is no further mask needed for this step, since the gate metal acts as a shield across the channel region. Nevertheless, the implantation energy and dose is chosen such that the $n$-doped regions still remain mainly $n$-doped. To ensure a proper integration into the crystal, this step is followed by a further activation step using the excimer laser, but this time at a pulse energy below the melting point.
Afterwards the semiconducting structure is covered with a layer of PECVD deposited SiN. In order to contact the drain/source regions, vias are etched through the SiN as well as the buffer oxide using a two step reactive ion etching process. Then the drain and source contacts are realized using an alloy of Aluminum and Neodymium. The Nd inside the alloy prevents the Al from growing hillocks into the material underneath or above during higher temperature deposition processes [175]. To prevent oxidation again a layer MoTa is deposited on top of the AlNd layer.
Like this the TFTs are nearly finished. For the encapsulation they are covered with 600 nm SiN and 100 nm Al for the bonding frame. The SiN is structured after the lithography step of the bonding frame to prevent etching of the drain/source metalization during the wet etching of the bonding frame. The whole process is finished by a last annealing step under inert gas. This helps to further increase the integration of the $p$-doping as well as to neutralize possible built-in charges.

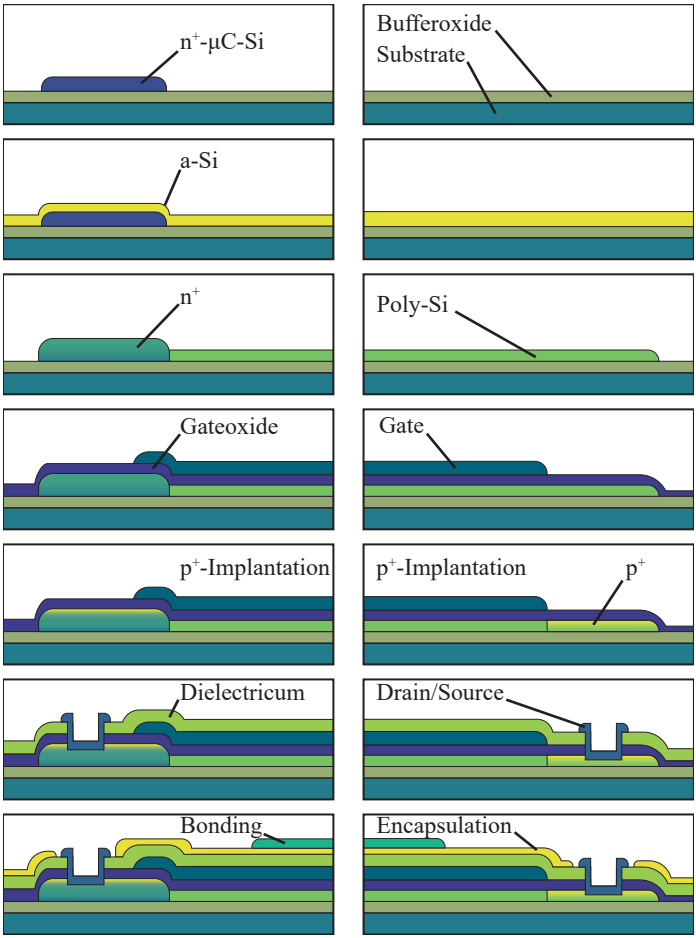


**Figure 6.4:** The employed LTPS process. Left: *n*-type TFTs; Right: *p*-type TFTs.

The final substrates are then cut into a suitable dimension for the cell manufacturing (see chapter 5). In figure 6.5 the characteristic input curves for $n$- and $p$-type TFTs are plotted. First before the anodic bonding, then after the bonding and then also after being exposed to Rb for more than a year. As a proof, a TFT buried underneath a droplet of Rb is shown in figure 6.6 a). Clearly, the characteristics of the TFTs were not affected by the alkali exposure and hence the encapsulation worked perfectly fine. There are unfortunately some drawbacks of the employed technology, which are explained now.

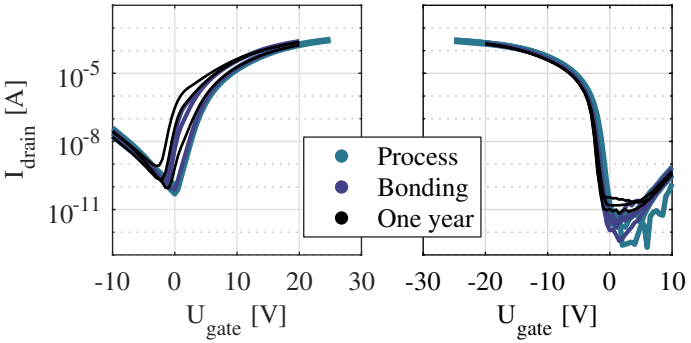


**Figure 6.5:** Input characteristics of the fabricated TFTs operated inside a bonded cell filled with Rb. First, directly after the finished fabrication, then after the bonding process and last, being exposed to Rb for more than one year. Left: $n$-type TFTs; Right: $p$-type TFTs.

**Subthreshold conduction:** As can be observed in figure 6.5 the TFTs show an increased conduction below the threshold voltage at the gate node. This is caused by the large amount of defects inside the channel. At those defects electron-hole pairs can be generated, which allow an injection of holes at a negative gate voltage. These will then contribute to the current from drain to source. This is also the reason why at least some picoampere are always leaking through.

**Shift of the cutoff voltage:** Also visible in figure 6.5 is that the cutoff voltage is not always at zero volts. This is also caused by charges trapped at the crystal defects, which have to be saturated before a current can start to flow.

**Saturation behavior:** In figure 6.12 the output characteristics are shown for different gate voltages. The drain current increases even for a TFT operated in saturation. This is first of all due to a channel length modulation, since the channel has some resistance at which a drop of the drain/source voltage occurs over the length of the channel. Another reason is the Kink effect, which occurs for high electric fields at the drain/channel interface. This leads to electron-hole generation by collisional ionization. This current increases exponentially with increasing drain/source voltage caused by the avalanche effect. This can partly be avoided by e.g. realizing the drain/channel interface as the already mentioned GOLDD transition, but in general it occurs in all SOI FETs.

**Parameter drift:** The characteristics of the TFT can change over time, especially when operated with a continuous current for a longer period of time. Although this is not as significant as in the case of organic semiconductors, it is still observable.

**Size and matching:** Due to the unavoidable variations on the substrate and the huge amount of crystal defects, the TFTs have to be rather large, in the range of at least 3 $\mu$m. This allows to average the behavior of the TFT over several crystal domains. Since we are building the electronics on our own, a lot of the variations on one single substrate as well as from substrate to substrate are caused by the way the substrates are handled. Unfortunately, this depends heavily on the experience and skill of the person fabricating the transistors.

### 6.2.2 Architecture of the TIA

Although the TFTs show some disadvantages it is still possible to realize operational amplifiers. One such design is sketched in figure 6.7. This design was first introduced in [187, 190, 191] and was modified during the course of this thesis in order to end up with a stable TIA [192]. A picture of the finalized TIA is shown in figure 6.6. The TIA has a size of $(230 \times 520)$ $\mu$m. It consists of a differential $p$-type input stage, those are the two large TFTs at the left of figure 6.6 b). The $p$-type TFTs show no gate overlap compared to the $n$-type TFTs and are therefore most suited for this application, since they have essentially no additional capacitance. They are chosen as large as reasonable. On

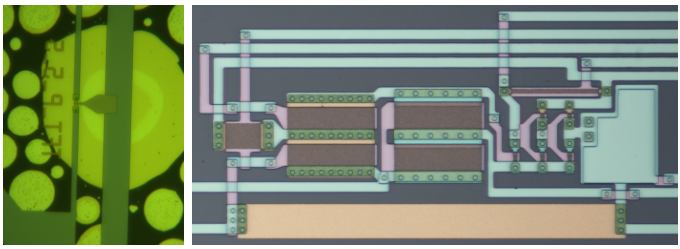

**Figure 6.6:** a) Microscope image of a TFT buried underneath a macroscopic droplet of Rb. b) Image of the TIA, which has a size of $(230 \times 520)$ $\mu$m including supply lines.

the one hand the bandwidth will decrease with larger TFTs, on the other hand the input stage will have less input offset voltage due to a better matching of the TFTs. The same applies to the current mirror following the input stage, which acts as a load. The input stage has its' own current source, which can be controlled by externally applying a voltage $V_1$. This is the single TFT on the far left of figure 6.6 b). This TFT is of course intended to be operated in saturation, but can also be abused to let the input stage current-starve. Thereby the bandwidth can be decreased artificially in case the circuit tends to show unstable oscillations.

After the input stage follows the amplification stage, which consists of one $n$-type TFT followed by two inverter stages. These boost the output signal further. The amplification TFT has again its' own current source controlled by $V_2$. This is necessary, since the inverter based on the technology at hand will never work symmetric. This is due to the different charge carrier mobilities and threshold voltages. With $V_2$ the symmetry of the amplifier can be set by some extent and hence helps to compensate for process variations.

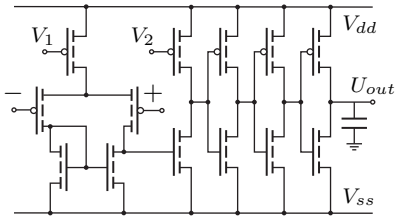


**Figure 6.7:** Schematic of the amplifier circuit.

The supply voltages $V_{dd}$ and $V_{ss}$ are typically in the range of $\pm 20$ V. $V_1$ and $V_2$ were set to $-10$ V and $-15$ V below $V_{dd}$.

The TIA is then realized by putting a resistor in the feedback path from the

output to the inverting input node. This resistor is realized as a strip of poly-Si. This has several drawbacks. First the exact value will be temperature dependent. Second, due to process variations the absolute value of the resistor is not known exactly. On average it was $(70 \pm 15)$ kΩ. Since the input capacitance of the electrodes collecting the Rydberg created charges is only 10 fF at most, one can omit any frequency compensating capacitance in the feedback path. A lowpass capacitance of 3.5 pF at the output of the amplifier was used nevertheless in order to cut off noise and prevent excessive peaking in the frequency response.

### 6.2.3 Results

The final amplifier has an open loop gain $A_{OL}$ of 300 up to 1000. The unity gain response of the amplifier configured as voltage follower as function of the input frequency is shown in figure 6.8. There the bandwidth is around 50 kHz but can be up to 100 kHz depending on process variations. A little peaking is visible, which a lot of amplifiers show in this configuration but which can easily be compensated in the final application. Although the relative matching error of the input TFTs is less than 2% in the linear region for small signals, the amplifiers often have an input offset voltage between 100 mV and 500 mV.

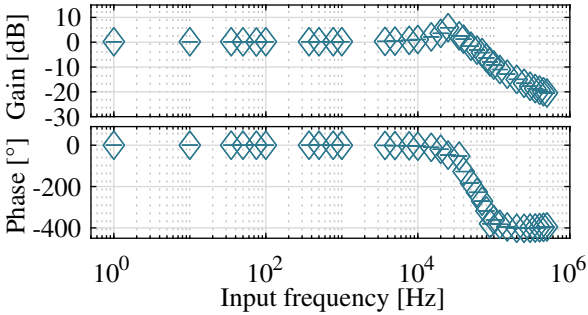


**Figure 6.8:** Frequency response of the amplifier for unity gain.

A sample trace of the output of the TIA is shown in figure 6.9 a) for an input current of ±200 nA. As already discussed in section 6.1.2, the output is quite noisy. Noticeable is the quite large output offset, which is mainly due to the

unsymmetric behavior of the amplification stage. The frequency response of the TIA is depicted in figure 6.9 b). As designed, it shows no peaking and a bandwidth of 10 kHz. The I-U transimpedance gain referenced to 1 Ω is at most 110 dBΩ. This is 10 dBΩ more than expected from using a feedback resistance of only 70 kΩ. This is most likely caused by the large output offset voltage, which causes a voltage between the input nodes of $U_{out}/A_{OL}$. This voltage will then contribute to the incoming current through the feedback as well. Still, this circuit is able to achieve a gain of at least 96 dBΩ at a bandwidth of 10 kHz.

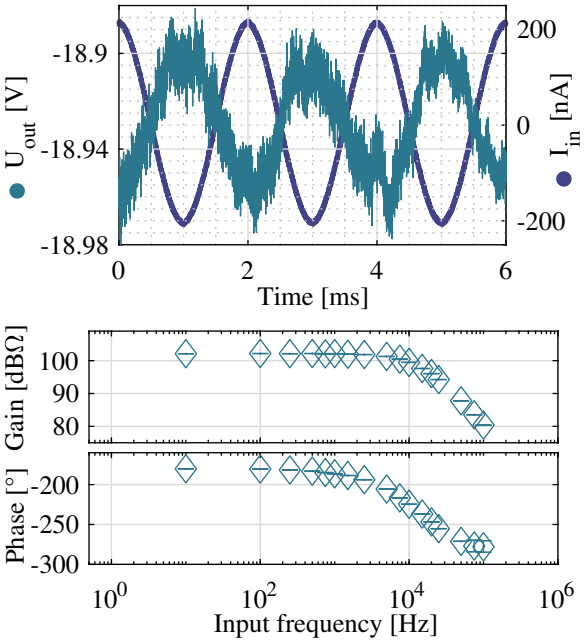


**Figure 6.9:** a) Sample trace of the TIA for an input current of ±200 nA. b) Frequency response of the TIA.

### 6.2.4 CSA based on an LTPS process

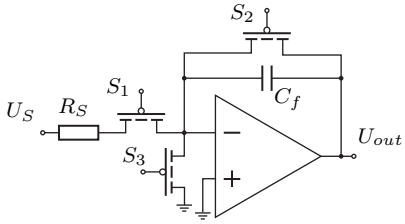


**Figure 6.10:** Schematic of the CSA circuit.

The TIA presented in the previous section has two drawbacks. One is the large output offset and the other is the fixed transimpedance gain. Both issues can be solved by using for example a charge sensitive amplifier (CSA) [193–196]. This switched capacitor circuit is depicted in figure 6.10 and relies on sampling the input current on a capacitance during one clock cycle $\phi_1$ and reading it at the start of the next cycle $\phi_2$.

The charge is sampled onto the capacitance $C_f = 0.4$ pF in the feedback path of the amplifier. During $\phi_2$ the switch $S_2$ is closed such that the amplifier is configured as a voltage follower. Also switch $S_3$ is being closed in this cycle. Hence, the amplifiers output will only show the input offset voltage $V_{OS}$. Consequently $C_f$ will be charged to this offset voltage as well.

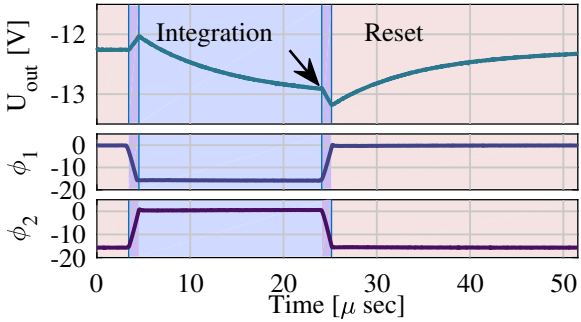


**Figure 6.11:** Measurement of the output signal $U_{out}$ of the CSA. Below are the voltages applied to the switches $S_1$, $S_2$ and $S_3$ are shown. The arrow indicates the point, which is used for all further evaluations.

By opening the switches $S_2$ and $S_3$ during the clock cycle $\phi_1$ and closing $S_1$, the inflowing charge gets sampled onto the capacitance $C_f$. Additionally the input offset voltage is again sampled onto $C_f$, but this time with a negative sign. It is therefore subtracted from the overall output swing, which is given by

$$U_{out} = I_{in} \cdot \tau_s \cdot \frac{1}{2\pi \cdot \left(C_f + \frac{C_f + C_i}{A_{OL}}\right)}. \tag{6.8}$$

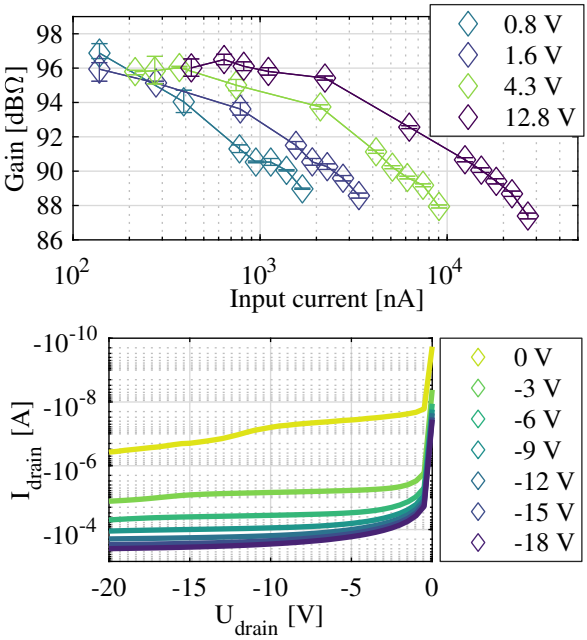


**Figure 6.12:** a) $I-U$ gain depending on the presumably incoming current, which is calculated from the the value of the applied voltage $U_s$ and the utilized resistor $R_s$. b) Output characteristics of the TFTs for different applied gate voltages.

A measurement of the output signal as function of time is shown in figure 6.11. The arrow indicates the end of the sample phase $\phi_1$. This point was also taken for all the evaluation. In practice a peak detector circuit would hold this point for further data acquisition electronics while the CSA continues by resetting $C_f$. For all measurements the resetting time $\tau_r$ was kept four times as long as the sample time $\tau_s$.
A voltage generator and a resistor were used as a current source. This has an immediate drawback. A perfect current source delivers a certain fixed current and as much voltage as is needed to drive this current. This is obviously not the case here. Additionally to the problematic current source has a TFT operated as a switch a nonideal conduction behavior as was explained in section 6.2.1. The output characteristics of the employed TFTs can be seen in figure 6.12, where the drain current is plotted as function of the drain/source voltage for different gate voltages. For our current source, which is rather a voltage source, one does not know the exact current flowing through the resistor $R_s$ and $S_1$ to the inverting input node due to the non-ohmic output characteristic of the TFTs for large voltages across the drain/source nodes. In figure 6.13 a) the gain of the CSA is plotted as function of the presumably present input current. The current was varied by using different values of $R_s$ and keeping for each measurement series $U_s$ at the value indicated in the legend. One can see, that for supposedly same current values, different gains are achieved since the TFT would be saturated at that drain source voltage. What one would need to do is to deconvolute the measured gain from the output characteristic of the $S_1$ TFT. This would require a precise SPICE model of the amplifier and the TFTs, which is not feasible due to the huge process fluctuations.
The gain can be changed by varying the sample time according to equation (6.8). The upper limit is given by the bandwidth of the amplifier. This behavior is depicted in figure 6.13 a). The frequency response of the CSA as function of the input frequency for a clock frequency of 5 kHz is depicted in figure 6.13 b). Although the CSA works as expected it becomes evident that such a circuit is more suited for detecting the mere presence of a signal rather than its' exact amplitude. The main problem is the non-ideal conduction behavior of the input switch $S_1$, which could in principle be improved to an ohmic behavior by using several TFTs in a row, such that across all TFTs only a small voltage drop occurs and they all work in the ohmic regime. This is exactly what is made use of in the Ulm TIA, where a so called pseudoresistor based on appropriately biased transistors is employed as a feedback resistor.

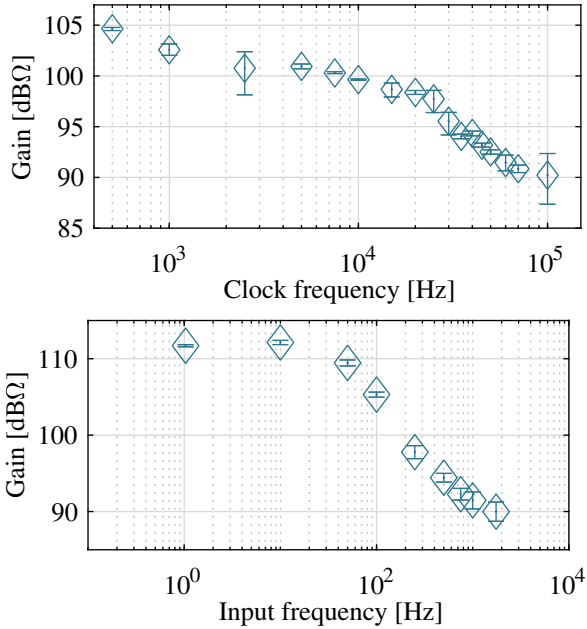


**Figure 6.13:** a) $I-U$ gain for different clock frequencies. b) $I-U$ gain for different input frequencies for a clock frequency of 5 kHz.

## 6.3 Solid state TIAs

Several attempts were made to utilize discrete TIAs in a die format. In the following the interconnect technology will be summarized and the circuit of the LTC6252 TIA will be explained.

### 6.3.1 ACF bonding

The Ulm TIA as well as the flat ribbon cables visible in figure 5.1 were attached to the glass substrates via anisotropic conductive film (ACF) bonding. ACF consists of a curable glue in which small spheres made from gold are immersed. The amount of particles is chosen such that electrical contact can only be

achieved in the vertical direction between e.g. the bumps of a die and the metallic footprint on the glass substrate. Yet in the horizontal direction no electrical contact is achieved [197]. The gold particles are often wrapped in a plastic film, which cracks open under pressure. This ensures once more that no electrical contact in the horizontal direction is accomplished. There is a huge variety of different ACF materials available, which differ in process temperature and pressure and which are suited for chip on glass, flex on glass, chip on board bonding for example. For our purpose, a strip of ACF is precured at a specified temperature and pressure before the chip is placed on the ACF with a flip-chip bonder. The chip is first aligned to the landpattern on the substrate, then the flip-chip bonder applies another time pressure and heat to the ACF and thereby attaches the chip to the glass substrate. In figure 6.14 a picture of the

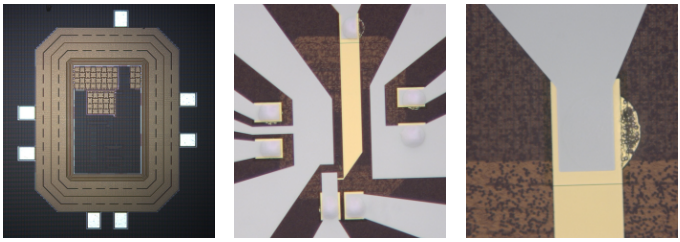

**Figure 6.14:** a) Microscope image of the Ulm TIA, taken from [74]. The area underneath the active electronics (the dark shaded region in the middle) has dimensions of $300 \times 480$ $\mu$m. b) Picture of the footprint on glass with the attached TIA. c) Closer view on one of the bumps.

bottom of the Ulm TIA is shown (taken from [74]), followed by a microscope image from below the glass substrate with the metallic footprit as well as the ACF bonded chip visible. The yellowish slab in the middle is another metallic layer, which forms a small capacitor between the inverting input node and the output node. This ensures a proper frequency compensation of the TIA [74]. A closer view on one of the bumps is shown on the right, where also the gold particles can be observed. Originally, the chip itself had only pads underneath, which were intended for wire bonding. In order to obtain bumps a gold wire was bonded to the pads and snipped off. By measuring the frequency response of the amplifier, the quality of the ACF interconnect could be verified. On chips intended for ACF bonding certain nodes, like the ground for example,

appear several times. This allows then to measure the resistance directly from one bump to the next one. This was not the case for the Ulm TIA.

### 6.3.2 LTC6252

The circuit shown in figure 6.15 was used for the measurement of fast arriving charges in chapter 2. One input node is connected to the amplifier configured as the known TIA via a lowpass filter. The other input is connected to a dummy electrode and acts as a reference. In this way noise occurring on both electrodes is subtracted at the amplifier and additionally suppressed by the common mode rejection ratio of the amplifier. A lower gain was chosen for the TIA to achieve a higher bandwidth, of course on the expense of noise and gain. The output signal of the TIA is then further amplified with an inverting amplifier. This circuit achieves a bandwidth of 2.5 MHz at a gain of 140 dBΩ and a current noise density of $1.0 \cdot 10^{-12}$ A/$\sqrt{\text{Hz}}$ with the cell attached. The convenience of this circuit lies in its' small low frequency noise, which is suppressed by the dummy electrode configuration.

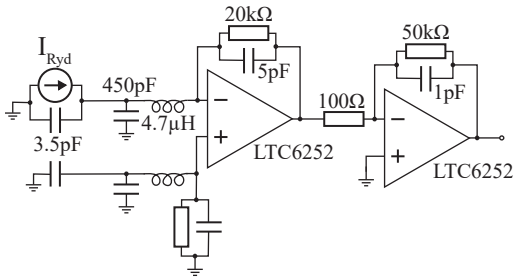


**Figure 6.15:** Schematic of the LTC6252 TIA circuit.

## 6.4 Conclusion

Different methods of implementing a transimpedance amplifier in an integrated way have been presented. Two main noise sources can be identified. The main contribution is caused by large input capacities. These can be minimized by placing the amplifier as close as possible to the current source. The remaining noise is caused by insufficient shielding of the electrodes. Here some development is still required. For high frequency noise the shielding has to be connected to the reference plane with a small resistance and inductance. Otherwise, the noise picked up on the shielding is out of phase with the reference plane and hence appears again. In the best case, the shielding has no gaps. This depends a lot on whether the cell needs any other things attached, such as tubes for filling with a gas for example.
The approaches that were investigated show very different properties concerning bandwidth and gain. The intrinsic noise of the amplifier is then for all the cases mainly given by the transimpedance gain. Depending on the exact application and its' demands on bandwidth and amplification the whole system has to be kept in mind. Therefore one needs to decide, whether an extremely low noise amplification is actually necessary, since an integration of the TIA into the cell can be a challenge. The implementation of different TIAs has been developed and demonstrated for a broad range of demands and for different overall circumstances.

# Technology readiness level 4

**"Component and/or breadboard functional verification in laboratory environment:** *A laboratory breadboard model of the element is integrated to establish that the "pieces" will work together to demonstrate the basic functional performance of the element. The verification is "low fidelity" compared to the eventual system, and is limited to laboratory environment [2]."*

One question that remains is certainly: What are the next necessary achievements that need to be accomplished to reach the next level of technological maturity?
In terms of basic physics some parts of the collisional processes is so far not sufficiently understood. It is indeed not well understood why only about 1% of the collisions actually lead to an ionization of the Rydberg excited atom. That means that further investigations on the Rb system are still required in order to achieve a better estimate of the efficiency of the gas sensor. This is also important with regard to the different decay mechanism in NO, which decays also via predissociation. Comparable to detectors based on chemiluminescence these collisional processes might in the end limit the sensor's sensitivity. Therefore a detailed understanding is necessary and might also open new paths to improve the detection efficiency further.
Based on the experimental results and the derived estimations, it is certainly worth building an apparatus tailored to the sensing of NO. This apparatus is currently being planned. It involves cw laser excitation, a glass cell in a through-flow configuration and will also include a new generation of the Ulm TIA.
The aim will be to build a millimeter sized glass cell, which decreases the required breath gas volume. The new TIA will feature an even lower noise level and its gain might in the future even be controllable via an digital command. This will then circumvent the encountered noise problems during the present realization.
The 3-photon excitation involves a laser at 226 nm wavelength exciting the

transition from the X $^2\Pi_{1/2}$ to the A $^2\Sigma$ state, similar to the transition investigated here. However, the next transition will be to the H $^2\Sigma^+$ state, coupled with a 540 nm laser. The Rydberg state is then reached using a laser with a wavelength of 833 nm.
This scheme has the advantage of being even more selective. Additionally, the photoionization due to the 328 nm laser can be avoided. A signal due to charge creation by photoionization by the 226 nm laser can be canceled using Lock-in detection by amplitude modulating the 833 nm laser for example. Furthermore, the 328 nm laser as cw laser would not have sufficient power to efficiently excite the Rydberg state, whereas with a 540 nm fiber laser and a tapered amplifier boosted 833 nm diode laser there is certainly sufficient power available.
The first goals with the new laser setup will be to measure the groundstate spectrum of NO via 2-photon photoionization or in a REMPI configuration. This has never been done before using such narrow band cw lasers. Then the Rydberg line needs to be found.
Maybe it is worth switching from the rotational groundstate to a higher rotational state, which is higher populated at room temperature. This would produce a more complicated and less coupled Rydberg spectrum, but might still yield more population in the excited state. The influence of pressure, concentration and type of background gas is then the final investigation, which paths the way to the next technology readiness level.
Eventually, the measurement of the NO concentration in a real breath gas sample will be the proof that the Rydberg based gas sensor technology is sufficiently high evolved to be on TRL 4. This will imply that the technology is ready to be applied in medical research.

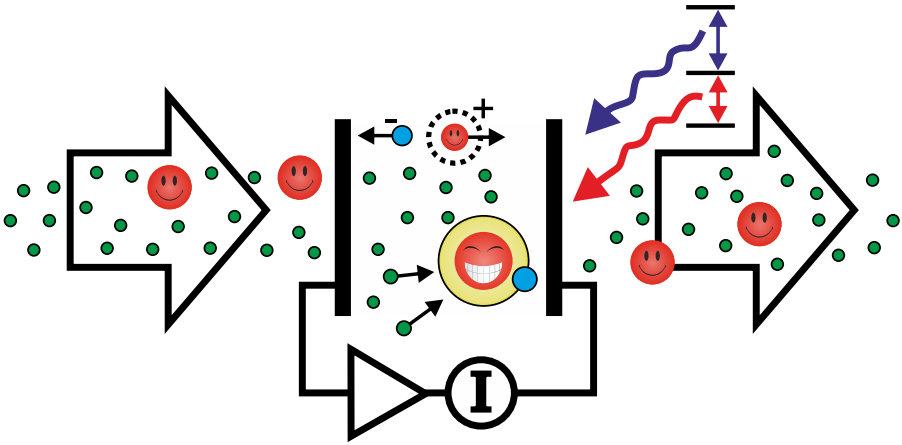
-
+
I

# Bibliography


[1] Roeder, S., Der richtige Riecher für exakte Diagnostik - Präzisionsspektrokopie misst winzige Stickoxid-Gasmenegen dank Rydberg-Anregung, *Forschung Leben* (2018).

[2] ISO Central Secretary. Space systems - Definition of the Technology Readiness Levels (TRLs) and their criteria of assessment. Standard ISO/FDIS 16290:2013, International Organization for Standardization, Geneva, CH, 2013.

[3] Li, W., Mourachko, I., Noel, M.W., and Gallagher, T.F., Millimeter-wave spectroscopy of cold Rb Rydberg atoms in a magneto-optical trap: Quantum defects of the ns, np, and nd series, *Physical Review A: Atomic, Molecular, and Optical Physics* **67**, 052502 (2003).

[4] Gallagher, T.F., *Rydberg atoms*, Cambridge University press.

[5] Olson, R.E., Ionization cross sections for Rydberg-Atom-Rydberg-Atom Collisions, *Physical Review Letters* **43**, 126–129 (1979).

[6] Seaver, M., Chupka, W.A., Colson, S.D., and Gauyacq, D., Double resonance multiphoton ionization studies of high Rydberg states in nitric oxide (NO), *The Journal of Physical Chemistry* **87**, 2226–2231 (1983).

[7] Ebata, T., Anezaki, Y., Fujii, M., Mikami, N., and Ito, M., High Rydberg states of nitric oxide studied by two-color multiphoton spectroscopy, *The Journal of Physical Chemistry* **87**, 4773–4776 (1983).

[8] O'Sullivan, M.S. and Stoicheff, B.P., Scalar polarizabilities and avoided crossings of high Rydberg states in Rb, *Physical Review A: Atomic, Molecular, and Optical Physics* **31**, 2718–2720 (1985).

[9] Li, L., Shi, X., Findley, G., and Evans, C., Dopant low-n Rydberg states in CF4 and CH4 near the critical point, *Chemical Physics Letters* **482**, 50–55 (2009).

[10] Komatsu, M., Ebata, T., and Mikami, N., Rotational analysis of n=4–7 Rydberg states of CO observed by ion-dip spectroscopy, *The Journal of Chemical Physics* **99**, 9350–9365 (1993).

[11] Ashfold, M.N.R., Hartree, W.S., Salvato, A.V., Tutcher, B., and Walker, A., A reinvestigation of the Rydberg states of H2S and D2S by two-photon resonant multiphoton ionisation spectroscopy, *Journal of the Chemical Society, Faraday Transactions* **86**, 2027 (1990).

[12] Jungen, C. and Miescher, E., Absorption spectrum of the NO molecule. IX. The structure of the f complexes, the ionization potential of NO, and the quadrupole moment of NO+, *Canadian Journal of Physics* **47**, 1769–1787 (1969).

[13] Schmidt, J., Fiedler, M., Albrecht, R., Djekic, D., Schalberger, P., Baur, H., Löw, R., Fruehauf, N., Pfau, T., Anders, J., Grant, E.R., and Kübler, H., Proof of concept for an optogalvanic gas sensor for NO based on Rydberg excitations, *Applied Physics Letters* **113**, 011113 (2018).

[14] Löw, R., Weimer, H., Nipper, J., Balewski, J.B., Butscher, B., Büchler, H.P., and Pfau, T., An experimental and theoretical guide to strongly interacting Rydberg gases, *Journal of Physics B: Atomic, Molecular and Optical Physics* **45**, 113001 (2012).

[15] Schmidt, J. Generation of non-classical light using ultra-cold Rydberg ensembles. Master's thesis, University of Stuttgart, 2014.

[16] Niemax, K., Spectroscopy using thermionic diode detectors, *Applied Physics B Photophysics and Laser Chemistry* **38**, 147–157 (1985).

[17] Herrmann, P.P., Schlumpf, N., Telegdi, V.L., and Weis, A., Design, performance, and theory of long thermionic diodes, *Review of Scientific Instruments* **62**, 609–623 (1991).

[18] Fleischhauer, M., Imamoglu, A., and Marangos, J.P., Electromagnetically induced transparency: Optics in coherent media, *Reviews of Modern Physics* **77**, 633 (2005).

[19] Barredo, D., Kübler, H., Daschner, R., Löw, R., and Pfau, T., Electrical read out for coherent phenomena involving Rydberg atoms in thermal vapor cells, *Phys. Rev. Lett.* **110**, 123002 (2013).

[20] Daschner, R. *Addressable rubidium vapor cells for optical and electrical read-out of Rydberg excitations.* PhD thesis.

[21] Ripka, F., Kübler, H., Löw, R., and Pfau, T., A room-temperature single-photon source based on strongly interacting Rydberg atoms, *Science* **362**, 446–449 (2018).

[22] Gorniaczyk, H., Tresp, C., Schmidt, J., Fedder, H., and Hofferberth, S., Single-Photon Transistor Mediated by Interstate Rydberg Interactions, *Phys. Rev. Lett.* **113**, 053601 (2014).

[23] Firstenberg, O., Adams, C.S., and Hofferberth, S., Nonlinear quantum optics mediated by Rydberg interactions, *Journal of Physics B: Atomic, Molecular and Optical Physics* **49**, 152003 (2016).

[24] Sedlacek, J., Schwettmann, A., Kübler, H., Löw, R., Pfau, T., and Shaffer, J.P., Microwave electrometry with Rydberg atoms in a vapour cell using bright atomic resonances, *Nature Physics* **8**, 819–824 (2012).

[25] Riegel, J., Exhaust gas sensors for automotive emission control, *Solid State Ionics* **152-153**, 783–800 (2002).

[26] Yang, R. and Chen, R., Real-Time Plasma Process Condition Sensing and Abnormal Process Detection, *Sensors* **10**, 5703–5723 (2010).

[27] Wilson, A., Diverse Applications of Electronic-Nose Technologies in Agriculture and Forestry, *Sensors* **13**, 2295–2348 (2013).

[28] Li, S., Simonian, A., and Chin, B.A., Sensors for Agriculture and the Food Industry, *The Electrochemical Society Interface* **19**, 41–46 (2010).

[29] Buszewski, B., Kesy, M., Ligor, T., and Amann, A., Human exhaled air analytics: biomarkers of diseases, *Biomedical Chromatography* **21**, 553–566 (2007).

[30] Ishihara, T. and Matsubara, S., *Journal of Electroceramics* **2**, 215–228 (1998).

[31] Wang, C., Yin, L., Zhang, L., Xiang, D., and Gao, R., Metal Oxide Gas Sensors: Sensitivity and Influencing Factors, *Sensors* **10**, 2088–2106 (2010).

[32] Umar, A., *Metal Oxide Nanostructures and Their Applications*, Amer Scientific Pub.

[33] Fanget, S., Hentz, S., Puget, P., Arcamone, J., Matheron, M., Colinet, E., Andreucci, P., Duraffourg, L., Myers, E., and Roukes, M., Gas sensors based on gravimetric detection—A review, *Sensors and Actuators B: Chemical* **160**, 804–821 (2011).

[34] Kim, S., Lee, Y.I., Choi, Y.M., Lim, H.R., Lim, J.H., Myung, N.V., and Choa, Y.H., Thermochemical hydrogen sensor based on chalcogenide nanowire arrays, *Nanotechnology* **26**, 145503 (2015).

[35] Hodgkinson, J. and Tatam, R.P., Optical gas sensing: a review, *Measurement Science and Technology* **24**, 012004 (2012).

[36] Lewicki, R., Doty, J.H., Curl, R.F., Tittel, F.K., and Wysocki, G., Ultrasensitive detection of nitric oxide at 5.33  m by using external cavity quantum cascade laser-based Faraday rotation spectroscopy, *Proceedings of the National Academy of Sciences* **106**, 12587–12592 (2009).

[37] Heinrich, K., Fritsch, T., Hering, P., and Mürtz, M., Infrared laser-spectroscopic analysis of 14NO and 15NO in human breath, *Applied Physics B* **95**, 281–286 (2009).

[38] Dooly, G., Fitzpatrick, C., and Lewis, E., Deep UV based DOAS system for the monitoring of nitric oxide using ratiometric separation techniques, *Sensors and Actuators B: Chemical* **134**, 317–323 (2008).

[39] McKeachie, J.R., van der Veer, W.E., Short, L.C., Garnica, R.M., Appel, M.F., and Benter, T., Selective ultra-trace detection of NO and NO2 in complex gas mixtures using broad-bandwidth REMPI mass spectrometry, *The Analyst* **126**, 1221–1228 (2001).

[40] *The PID Handbook-Theory and Applications of Direct-Reading Photoionization Detectors*, RAE Systems Inc.

[41] Ménil, F., Coillard, V., and Lucat, C., Critical review of nitrogen monoxide sensors for exhaust gases of lean burn engines, *Sensors and Actuators B: Chemical* **67**, 1–23 (2000).

[42] Bakker, E., Electrochemical Sensors, *Analytical Chemistry* **76**, 3285–3298 (2004).

[43] Stetter, J.R. and Li, J., Amperometric Gas SensorsA Review, *Chemical Reviews* **108**, 352–366 (2008).

[44] Somov, S., Reinhardt, G., Guth, U., and Göpel, W., Gas analysis with arrays of solid state electrochemical sensors: implications to monitor HCs and NOx in exhausts, *Sensors and Actuators B: Chemical* **36**, 409–418 (1996).

[45] Jensen, G.C., Zheng, Z., and Meyerhoff, M.E., Amperometric Nitric Oxide Sensors with Enhanced Selectivity Over Carbon Monoxide via Platinum Oxide Formation Under Alkaline Conditions, *Analytical Chemistry* **85**, 10057–10061 (2013).

[46] Akbar, S., Dutta, P., and Lee, C., High-Temperature Ceramic Gas Sensors: A Review, *International Journal of Applied Ceramic Technology* **3**, 302–311 (2006).

[47] Maniscalco, M., Vitale, C., Vatrella, A., Molino, A., Bianco, A., and Mazzarella, G., Fractional exhaled nitric oxide-measuring devices: technology update, *Medical Devices: Evidence and Research*, 151 (2016).

[48] Bateman, R.M., Ellis, C.G., and Freeman, D.J., Optimization of Nitric Oxide Chemiluminescence Operating Conditions for Measurement of Plasma Nitrite and Nitrate, *Clinical Chemistry* **48**, 570–573 (2002).

[49] Bates, J.N., Nitric oxide measurement by chemiluminescence detection, *Neuroprotocols* **1**, 141 – 149 (1992).

[50] Awad, H., Khamis, M.M., and El-Aneed, A., Mass Spectrometry, Review of the Basics: Ionization, *Applied Spectroscopy Reviews* **50**, 158–175 (2014).

[51] Glish, G.L. and Vachet, R.W., The basics of mass spectrometry in the twenty-first century, *Nature Reviews Drug Discovery* **2**, 140–150 (2003).

[52] ATS/ERS Recommendations for Standardized Procedures for the Online and Offline Measurement of Exhaled Lower Respiratory Nitric Oxide and Nasal Nitric Oxide, 2005, *American Journal of Respiratory and Critical Care Medicine* **171**, 912–930 (2005).

[53] Mazzatenta, A., Giulio, C.D., and Pokorski, M., Pathologies currently identified by exhaled biomarkers, *Respiratory Physiology & Neurobiology* **187**, 128–134 (2013).

[54] Risby, T. and Solga, S., Current status of clinical breath analysis, *Applied Physics B* **85**, 421–426 (2006).

[55] Furchgott, R.F. and Zawadzki, J.V., The obligatory role of endothelial cells in the relaxation of arterial smooth muscle by acetylcholine, *Nature* **288**, 373–376 (1980).

[56] Ignarro, L., Buga, G., Wood, K., Byrns, R., and Chaudhuri, G., Endothelium-derived relaxing factor produced and released from artery and vein is nitric oxide, *Proc Natl Acad Sci USA* **84**, 9265–9269 (1987).

[57] Moncada, S. and Higgs, E.A., The discovery of nitric oxide and its role in vascular biology, *British Journal of Pharmacology* **147**, S193–S201 (2006).

[58] Thomas, D.D., Ridnour, L.A., Isenberg, J.S., Flores-Santana, W., Switzer, C.H., Donzelli, S., Hussain, P., Vecoli, C., Paolocci, N., Ambs, S., Colton, C.A., Harris, C.C., Roberts, D.D., and Wink, D.A., The chemical biology of nitric oxide: Implications in cellular signaling, *Free Radical Biology and Medicine* **45**, 18–31 (2008).

[59] Yun, H., Dawson, V., and Dawson, T., Neurobiology of nitric oxide, *Crit Rev Neurobiol* **10**, 291–316 (1996).

[60] Alving, K. Weitzberg, E.L.J., Increased amount of nitric oxide in exhaled air of asthmatics, *Eur Respir J.* **6**, 1368–1370 (1993).

[61] Haklar, G., Sayin-Özveri, E., Yüksel, M., Aktan, A.O., and Yalcin, A., Different kinds of reactive oxygen and nitrogen species were detected in colon and breast tumors, *Cancer Letters* **165**, 219 – 224 (2001).

[62] Connelly, S.T., Macabeo-Ong, M., Dekker, N., Jordan, R.C., and Schmidt, B.L., Increased nitric oxide levels and iNOS over-expression in oral squamous cell carcinoma, *Oral Oncology* **41**, 261–267 (2005).

[63] Hickok, J. and Thomas, D., Nitric Oxide and Cancer Therapy: The Emperor has NO Clothes, *Current Pharmaceutical Design* **16**, 381–391 (2010).

[64] Choudhari, S.K., Sridharan, G., Gadbail, A., and Poornima, V., Nitric oxide and oral cancer: A review, *Oral Oncology* **48**, 475 – 483 (2012).

[65] Jorissen, M., Lefevere, L., and Willems, T., Nasal nitric oxide, *Allergy* **56**, 1026–1033 (2001).

[66] Mur, L.A., Mandon, J., Cristescu, S.M., Harren, F.J., and Prats, E., Methods of nitric oxide detection in plants: A commentary, *Plant Science* **181**, 509–519 (2011).

[67] Cristescu, S.M., Marchenko, D., Mandon, J., Hebelstrup, K., Griffith, G.W., Mur, L.A.J., and Harren, F.J.M., Spectroscopic monitoring of NO traces in plants and human breath: applications and perspectives, *Applied Physics B* **110**, 203–211 (2012).

[68] Waller, L.A., Estimate suggests many infant deaths in sub-Saharan Africa attributable to air pollution, *Nature* **559**, 188–189 (2018).

[69] Heft-Neal, S., Burney, J., Bendavid, E., and Burke, M., Robust relationship between air quality and infant mortality in Africa, *Nature* **559**, 254–258 (2018).

[70] Exhaust Aftertreatment - BlueTEC with AdBlue - System Description of Engine 642.8. Technical report, Daimler AG, 70546 Stuttgart, 2009.

[71] Schwarzer, C.M., Wir Selbstvergifter, *Zeit Online* (2018).

[72] Schmidt, J., Schalberger, P., Baur, H., Löw, R., Pfau, T., Kübler, H., and Fruehauf, N., A transimpedance amplifier based on an LTPS process operated in alkali vapor for the measurement of an ionization current, (2018).

[73] Michaud, S., Optogalvanic gas sensor based on Rydberg excitation shows promise for NO detection, *Scilight* **2018**, 270010 (2018).

[74] Djekic, D., Fantner, G., Behrends, J., Lips, K., Ortmanns, M., and Anders, J., *A transimpedance amplifier using a widely tunable PVT-independent pseudo-resistor for high-performance current sensing applications*, in *ESSCIRC 2017 - 43rd IEEE European Solid State Circuits Conference*, 79-82.

[75] Beringer, R., Rawson, E.B., and Henry, A.F., Microwave Resonance in Nitric Oxide: Lambda Doubling and Hyperfine Structure, *Physical Review* **94**, 343–349 (1954).

[76] Rudolph, H., McKoy, V., and Dixit, S.N., Rotational branching ratios at low photoelectron energies in resonant enhanced multiphoton ionization of NO, *The Journal of Chemical Physics* **90**, 2570–2574 (1989).

[77] Reiser, G. and Mueller-Dethlefs, K., Rotationally resolved (zero kinetic energy) photoelectron spectroscopy of nitric oxide, *The Journal of Physical Chemistry* **96**, 9–12 (1992).

[78] Sándorfy, C., editor, *The Role of Rydberg States in Spectroscopy and Photochemistry*, Springer Netherlands.

[79] Herzberg, G., *Molecular Spectra and Molecular Structure: Spectra of diatomic molecules*, number Bd. 1 in Molecular Spectra and Molecular Structure, Van Nostrand.

[80] Bixon, M. and Jortner, J., The dynamics of predissociating high Rydberg states of NO, *The Journal of Chemical Physics* **105**, 1363–1382 (1996).

[81] Vrakking, M.J.J. and Lee, Y.T., Enhancements in the lifetimes of NO Rydberg states in dc electric fields: Implications for zero-electron-kinetic-energy photoelectron spectroscopy experiments, *Physical Review A* **51**, R894–R897 (1995).

[82] Miescher, E., Absorption spectrum of the NO molecule, *Journal of Molecular Spectroscopy* **20**, 130–140 (1966).

[83] Jungen, C. and Miescher, E., Absorption spectrum of the NO molecule. IX. The structure of the f complexes, the ionization potential of NO, and the quadrupole moment of $NO^+$, *Canadian Journal of Physics* **47**, 1769–1787 (2011).

[84] Jungen, C., Rydberg Series in the NO Spectrum: An Interpretation of Quantum Defects and Intensities in the s and d Series, *The Journal of Chemical Physics* **53**, 4168–4182 (2003).

[85] Saquet, N., Morrison, J.P., and Grant, E., Recombinative dissociation and the evolution of a molecular ultracold plasma, *Journal of Physics B: Atomic, Molecular and Optical Physics* **45**, 175302 (2012).

[86] Haenel, R., Schulz-Weiling, M., Sous, J., Sadeghi, H., Aghigh, M., Melo, L., Keller, J.S., and Grant, E.R., Arrested relaxation in an isolated molecular ultracold plasma, *Physical Review A* **96**, 023613 (2017).

[87] Sadeghi, H., Kruyen, A., Hung, J., Gurian, J.H., Morrison, J.P., Schulz-Weiling, M., Saquet, N., Rennick, C.J., and Grant, E.R., Dissociation and the Development of Spatial Correlation in a Molecular Ultracold Plasma, *Physical Review Letters* **112**, 075001 (2014).

[88] Sadeghi, H., Schulz-Weiling, M., Morrison, J.P., Yiu, J.C.H., Saquet, N., Rennick, C.J., and Grant, E.R., Molecular ion–electron recombination in an expanding ultracold neutral plasma of $NO^+$, *Phys. Chem. Chem. Phys.* **13**, 18872 (2011).

[89] Morrison, J.P., Rennick, C.J., Keller, J.S., and Grant, E.R., Evolution from a Molecular Rydberg Gas to an Ultracold Plasma in a Seeded Supersonic Expansion of NO, *Physical Review Letters* **101**, 205005 (2008).

[90] Schulz-Weiling, M. *Ultracold Molecular Plasma.* PhD thesis.

[91] Schott Technical Glass Solutions GmbH, Schott Borofloat 33, *Schott, Jena, Germany* (2014).

[92] McCleverty, J.A., Reactions of nitric oxide coordinated to transition metals, *Chemical Reviews* **79**, 53–76 (1979).

[93] Eisenberg, R. and Meyer, C.D., Coordination chemistry of nitric oxide, *Accounts of Chemical Research* **8**, 26–34 (1975).

[94] Ford, P.C. and Lorkovic, I.M., Mechanistic Aspects of the Reactions of Nitric Oxide with Transition-Metal Complexes, *Chemical Reviews* **102**, 993–1018 (2002).

[95] Schmick, H.D. and Wassmuth, H.W., Adsorption, desorption and reaction kinetics of nitric oxide on a stepped pd(111) surface, *Surface Science* **123**, 471 – 490 (1982).

[96] Pontrelli, G. and de Monte, F., Mass diffusion through two-layer porous media: an application to the drug-eluting stent, *International Journal of Heat and Mass Transfer* **50**, 3658 – 3669 (2007).

[97] Garnica, R.M., Appel, M.F., Eagan, L., McKeachie, J.R., and Benter, T., A REMPI Method for the Ultrasensitive Detection of NO and NO2Using Atmospheric Pressure Laser Ionization Mass Spectrometry, *Analytical Chemistry* **72**, 5639–5646 (2000).

[98] Hall, R.T. and Dowling, J.M., Pure Rotational Spectrum of Nitric Oxide, *The Journal of Chemical Physics* **45**, 1899–1903 (1966).

[99] Mollet, S. *Rydberg states and photoionisation dynamics of NO and $Cl_2$.* PhD thesis.

[100] Steck, D.A., Rubidium 85 D Line Data, *available online at http://steck.us/alkalidata (revision 2.1.6, 20 September 2013).*

[101] Safarian, J. and Engh, T.A., Vacuum Evaporation of Pure Metals, *Metallurgical and Materials Transactions A* **44**, 747–753 (2012).

[102] Ishikawa, K. and Yabuzaki, T., Diffusion coefficient and sublevel coherence of Rb atoms inN2buffer gas, *Physical Review A* **62** (2000).

[103] Sushkov, A.O. and Budker, D., Production of long-lived atomic vapor inside high-density buffer gas, *Physical Review A* **77** (2008).

[104] R. Integrated and Time-Resolved Measurements of Collisional Energy Transfer in Rubidium P-States. mathesis, Universität Stuttgart, December 2017.

[105] Hall, T. and Mee, C., The Work Function of Rubidium, *Phys. Stat. Sol.* **21**, 109 (1974).

[106] Petitjean, L., Gounand, F., and Fournier, P.R., Thermal-energy collisions of rubidium Rydberg states with $N_2$ molecules, *Physical Review A: Atomic, Molecular, and Optical Physics* **30**, 736–742 (1984).

[107] Hahn, Y., Thermal collisions of high Rydberg atoms with neutral particles. I. General theory and modified impulse approximation, *Journal of Physics B: Atomic and Molecular Physics* **14**, 985 (1981).

[108] Thompson, D.C., Weinberger, E., Xu, G.X., and Stoicheff, B.P., Frequency shifts and line broadening in collisions between Rydberg and ground-state alkali-metal atoms, *Physical Review A: Atomic, Molecular, and Optical Physics* **35**, 690–700 (1987).

[109] Huber, B., Baluktsian, T., Schlagmüller, M., Kölle, A., Kübler, H., Löw, R., and Pfau, T., GHz Rabi flopping to Rydberg states in hot atomic vapor cells, *Phys. Rev. Lett.* **107**, 243001 (2011).

[110] Schmieg, R. Setup and Characterization of a Laser Amplifier for Rydberg Excitation in thermal Rb Atoms. mathesis, Universität Stuttgart, December 2016.

[111] Graeme, J., *Photodiode Amplifiers: OP AMP Solutions*, Gain technology, McGraw-Hill Education.

[112] Demtröder, W., *Laserspektroskopie: Grundlagen und Techniken*, Springer Verlag.

[113] Weller, D., Urvoy, A., Rico, A., Löw, R., and Kübler, H., Charge-induced optical bistability in thermal Rydberg vapor, *Physical Review A* **94** (2016).

[114] Grimmel, J., Mack, M., Karlewski, F., Jessen, F., Reinschmidt, M., Sándor, N., and Fortágh, J., Measurement and numerical calculation of Rubidium Rydberg Stark spectra, *New Journal of Physics* **17**, 053005 (2015).

[115] Kashtanov, P.V., Myasnikov, M.I., and Smirnov, B.M., Ineleastic Electron collisions with Rydberg Atoms, *Journal of experimental and theoretical physics* **108**, 18–26 (2009).

[116] Beterov, I.I., Tretyakov, D.B., Ryabtsev, I.I., Entin, V.M., Ekers, A., and Bezuglov, N.N., Ionization of Rydberg atoms by blackbody radiation, *N. Journ. Phys.* **11**, 013052 (2009).

[117] Ovsiannikov, V.D., Glukhov, I.L., and Nekipelov, E.A., Radiative lifetime and photoionization cross-section for Rydberg states in alkali-metal atoms, *Optics and Spectroscopy* **111**, 25–33 (2011).

[118] Kleinbach, K., Engel, F., Dieterle, T., Löw, R., Pfau, T., and Meinert, F., Ionic Impurity in a Bose-Einstein Condensate at Submicrokelvin Temperatures, *Physical Review Letters* **120** (2018).

[119] Horsley, A. *High resolution field imaging with atomic vapor cells.* PhD thesis.

[120] Petitjean, L., Gounand, F., and Fournier, P.R., Depopulation of rubidium Rydberg states by CO molecules: An experimental and theoretical study, *Physical Review A: Atomic, Molecular, and Optical Physics* **30**, 71–81 (1984).

[121] Petitjean, L., Gounand, F., and Fournier, P.R., Collisions of rubidium Rydberg-state atoms with ammonia, *Physical Review A: Atomic, Molecular, and Optical Physics* **33**, 143–147 (1986).

[122] Weller, L., Bettles, R.J., Siddons, P., Adams, C.S., and Hughes, I.G., Absolute absorption on the rubidium D1line including resonant dipole–dipole interactions, *Journal of Physics B: Atomic, Molecular and Optical Physics* **44**, 195006 (2011).

[123] Rotondaro, M.D. and Perram, G.P., Collisional broadening and shift of the rubidium D1 and D2 lines () by rare gases, H2, D2, N2, CH4 and CF4, *Journal of Quantitative Spectroscopy and Radiative Transfer* **57**, 497–507 (1997).

[124] Hrycyshyn, E.S. and Krause, L., Inelastic collisions between excited alkali atoms and molecules. VII. Sensitized fluorescence and quenching in mixtures of rubidium with H2, HD, D2, N2, CH4, CD4, C2H4, and C2.H6, *Canadian Journal of Physics* **48**, 2761–2768 (1970).

[125] Amaldi, E. and Segré, E., Effect of Pressure on High Terms of Alkaline Spectra, *Nature* **133**, 141–141 (1934).

[126] Amaldi, E. and Segré, E., Effetto della Pressione Sui Termini Elevati Degli Alcalini, *Il Nuovo Cimento (1924-1942)* **11**, 145 (2008).

[127] Fermi, E., Sopra lo Spostamento per Pressione delle Righe Elevate delle Serie Spettrali, *Il Nuovo Cimento (1924-1942)* **11**, 157 (2008).

[128] Füchtbauer, C. and Gössler, F., Verschiebung und unsymmetrische Verbreiterung von Absorptionslinien durch Fremdgase, *Zeitschrift für Physik* **87**, 89–104 (1934).

[129] Füchtbauer, C., Schulz, P., and Brandt, A.F., Verschiebung von hohen Serienlinien des Natriums und Kaliums durch Fremdgase, Berechnung der Wirkungsquerschnitte von Edelgasen gegen sehr langsame Elektronen, *Zeitschrift für Physik* **90**, 403–415 (1934).

[130] Balewski, J. *A single electron in a Bose-Einstein condensate*. PhD thesis.

[131] Omont, A., On the theory of collisions of atoms in rydberg states with neutral particles, *Journal de Physique* **38**, 1343–1359 (1977).

[132] Weber, K.H. and Niemax, K., Impact broadening and shift of RbnS andnD levels by noble gases, *Zeitschrift für Physik A Atoms and Nuclei* **307**, 13–24 (1982).

[133] Hugon, M., Sayer, B., Fournier, P.R., and Gounand, F., Collisional depopulation of rubidium Rydberg levels by rare gases, *Journal of Physics B: Atomic and Molecular Physics* **15**, 2391 (1982).

[134] Shepard, C.L. and Kocher, C.A., Collisional ionization of high-Rydberg lithium atoms in thermal-energy encounters with rapidly rotating polar molecules, *The Journal of Chemical Physics* **78**, 6620–6628 (1983).

[135] Weber, K.H. and Niemax, K., Self-broadening and shift of Doppler-free two-photon lines of Rb, *Optics Communications* **31**, 52–56 (1979).

[136] Hotop, H. and Niehaus, A., Collisional Ionization of Long-Lived Highly Excited Atoms, *The Journal of Chemical Physics* **47**, 2506–2507 (1967).

[137] Foltz, G.W., Latimer, C.J., Hildebrandt, G.F., Kellert, F.G., Smith, K.A., West, W.P., Dunning, F.B., and Stebbings, R.F., Ionization of xenon atoms in high Rydberg states by collision with molecules, *The Journal of Chemical Physics* **67**, 1352–1359 (1977).

[138] Pfeiffer Vacuum GmbH, Berliner Strasse 43 35614 Asslar, Deutschland. *The Vacuum Technology Book*, April 2013.

[139] Scherschligt, J., Fedchak, J.A., Ahmed, Z., Barker, D.S., Douglass, K., Eckel, S., Hanson, E., Hendricks, J., Klimov, N., Purdy, T., Ricker, J., Singh, R., and Stone, J., Review Article: Quantum-based vacuum metrology at the National Institute of Standards and Technology, *Journal of Vacuum Science & Technology A* **36**, 040801 (2018).

[140] Poulter, K.F., The calibration of vacuum gauges, *Journal of Physics E: Scientific Instruments* **10**, 112–125 (1977).

[141] Newell, D.B., Cabiati, F., Fischer, J., Fujii, K., Karshenboim, S.G., Margolis, H.S., de Mirandés, E., Mohr, P.J., Nez, F., Pachucki, K., Quinn, T.J., Taylor, B.N., Wang, M., Wood, B.M., and Zhang, Z., The CODATA 2017 values of h, e, k, and N A for the revision of the SI, *Metrologia* **55**, L13–L16 (2018).

[142] Egan, P.F., Stone, J.A., Ricker, J.E., Hendricks, J.H., and Strouse, G.F., Cell-based refractometer for pascal realization, *Optics Letters* **42**, 2944 (2017).

[143] Douglass, K.O. and Olson, D.A., Towards a standard for the dynamic measurement of pressure based on laser absorption spectroscopy, *Metrologia* **53**, S96–S106 (2016).

[144] Ahmed, Z., Olson, D., and Douglass, K.O., Precision Spectroscopy to Enable Traceable Dynamic Measurements of Pressure, (2016).

[145] Eckel, S., Barker, D.S., Fedchak, J.A., Klimov, N.N., Norrgard, E., Scherschligt, J., Makrides, C., and Tiesinga, E., Challenges to miniaturizing cold atom technology for deployable vacuum metrology, *Metrologia* **55**, S182–S193 (2018).

[146] Yuan, J.P., Ji, Z.H., Zhao, Y.T., Chang, X.F., Xiao, L.T., and Jia, S.T., Simple, reliable, and nondestructive method for the measurement of vacuum pressure without specialized equipment, *Applied Optics* **52**, 6195 (2013).

[147] Arpornthip, T., Sackett, C.A., and Hughes, K.J., Vacuum-pressure measurement using a magneto-optical trap, *Physical Review A* **85** (2012).

[148] Scherschligt, J., Fedchak, J.A., Barker, D.S., Eckel, S., Klimov, N., Makrides, C., and Tiesinga, E., Development of a new UHV/XHV pressure standard (cold atom vacuum standard), *Metrologia* **54**, S125–S132 (2017).

[149] Baluktsian, M. Superradiance of Rydberg atoms in thermal vapour cells. Master's thesis, University of Stuttgart, 2014.

[150] Sieber, N. Fluorescence spectroscopy of Rydberg atoms in thermal vapor cells in a collision dominated regime. Master's thesis, University of Stuttgart, 2017.

[151] Kitching, J., Chip-scale atomic devices, *Applied Physics Reviews* **5**, 031302 (2018).

[152] Liew, L.A., Knappe, S., Moreland, J., Robinson, H., Hollberg, L., and Kitching, J., Microfabricated alkali atom vapor cells, *Applied Physics Letters* **84**, 2694–2696 (2004).

[153] Lutwak, R., Deng, J., Riley, W., Varghese, M., Leblanc, J., Tepolt, G., Mescher, M., Serkland, D., M Geib, K., and M Peake, G., The chip-scale atomic clock-low-power physics package, (2018).

[154] Pétremand, Y., Affolderbach, C., Straessle, R., Pellaton, M., Briand, D., Mileti, G., and de Rooij, N.F., Microfabricated rubidium vapour cell with a thick glass core for small-scale atomic clock applications, *Journal of Micromechanics and Microengineering* **22**, 025013 (2012).

[155] Vecchio, F., Venkatraman, V., Shea, H., Maeder, T., and Ryser, P., Dispensing and hermetic sealing Rb in a miniature reference cell for integrated atomic clocks, *Procedia Engineering* **5**, 367–370 (2010).

[156] Weller, D., Yilmaz, A., Kübler, H., and Löw, R., High vacuum compatible fiber feedthrough for hot alkali vapor cells, *Applied Optics* **56**, 1546 (2017).

[157] Baluktsian, T., Urban, C., Bublat, T., Giessen, H., Löw, L., and Pfau, T., Fabrication method for microscopic vapor cells for alkali atoms, *Opt. Lett.* **35**, 1950 (2010).

[158] Daschner, R., Kübler, H., Löw, R., Bauer, H., Frühauf, N., and Pfau, T., Triple stack glass-to-glass anodic bonding for optogalvanic spectroscopy cells with electrical feedthroughs, *Appl. Phys. Lett.* **105**, 041107 (2014).

[159] Daschner, R., Ritter, R., Kübler, H., Frühauf, N., Kurz, E., Löw, R., and Pfau, T., Fabrication and characterization of an electrically contacted vapor cell, *Opt. Lett.* **37**, 2271 (2012).

[160] Liew, L.A., Moreland, J., and Gerginov, V., Wafer-level filling of microfabricated atomic vapor cells based on thin-film deposition and photolysis of cesium azide, *Applied Physics Letters* **90**, 114106 (2007).

[161] Huang, H., Yang, L.M., and Liu, J., Direct welding of fused silica with femtosecond fiber laser, (2012).

[162] Haisma, J. and Spierings, G., Contact bonding, including direct-bonding in a historical and recent context of materials science and technology, physics and chemistry, *Materials Science and Engineering: R: Reports* **37**, 1–60 (2002).

[163] Rangsten, P., Quartz-to-Quartz Direct Bonding, *Journal of The Electrochemical Society* **146**, 1104 (1999).

[164] Sekiguchi, N., Sato, T., Ishikawa, K., and Hatakeyama, A., Spectroscopic study of a diffusion-bonded sapphire cell for hot metal vapors, *Applied Optics* **57**, 52 (2017).

[165] Wolffenbuttel, R.F., *Low-temperature silicon wafer-to-wafer bonding using gold at eutectic temperature.*

[166] Wolffenbuttel, R.F., Low-temperature intermediate Au-Si wafer bonding; eutectic or silicide bond, *Sensors and Actuators A: Physical* **62**, 680–686 (1997).

[167] Lee, C., Huang, W.F., and Shie, J.S., Wafer bonding by low-temperature soldering, *Sensors and Actuators A: Physical* **85**, 330–334 (2000).

[168] Yost, F.G., Ultimate strength and morphological structure of eutectic bonds, *Journal of Electronic Materials* **3**, 353–369 (1974).

[169] Pomerantz, D.I., Anodic bonding, *US Patent* **3,397,278** (1968).

[170] Berthold, A., Nicola, L., Sarro, P., and Vellekoop, M., Glass-to-glass anodic bonding with standard IC technology thin films as intermediate layers, *Sensors and Actuators A: Physical* **82**, 224–228 (2000).

[171] Knowles, K.M. and van Helvoort, A.T.J., Anodic bonding, *International Materials Reviews* **51**, 273–311 (2006).

[172] Kim, H.S., Blick, R.H., Kim, D.M., and Eom, C.B., Bonding silicon-on-insulator to glass wafers for integrated bio-electronic circuits, *Applied Physics Letters* **85**, 2370–2372 (2004).

[173] Tingkai, Z., Honghai, Z., Jian, X., Sheng, L., and Zhiyin, G., Study on triple-stack anodic bonding using two electrodes, *Sensors and Actuators, A: Physical* **157**, 168–172 (2010).

[174] Wallis, G. and Pomerantz, D.I., Field assisted glass-metal sealing, *J. Appl. Phys.* **40**, 3946–3949 (1969).

[175] Schjølberg-Henriksen, K., Poppe, E., Moe, S., Storås, P., Taklo, M., Wang, D., and Jakobsen, H., Anodic bonding of glass to aluminium, *Microsyst. Technol.* **12**, 441–449 (2006).

[176] Wei, J., Nai, S.M.L., Wong, C.K., and Lee, L.C., Glass-to-glass anodic bonding process and electrostatic force, *Thin Solid Films* **462-463**, 487–491 (2004).

[177] Albaugh, K.B., Electrode phenomena during anodic bonding of silicon to sodium borosilicate glass, *J. Electrochem. Soc* **138**, 3089–3094 (1991).

[178] Albaugh, K.B. and Rasmussen, D.H., Rate processes during anodic bonding, *J. Am. Ceram. Soc.* **75**, 2644–2648 (1992).

[179] Berthold, A., Nicola, L., Sarro, P., and Vellekoop, M.J., Glass-to-glass anodic bonding with standard IC technology thin films as intermediate layers, *Sensors and Actuators, A: Physical* **82**, 224–228 (2000).

[180] Nitzsche, P., Ion Drift Processes in Pyrex-Type Alkali-Borosilicate Glass during Anodic Bonding, *Journal of The Electrochemical Society* **145**, 1755 (1998).

[181] Hobbs, P.C.D., Photodiode Front Ends, The REAL Story, *Optics & Photonics News* (2001).

[182] Holt, J.C., Hill, W., and Horowitz, P., *The Art of Electronics*, Cambridge University Pr.

[183] Instruments, D. Noise Analysis and Gain Considerations in Selecting the Right Current Preamplifier. techreport Rev. 1 3/87, DL Instruments, 233 Cecil A. Malone Drive, Ithaca, New York 14850.

[184] Instruments, D. *Model 1211 Current Preamplifier*. DL Instruments, 646 76 Road, Brooktondale, NY 14817, USA.

[185] Low Current Measurements. Technical report, Keithley, 2012.

[186] Schalberger, P., Persidis, E., and Fruehauf, N., A five mask CMOS LTPS process with LDD and only one ion implantation step, *Journal of Information Display* **8**, 1–5 (2007).

[187] Schalberger, P., Herrmann, M., Hoehla, S., and Fruehauf, N., 60.4: Distinguished Paper: A Fully Integrated 1 AMOLED Display Using Current Feedback Based on a Five Mask LTPS CMOS Process, *SID Symposium Digest of Technical Papers* **41**, 905–908 (2010).

[188] Schalberger, P. *Komplementäre Niedertemperatur-Polysiliziumschaltungen für vollintegrierte Aktiv Matrix Anzeigen mit organischen Leuchtdioden*. PhD thesis.

[189] Schindler, A., Pross, A., Baur, H., and Fruehauf, N., 62.2: AMLCD with Carbon-Nanotube Pixel Electrodes, *SID Symposium Digest of Technical Papers* **39**, 947 (2008).

[190] Schalberger, P., Herrmann, M., Hoehla, S., and Fruehauf, N., A fully integrated 1-in. AMOLED display using current feedback based on a five-mask LTPS CMOS process, *Journal of the Society for Information Display* **19**, 496 (2011).

[191] Herrmann, M. Entwurf und Anwendung eines LTPS CMOS Operationsverstärkers. Master's thesis, University of Stuttgart, 2009.

[192] Baker, R.J., *Cmos: Circuit Design, Layout, And Simulation*, BWSTM.

[193] Lutz, G., Buttler, W., Bergmann, H., Holl, P., Hosticka, B., Manfredi, P., and Zimmer, G., Low noise monolithic CMOS front end electronics,

*Nuclear Instruments and Methods in Physics Research Section A: Accelerators, Spectrometers, Detectors and Associated Equipment* **263**, 163–173 (1988).

[194] An, M., Chen, C., Gao, C., Han, M., Ji, R., Li, X., Mei, Y., Sun, Q., Sun, X., Wang, K., Xiao, L., Yang, P., and Zhou, W., A low-noise CMOS pixel direct charge sensor, Topmetal-II-, *Nuclear Instruments and Methods in Physics Research Section A: Accelerators, Spectrometers, Detectors and Associated Equipment* **810**, 144–150 (2016).

[195] Saukoski, M., Aaltonen, L., Halonen, K., and Salo, T., Fully Integrated Charge Sensitive Amplifier for Readout of Micromechanical Capacitive Sensors.

[196] Enz, C. and Temes, G., Circuit techniques for reducing the effects of op-amp imperfections: autozeroing, correlated double sampling, and chopper stabilization, *Proceedings of the IEEE* **84**, 1584–1614 (1996).

[197] AN-617 Application Note: Wafer Level Chip Scale Package. techreport AN-617, Analog Devices, P.O. Box 9106, Norwood, MA 02062-9106, U.S.A., 2007.

# Publications and supervised theses

## Publications

- J. Schmidt and P. Schalberger and H. Baur and R. Löw and T. Pfau and H. Kübler and N. Fruehauf, A transimpedance amplifier based on an LTPS process operated in alkali vapor, *21$^{st}$ Int. Workshop Active-Matrix Flatpanel Displays and Devices, AM-FPD*, 2017

- J. Schmidt, P. Schalberger, H. Baur, R. Löw, T. Pfau, H. Kübler, and N. Fruehauf, A transimpedance amplifier based on an LTPS process operated in alkali vapor for the measurement of an ionization current, *SPIE, Proceeding Quantum Technologies*, 2018
  *Awarded for "Best student paper presentation" at the SPIE's Photonics Europe International Symposia held 22-26 April 2018 in Strasbourg, France*

- J. Schmidt, M. Fiedler, R. Albrecht, D. Djekic, P. Schalberger, H. Baur, R. Löw, N. Fruehauf, T. Pfau, J. Anders, E. R. Grant, and H. Kübler, Proof of concept for an optogalvanic gas sensor for NO based on Rydberg excitations, *Applied Physics Letters* **113**, 011113, 2018

- J. Schmidt, Y. Münzenmaier, P. Kaspar, P. Schalberger, H. Baur, R. Löw, N. Fruehauf, T. Pfau, and H. Kübler, An optogalvanic gas sensor based on Rydberg excitations, *In preparation*, 2018

## Bachelor theses

- Max Kühn: Thermische Rydbergatome im Hintergrundgas, 2016

- Rebecca Schmieg: Setup and Characterization of a Laser Amplifier for Rydberg Excitation in thermal Rb Atoms, 2016

- Kateryna Guguieva: Design of electrical transmission lines for the measurements in a rubidium vapor cell, 2016
- Fabian Munkes: Aufbau eines Frequenzmodulationssystems zur Spektroskopie in optisch dünnen Alkaligasen, 2016
- Yannick Münzenmaier: Optogalvanische Alkali-Spektroskopie in Hintergrundgasen, 2018


### Master theses


- Ralf Albrecht: Integrated and Time-Resolved Measurements of Collisional Energy Transfer in Rubidium P-States, 2017
- Markus Fiedler: Noise Characteristic of a Random Sampling LIA for Optogalvanic Spectroscopy in a Thermal Vapor Cell, 2018
- Fabian Munkes: In preparation, 2019


## Danksagung

Die vorliegende Arbeit war natürlich nur durch umfangreiche Unterstützung einer Vielzahl an Menschen möglich, denen ich nun leider nur in aller Kürze, die dem geleisteten Beitrag nicht gerecht wird, danken kann.
Zuerst danke ich Prof. Dr. Tilman Pfau für die Annahme zuerst als Master Student dann als Doktorand am 5. Physikalischen Institut. An die hier verbrachte Zeit werde ich mich sicherlich noch öfters zurückerinnern. Außerdem möchte ich Prof. Dr. Michler für den Mitbericht danken.
Nun ist es ja so, dass es ganz normal ist, dass ein Physikstudent an einem Physik Institut arbeitet. Wenn man nun aber einen Physiker an einem Elektrotechnikinstitut arbeiten lässt, noch dazu in einem solch hochklassigen Reinraum, wie der am Institut für Großflächige Mikroelektronik, dann zeugt das von einem sehr hohem Vertrauen, welches mir von Prof. Dr. Norbert Frühauf entgegengebracht wurde. Ich habe äußerst viel bei Ihnen lernen dürfen und denke, dass unsere Zusammenarbeit äußerst fruchtbar war. Es ist ganz eindeutig, dass die Idee der Anwendung der Rydberganregungen für die Gasdetektion nur durch unsere interdisziplinäre Zusammenarbeit überhaupt erst aufgekommen ist.

Ein weiteres Beispiel der sehr erfolgreichen interdisziplinären Zusammenarbeit, ist die Kooperation mit dem Institut für Intelligente Sensorik und Theoretische Elektrotechnik an der Universität Stuttgart. Durch die Vielfache Unterstützung durch Prof. Dr. Jens Anders aber auch durch Denis Djekic wurden die Messungen an Stickoxid in Vancouver in der vorliegenden Form ermöglicht.
Dass die Idee eines Gassensors basierend auf Rydberganregungen nicht bloß ein reines theoretisches Gedankenkonstrukt geblieben ist, sondern dass die Anwendbarkeit an einem relevanten Molekül demonstriert werden konnte, verdanke ich Prof. Dr. Ed Grant. Ich bin immer noch erstaunt und zugleich umso dankbarer, dass ich während meines Austauschs das gesamte Labor verwenden konnte und dabei völlig freie Hand bei der Umsetzung der Experimente erhalten habe.
Es gibt zwei Leute, die am allermeisten und am öftesten zu diesem Projekt beigetragen haben. Das sind Dr. Harald Kübler und Dr. Patrick Schalberger. Diese beiden sind die zwei, die dieses Projekt durch ihr unerschöpfliches Know-How und Wissen durchgetragen haben und ohne die ich schon lange an einem der vielen kleinen Herausforderungen hängen geblieben wäre. Darüber hinaus hatten wir auch auf persönlicher Ebene jede Menge Spaß und ich konnte mich auf euren Rückhalt immerzu verlassen. Dafür bin ich sehr dankbar.
Da ich nun an zwei Instituten angestellt war, möchte ich an dieser Stelle ganz allgemein dem Institut für Großflächige Mikroelektronik und dem 5. Physikalischen Institut danken. Insbesondere muss ich da an folgende Kollegen denken: Das sind Holger Baur und Elisabeth Schuler, Dr. Robert Löw und Patrick Kaspar, die mindestens genauso wie alle anderen zu diesem Projekt beigetragen haben.
Einen großen Anteil am Gelingen dieser Arbeit haben natürlich auch all die Studenten, deren Abschlussarbeiten ich mitbetreut habe, auch wenn die Thematik im Einzelnen nicht immer genau passend zu dem Gassensor Projekt war: Max Kühn, Rebecca Schmieg, Kateryna Guguieva, Fabian Munkes, Yannick Münzenmaier, Ralf Albrecht, Markus Fiedler. Vielen Dank für die sehr harmonische Zusammenarbeit, die eigentlich immer Hand in Hand ging. Genauso angenehm war auch die Zusammenarbeit mit Herrn Frank Schreiber. Vielen Dank für all die Unterstützung über die vier Jahre hinweg.
Bei all den beruflichen und fachlichen Errungenschaften geht mein größter Dank aber immer noch an meine Familie und meine Freunde. Auch in Zeiten in denen scheinbar niemand auf meiner Seite stand, konnte ich mich immer auf euren Rückhalt verlassen. Ihr ward immer meine Zuflucht und meine größte Unterstützung. Ich bin so froh, dass es euch gibt.

# Erklärung

Hiermit erkläre ich, dass ich diese Arbeit selbständig verfasst und keine anderen als die von mir angegebenen Quellen und Hilfsmittel verwendet habe.

Stuttgart, 11. Januar 2019

Johannes Schmidt